Optical Probing of Laser-Induced Expansion of Levitating Microspheres

Martin Speicher

München 2022

Optical Probing of Laser-Induced Expansion of Levitating Microspheres

Martin Speicher

Dissertation
der Fakultät für Physik
der Ludwig-Maximilians-Universität
München

vorgelegt von
Martin Speicher
aus Traunstein

München, den 17.05.2022

Erstgutachter: Prof. Dr. Jörg Schreiber

Zweitgutachter: PD Dr. Anna Tauschwitz

Tag der mündlichen Prüfung: 30.06.2022

Zusammenfassung

In der vorliegenden Arbeit wird die Expansionsdynamik von schwebenden Mikrokugeln nach der Interaktion mit einem fs-kurzen Laserimpuls im Intensitätsbereich von $10^{15} - 10^{16}\,W/cm^2$ mithilfe eines Pump-Probe-Experiments untersucht. Die Studie umfasst zwei Plasmadiagnostiken: ein intrinsisches Probing entlang der Laserachse durch den auf t = 0 ps fixierten Pump-Puls und ein zeitlich variables, laterales Probing durch einen separaten Probe-Puls. In beiden Fällen wird das transmittierte Licht über einen Streuschirm aufgezeichnet, der eine sehr simple Diagnostik darstellt, die in den meisten Hochleistungslaserexperimenten implementiert werden kann. Um eine Plasmadichteverteilung aus den aufgezeichneten Inline-Hologrammen zu extrahieren, wird das Experiment durch numerische Simulationen mit dem Python-Paket LightPipes reproduziert. Der Simulationsaufbau wird durch Vergleich mit experimentellen Größen wie Fokusgröße, Strahlprofilen und Hologrammen wohldefinierter Polystyrol-Kugeln kalibriert. Mehrere radialsymmetrische Modelle werden für die Modellierung der Dichteverteilung des Plasmas zu verschiedenen Zeitpunkten während seiner Entwicklung getestet, indem Simulationsergebnisse mit aufgezeichneten experimentellen Bildern verglichen werden. Die beste Übereinstimmung wird für eine Gauß-förmige Dichteverteilung mit einer zusätzlichen, dezentralen Gauß-Komponente erzielt. Die Validität dieses empirisch ermittelten Modells wird durch Simulationen mit dem Hydrodynamik-Code RALEF weiter untermauert, wofür experimentell ermittelte Werte für die räumliche und zeitliche Intensitätsverteilung als Input verwendet wurden. Der zeitliche Verlauf der expandierenden Dichteverteilung wird mit einem einfachen Modell unter Annahme hydrodynamischer Expansion des Plasmas verglichen. Die gute Übereinstimmung zwischen den experimentellen Daten und dem Modell ermöglicht es, physikalische Größen wie die Laserabsorption zu bestimmen und sie mit experimentellen Bedingungen des Plasmas in Beziehung zu setzen. Die Ergebnisse dieser Arbeit sind ein erster Schritt zur Untersuchung der Expansion von mikrometergroßen, kugelförmigen Targets bei Intensitäten weit oberhalb der Plasmabildungsschwelle und sind besonders relevant für zukünftige Experimente, die die Wechselwirkung von relativistisch intensiven Laserimpulsen mit dichteangepassten, subfokusgroßen Mikroplasmen untersuchen, z. B. auf dem Gebiet der Laser-Ionen-Beschleunigung.

Abstract

In the present work, the expansion dynamics of levitating microspheres following the interaction with a fs-short laser pulse in the intensity regime of $10^{15} - 10^{16}\,W/cm^2$ is investigated in a pump-probe experiment. The study comprises two plasma diagnostics: an intrinsic probing along the laser axis via the pump pulse, fixed at t = 0 ps, and a time-variable lateral probing on a separate probe pulse. In both cases, the transmitted light is recorded via a scatter screen, providing a very simple diagnostic tool that can be implemented in most high-power laser experiments. In order to extract a plasma density distribution from the recorded inline holograms, the experiment is reproduced via numerical simulations using the Python package LightPipes. The simulation setup is calibrated by comparison to experimental conditions such as focus size, beam profiles and holograms of defined polystyrene spheres. Several radial symmetric models are investigated for modeling the density distribution of the plasma at different times during its evolution by comparing simulation results against recorded experimental images. The best agreement is found for a Gaussian density distribution with an additional, decentralized Gaussian component. The validity of this empirically determined model is further strengthened by simulations using the hydrodynamic code RALEF, where experimentally obtained values for the spatial and temporal intensity distribution are used as input. The temporal course of the expanding density distribution is compared to a simple model assuming hydrodynamic expansion of the plasma. The good agreement between experimental data and the model allows determining physical quantities such as laser absorption and relate them to experimental conditions of the plasma. The findings of this work are a first step towards studying the expansion of micrometer spherical targets at intensities well above the plasma generation threshold and are particularly relevant for future experiments investigating the interaction of relativistically intense laser pulses with density-tailored, sub-focus sized microplasmas, e.g. in the field of laser-ion acceleration.

Contents

Zusammenfassung iii

Abstract v

Contents vii

List of Figures xi

List of Tables xv

1 Motivation and Context 1

1.1 Particle Accelerators 1

1.2 Plasma Diagnostics 3

1.3 Aim of this Work 5

1.4 Thesis Structure 6

2 Theory 9

2.1 Electromagnetic Waves 9

2.2 Free Electron in a Plane Wave 12

2.3 Ionization Processes 15

2.4 Plasma 18

2.5 Laser Absorption 20

2.6 Plasma Expansion 24

2.7 Scalar Diffraction Theory 28

3 Experimental Setup 35

3.1 High-Power Laser Systems (ZEUS) 35

3.2 Pump-Probe Setup of Levitating Spheres 41

3.3 Diagnostics 43

3.3.1 Pump 44
3.3.2 Probe 45
3.3.3 Laser Characterization 51

4 Simulations 55
4.1 Simulation Setup 56
4.1.1 Setup of Pump Simulation 57
4.1.2 Setup of Probe Simulation 61
4.1.3 Implementation of Density Distribution 64
4.2 Density Models 69
4.2.1 Initial Sphere and Particle Number 70
4.2.2 Exponential Distribution 71
4.2.3 Single Gaussian Distribution 75
4.2.4 Dual Gaussian Distribution 79
4.3 RALEF Simulations 86
4.4 Methodology 90

5 Analysis and Evaluation 99
5.1 Selection of Evaluable Data 99
5.2 Pump 102
5.2.1 Position in Focal Plane 103
5.2.2 Density Distribution 104
5.3 Probe 107
5.3.1 Negative Delay ($t < 0$ ps) 107
5.3.2 Zero Delay ($t = 0$ ps) 109
5.3.3 Positive Delay ($t > 0$ ps) 110
5.4 Discussion 112

6 Summary and Outlook 129
6.1 Summary 129
6.2 Outlook 130

List of Abbreviations 133

Publications and Conference Contributions 135

Bibliography 139

Acknowledgements **151**

List of Figures

2.1 Optical ionization 17

3.1 Basic laser setup 36
3.2 Chirped Pulse Amplification 37
3.3 Regenerative/Multipass amplifier 38
3.4 Layout ZEUS laser system 39
3.5 Experimental setup at ZEUS 42
3.6 Pump/Probe diagnostics 43
3.7 Pump transmission images 45
3.8 Overview of probing scenarios 46
3.9 Probe transmission images 47
3.10 Oversaturated probe image and setup of probe diagnostic 49
3.11 Unfiltered diffration image 50
3.12 Filtered diffraction image 50
3.13 Spatial intensity distribution (pump) 53
3.14 Autocorrelation trace (pump) 54

4.1 Setup pump simulation 58
4.2 Calibration pump simulation: focus 59
4.3 Calibration pump simulation: beam profile 60
4.4 Setup probe simulation 62
4.5 Calibration probe simulation: empty shot 63
4.6 Calibration probe simulation: initial sphere 64
4.7 Implementation of density distribution 65
4.8 Discretization of refractive index values 67
4.9 Test case for imaginary index 68
4.10 Density distribution: exponential 71
4.11 Comparison exp./sim. for exponential distribution (pump) 73

4.12 Comparison exp./sim. for exponential distribution (pump, profile) . . . 74
4.13 Comparison exp./sim. for exponential distribution (probe) 74
4.14 Comparison exp./sim. for exponential distribution (probe, profile) . . . 75
4.15 Density distribution: single Gaussian 76
4.16 Comparison exp./sim. for single Gauss. distribution (pump) 77
4.17 Comparison exp./sim. for single Gauss. distribution (pump, profile) . . 78
4.18 Comparison exp./sim. for single Gauss. distribution (probe) 78
4.19 Comparison exp./sim. for single Gauss. distribution (probe, profile) . . 79
4.20 Density distribution: dual Gaussian (centered) 81
4.21 Density distribution: dual Gaussian (moving) 82
4.22 Comparison exp./sim. for dual Gauss. distribution (pump) 83
4.23 Comparison exp./sim. for dual Gauss. distribution (pump, profiles) . . 83
4.24 Comparison exp./sim. for dual Gauss. distribution (probe) 84
4.25 Comparison exp./sim. for dual Gauss. distribution (probe, profiles) . . 84
4.26 Comparison of density models 85
4.27 RALEF simulation results 89
4.28 Methodology pump 91
4.29 Methodology probe 95
4.30 Best fit/error margins probe 97

5.1 Differentiation of initial particle size 100
5.2 Cutout of scaled temporal intensity distribution 103
5.3 Sphere position in laser focus/transmission vs. offset 103
5.4 Parameters of density distribution (pump) 105
5.5 Reconstructed density distributions (pump) 106
5.6 Critical density and limiting radius (pump) 107
5.7 Profile diffraction image (negative delay) 108
5.8 Profile diffraction image (zero delay) 110
5.9 Illustration expansion model 115
5.10 Experimental data in expansion model (small offset) 117
5.11 Experimental data in expansion model (medium offset) 118
5.12 Experimental data (t = 0 ps) in expansion model (small & medium offset) 119
5.13 Experimental data in expansion model (large offset) 120
5.14 Model for energy within area of critical density 122
5.15 Fractional absorption versus peak intensity 124
5.16 Approximation of scale length 125

5.17 Comparison of exp./theor. absorption and scale length 126

List of Tables

5.1 List of all evaluated shots (pump) 101
5.2 List of all evaluated shots (probe) 111
5.3 Probe data grouped by offset with corresponding plasma front radius . 116
5.4 List of initial plasma energies 121
5.5 Energy within growing area of critical density 123

Chapter 1

Motivation and Context

Contents

1.1 **Particle Accelerators** 1

1.2 **Plasma Diagnostics** 3

1.3 **Aim of this Work** 5

1.4 **Thesis Structure** 6

This chapter serves as an introduction to the field of laser-plasma acceleration and highlights some efforts that have been made in the last decades to study the interaction of high-intensity laser pulses with plasmas.

1.1 Particle Accelerators

"It would be of great scientific interest if it were possible in laboratory experiments to have a supply of electrons and atoms of matter in general, of which the individual energy of motion is greater even than that of the α-particle. This would open up an extraordinarily interesting field of investigation which could not fail to give us information of great value, not only on the constitution and stability of atomic nuclei but in many other directions."

With these words, addressed to the Royal Society in 1927 [1], Ernest Rutherford expressed his wish for a MeV-class particle accelerator. Today, such machines are no longer wishful thinking and, as Rutherford predicted, have made groundbreaking contributions to our understanding of physics. Here, the discovery of the Higgs boson [2, 3] is the most recent in a long line of Nobel Prize rewarded discoveries that would not have been possible without particle accelerators. Major facilities such as the Large Hadron Collider are capable of accelerating particles to energies of several TeV. However, accelerators have become indispensable not only in the field of fundamental research but also in many practical applications such as medical imaging [4, 5], radiation therapy [6, 7] or industrial processes [8].

In most cases, the particles are accelerated by electrostatic or radio frequency fields. Due to material breakdown, these have an upper limit with regard to the available electric fields of around 100 MV/m [9, 10, 11]. This also results in a lower limit for the compactness of such accelerators. Therefore, high-energy accelerators are often built in a ring shape, where the acceleration cavities can be used repeatedly until the target energy is reached. But even such configurations cannot reach arbitrarily high energies, since they are limited by losses due to synchrotron radiation and the increasingly difficult steering of the particles.

Plasma-based Accelerators

A concept capable of circumventing such limitations was introduced by Veksler [12] in 1957, proposing a plasma as the accelerating medium, where electric breakdown is no longer a limitation as the plasma already consists of ionized matter. In contrast to the conventional acceleration of individual particles by an external electric field, here a collective acceleration of ions can be achieved by a plasma wave, exited by an injected high-energetic electron beam. Early experiments, trying to demonstrate this concept, could not achieve the projected high energy gain due to instabilities of the plasma wave [13]. By adopting the scheme to the acceleration of electrons and changing the driver of the plasma wave to a laser, which was invented by Maiman in 1960 [14] Tajima and Dawson proposed a new concept called Laser Wakefield Acceleration (LWFA) [15]. Here an ultra-short, intense laser pulse drives a plasma wave moving with a relativistic phase velocity which results in a much more stable acceleration structure. At that time lasers were not able to deliver the required pulse length or intensity although they became shorter and more intense through techniques such as Q-switching [16]. With the invention of Chirped Pulse Amplification (CPA) [17] in 1985 the achievable laser parameters experienced an enormous boost and were able to unleash the full potential of the LWFA concept [18]. Achievable electric fields can exceed those of conventional accelerators by several orders of magnitude and by that allow to compactify the accelerator design. In 2019, electrons with an energy of about 8 GeV could be accelerated over a distance of only 20 cm [19], where conventional accelerators would need on the order of 100 m to reach the same energy.

The laser-driven acceleration of ions has not yet reached the scale desired by Veksler because the necessary experimental conditions have not yet been met. Nevertheless, this field is being developed with great effort, especially since experiments in 2000 showed the generation of multi-MeV ions from the interaction of high-intensity lasers with solid-state density targets [20, 21, 22]. The acceleration of these ions is achieved indirectly by charge separation fields that can reach strengths on the order of the electric field of the laser (MV/μm). These are created, for example, when the laser energizes electrons on the irradiated side of the target. The electrons pass through the target and escape into the vacuum on the non-radiated side, where they induce strong fields that accelerate target ions. This mechanism is called Target Normal Sheath Acceleration (TNSA) [23] and generates ions of a broad energy distribution with an exponentially decaying particle number up to a typically well-defined cutoff energy. The maximum of these cutoff energies has meanwhile been pushed towards the 100 MeV mark [24, 25, 26]. In addition, laser-accelerated ions exhibit a number of specific properties (small source size (μm), short emission time (fs - ps) and co-emission of different particle species and radiation types [27, 28, 29]) that make them interesting for applications. Nevertheless it is often the broad energy spectrum that restricts applicability. Therefore several approaches where made to narrow the spectrum towards a quasi-monoenergetic distribution. Prime examples utilized the manipulation of the target and/or the laser parameters in foil-based experiments (e.g. [30, 31, 32, 33]), near-critical densities (e.g. [34, 35]), mass-limited targets (e.g. [36, 37, 38]) or a combination of the latter two [39].

1.2 Plasma Diagnostics

In all the experiments and mechanisms described above, the plasma is of essential importance as the accelerating medium. It is therefore not surprising that one of the main tasks in experiments is to study and understand it in detail. From such data, model predictions can be tested, new models developed, experimental conditions verified and experimental results explained. Laser-driven plasmas change at relativistic velocities and are often only micrometers in size, making detailed measurements very challenging. Since such structures are unique to laser plasma acceleration, a variety of diagnostics have been and are being developed to study the plasma itself or its properties, ideally with spatial and temporal resolution.

Spectroscopic analysis of electromagnetic radiation, emitted by the plasma, offers a wide range of diagnostic possibilities. This includes higher harmonics of the frequency of the driving laser [40], a broad spectrum of X-rays [41, 42] as well as radiation in the far-infrared range [43]. The study of the latter, for example, allowed the first direct observation of laser-induced wake fields [43].

Many plasma diagnostics use external electromagnetic pulses (often called probe in this context) to examine the plasma. Among the most established techniques are shadowgraphy and schlieren imaging. In shadowgraphy, the plasma is typically trans-illuminated with a laser pulse whose intensity distribution is then recorded on a detector, either directly or via an imaging system. Information about the plasma is obtained from the density dependence of the refractive index in the plasma. This causes the examining laser pulse to be diffracted or even blocked according to the spatial density distribution of the plasma. Shadowgraphy is particularly well suited to observe ultrafast changes in the density distribution. For example, the evolution of a plasma wave in a laser wakefield accelerator [44] or the dynamics of the laser-plasma interaction in foil experiments [45] for laser-ion acceleration could be studied with femtosecond time resolution. Schlieren imaging is closely related to the technique of shadowgraphy. The setup is very similar, but in schlieren imaging an aperture (often at the focus of the imaging lens) is used to block light unaffected by plasma. This method directly measures the angle of deflection (first derivative of refractive index) while shadowgraphy measures the displacement of the examining light due to the deflection (second derivative of refractive index). In general, the schlieren technique is therefore more sensitive and suitable for measuring smaller density fluctuations.

However, both techniques usually provide only qualitative measurements of density variations and are thus often used to monitor dynamics. For quantitative statements, interferometric diagnostics can be employed for measuring miniscule refractive index changes. For this purpose, a laser pulse is typically split and one beam is used as a reference while the second beam is sent through the plasma. The changes in the refractive index caused by the plasma change the phase or optical path, which is reflected in fringe shifts in the interferogram of the two beams. Interference-based methods have been used extensively to characterize laser-driven wakefields [46] or to measure the expansion of dense plasmas after the interaction of solid-state density targets with high-intensity lasers [47]. If not only relative phase-differences need to be measured, holography, invented by Gabor in 1948 [48], can be used. Here, a interference pattern between an undisturbed reference beam and a beam diffracted by the object to be investigated is recorded. Within this interference the phase structure of the object is encoded and allows to subsequently reconstruct the object. Such diagnostics allow to quantify the electron density distribution in a plasma with great spatial resolution [49]. By adapting the holographic principle towards the frequency domain [50], plasma structures, moving with relativistic velocities, can be recorded within a single measurement [51].

The dominant limitation for probe pulses is set by the critical density. This defines a limit above which the plasma is no longer transparent but opaque. Thus, access to the density distribution in high density regions (for optical radiation at electron densities of the order of and beyond $n_e \sim 10^{21}/cm^3$) remains out of reach. Consequently, efforts for providing probes with shorter wavelength approach now the X-ray regime, since the critical density is indirectly proportional to the square of the wavelength of the probe. With picosecond-long X-ray pulses, these regions could be studied in detail for the first time (e.g. [52, 53]). With the development of free electron lasers, which are able to deliver femtosecond-short X-ray pulses, the temporal resolution can be drastically improved and allows the investigation of the solid-density dynamics in great spatial and temporal resolution (e.g. [54]).

1.3 Aim of this Work

This work focuses on the laser-induced expansion of micron-sized, mass-limited spherical targets. It is motivated by the work of Hilz et. al. [39], who demonstrated a directional acceleration of ions with a narrow energy spread by experiments with such targets at the petawatt-class laser PHELIX at the GSI Darmstadt. The decisive factor and novelty in these experiments was that the high-intensity laser pulse did not interact with a solid-state density target but with a micrometer-small near-critical-density plasma. The necessary pre-expansion occurred naturally (and thus uncontrolled) over 100 ps in the rising edge of the intensity of the 500 fs long laser pulse. For experiments using shorter-pulse lasers, which are designed to prevent such pre-mature expansion, and to gain control over the pre-expansion, the use of adjustable pre-pulses is considered to optimize the plasma conditions for the interaction with the main laser pulse.

This work serves as a preliminary study for further experiments on high-power laser systems in which two aspects in particular are to be investigated. On the one hand, plasma diagnostics should be developed that are as simple as possible and allow the precise investigation of the plasma state. The concept of inline holography, which allows to reconstruct the density distribution in three dimensions, is used. This will also be implemented in future high-power experiments to allow the verification of the plasma conditions. On the other hand, a simple, analytical model for the time course of the plasma expansion is to be determined with which predictions can be made about the expansion behavior. This model can then serve as a guideline to determine the appropriate experimental parameter range for the short pre-pulse. For the study, a pump-probe experiment in combination with a Paul trap target system [55] is realized using the dual-beam ZEUS laser system at the Centre for Advanced Laser Applications (CALA) in Garching, where the main beam simulates the short pre-pulse of a high-power experiment, interacting with micrometer-sized plastic spheres, while the time course of the subsequent expansion is investigated with a second beam. Even though the involved (optical) laser pulses cannot access the high-density region of the micro-plasma, their very nature enables determining most relevant plasma parameters via detailed numerical modeling of the probing process with simplified, empirical plasma-density distributions.

1.4 Thesis Structure

Chapter 2 provides the theoretical basis of physical aspects relevant to this thesis. It illuminates laser-plasma interaction, introduces different expansion models of plasmas and describes the basic theoretical concepts of the simulations used for interpreting the experimental results.

Chapter 3 presents the experimental setup for studying the temporal behavior of laser-generated micro-plasmas and introduces the diagnostics developed for this purpose.

Chapter 4 introduces the numerical simulations that were used to reconstruct the key plasma parameters from the experimental data with the help of empirical, analytical 3D models.

Chapter 5 presents the plasma parameters obtained from the combination of experiment and simulation. In comparison with previous expansion models, the temporal dynamics and the influence of the laser parameters, in particular the intensity, becomes accessible.

Chapter 6 summarizes the findings obtained in this thesis and provides recommendations for exploitation in future experiments.

Chapter 2

Theory

Contents

2.1 Electromagnetic Waves 9

2.2 Free Electron in a Plane Wave 12

2.3 Ionization Processes 15

2.4 Plasma 18

2.5 Laser Absorption 20

2.6 Plasma Expansion 24

2.7 Scalar Diffraction Theory 28

This chapter provides the theoretical background of the physics relevant to this thesis. These include the description of light and plasma, as well as their interaction and important mechanisms concerning ionization, absorption and expansion. Finally, the main formalisms of scalar diffraction theory that provide the basis for the numerical simulations are introduced.

2.1 Electromagnetic Waves

[1]The consideration of light as an electromagnetic wave follows from Maxwell's equations, with the help of which electromagnetic fields can be completely described [57]:

---

[1] This section follows [56, 57]

$$\begin{aligned}
(I) &\quad \vec{\nabla}\vec{E} = \frac{\rho}{\epsilon}, \\
(II) &\quad \vec{\nabla}\vec{B} = 0, \\
(III) &\quad \vec{\nabla} \times \vec{E} = -\frac{\partial \vec{B}}{\partial t}, \\
(IV) &\quad \vec{\nabla} \times \vec{B} = \mu\vec{j} + \mu\epsilon\frac{\partial \vec{E}}{\partial t},
\end{aligned} \tag{2.1}$$

where $\vec{E}$ and $\vec{B}$ are the vectorial electric and magnetic field, ρ is the charge density, $\vec{j}$ is the current density and ϵ and μ are the medium-specific dielectric permittivity and magnetic permeability, respectively. In the absence of charges and currents ($\rho = 0$, $\vec{j} = 0$) and using $\vec{\nabla} \times (III)$ and $\vec{\nabla} \times (IV)$, one obtains the harmonic wave equations

$$\begin{aligned}
\vec{\nabla}^2\vec{E} - \frac{1}{v^2}\frac{\partial^2 \vec{E}}{\partial t^2} = 0, \\
\vec{\nabla}^2\vec{B} - \frac{1}{v^2}\frac{\partial^2 \vec{B}}{\partial t^2} = 0,
\end{aligned} \tag{2.2}$$

which describe the propagation of an electromagnetic wave with a velocity of $v = 1/\sqrt{\mu\epsilon}$. Using the medium refractive index $\eta = \sqrt{\frac{\mu\epsilon}{\mu_0\epsilon_0}}$ and the speed of light $c = 1/\sqrt{\mu_0\epsilon_0}$, one finds that $v = c/\eta$. In a vacuum with $\eta = 1$, the velocity thus becomes c.

Monochromatic, plane waves

A possible solution that satisfies equation 2.2, are monochromatic, plane waves that travel in one direction $\vec{k}$. Consequently the fields can be assumed to have the form

$$\begin{aligned}
\vec{E}\left(\vec{r}, t\right) = \vec{e}_1 \cdot E_0 \cdot cos\left(\vec{k}\vec{r} - \omega t + \phi_0\right), \\
\vec{B}\left(\vec{r}, t\right) = \vec{e}_2 \cdot B_0 \cdot cos\left(\vec{k}\vec{r} - \omega t + \phi_0\right),
\end{aligned} \tag{2.3}$$

with E_0 and B_0 being constant amplitudes, ϕ_0 being a constant phase term and the dispersion relation $\omega = \left|\vec{k}\right| \cdot v$. $\vec{e}_1$ and $\vec{e}_2$ denote constant unit vectors. From $\vec{\nabla}\vec{E} = 0$ and $\vec{\nabla}\vec{B} = 0$ follows that $\vec{e}_1 \cdot \vec{k} = 0$ as well as $\vec{e}_2 \cdot \vec{k} = 0$, meaning that both fields are perpendicular to the propagation direction or in other words, that the wave is transverse. Moreover, it can be shown that $\vec{k} \perp \vec{e}_1 \perp \vec{e}_2$ and that the relation between the field amplitudes is given by $E_0 = v \cdot B_0$.

It is often convenient to use a complex notation for electromagentic waves. The sinusodal solution for the electric field found above can also be written in the form of

$$\vec{E}\left(\vec{r},t\right) = Re\left[\vec{e}_1 \cdot E_0 \cdot e^{i\phi_0} \cdot e^{i\left(\vec{k}\vec{r} - \omega t\right)}\right]. \tag{2.4}$$

Introducing a complex amplitude $E_0' = E_0 \cdot e^{i\phi_0}$, equations 2.3 can be expressed as

$$\begin{aligned} \vec{E}'\left(\vec{r},t\right) &= \vec{e}_1 \cdot E_0' \cdot e^{i\left(\vec{k}\vec{r} - \omega t\right)}, \\ \vec{B}'\left(\vec{r},t\right) &= \vec{e}_2 \cdot B_0' \cdot e^{i\left(\vec{k}\vec{r} - \omega t\right)}. \end{aligned} \tag{2.5}$$

It should be noted that the electric field of 2.3 (and consequently 2.5) always points in the direction of $\vec{e}_1$, the wave thus is linearly polarized along that direction. For a more general consideration, the electric field for example would be a superposition of the form $\vec{E}'\left(\vec{r},t\right) = \left(\vec{e}_1 \cdot E_1' + \vec{e}_2 \cdot E_2'\right) \cdot e^{i\left(\vec{k}\vec{r} - \omega t\right)}$ [56] which also allows to find solutions for the cases of circular or elliptical polarization. For simplicity and as only linear polarized light was used in the experiments, these cases are not considered further.

While traveling, the wave carries energy. The energy flux is described by the Poynting vector

$$\vec{S} = \frac{1}{\mu}\left(\vec{E} \times \vec{B}\right). \tag{2.6}$$

Inserting 2.3 gives $\vec{S} = v \cdot \epsilon \cdot E_0^2 \cdot cos^2\left(\vec{k}\vec{r} - \omega t + \phi_0\right)\vec{e}_3$, pointing in propagation direction. The intensity (or average power per unit area) of the electromagnetic wave is defined as the cycle-averaged magnitude of the Poynting vector:

$$I = \langle S \rangle = \frac{1}{2} \cdot v \cdot \epsilon \cdot E_0^2, \tag{2.7}$$

where $\langle cos^2 \rangle = 1/2$ was used.

Intensity of a laser pulse in the focal plane

In the context of laser-plasma experiments, where a short laser-pulse is focused to a small spot, the intensity in the focal plane is a key parameter. When using real pulses, the electric field amplitude (and thus the intensity) is no longer independent of space and time. Assuming simple Gaussian envelopes for both, the intensity for a pulse propagating in z-direction then reads:

$$I\left(x,y,t\right) = I_0 \cdot e^{\left(-\frac{2\cdot x^2}{\sigma_x^2}\right)} \cdot e^{\left(-\frac{2\cdot y^2}{\sigma_y^2}\right)} \cdot e^{\left(-\frac{2\cdot t^2}{\sigma_t^2}\right)}. \tag{2.8}$$

It is not possible to measure the intensity directly, but it must be determined from accessible parameters. Such measurements provide the energy in a pulse W, the full width at half maximum (FWHM) duration of the temporal intensity distribution t_{FWHM} and the FWHM diameter of the spatial intensity distribution d_{FWHM}. The FWHMs and the standard deviations are related via $t_{FWHM} = \sqrt{2ln2} \cdot \sigma_t$ and $d_{FWHM} = \sqrt{2ln2} \cdot \sigma_x = \sqrt{2ln2} \cdot \sigma_y$. Integrating the intensity $I\left(x,y,t\right)$ over space and time results in the pulse energy:

$$\begin{aligned} W &= \int_{-\infty}^{+\infty}\int_{-\infty}^{+\infty}\int_{-\infty}^{+\infty} I\left(x,y,t\right)\, dx\, dy\, dt \\ &= I_0 \cdot \sigma_t \cdot \sigma_x \cdot \sigma_y \cdot \left(\frac{\pi}{2}\right)^{\frac{3}{2}} \\ &= I_0 \cdot t_{FWHM} \cdot d_{FWHM}^2 \cdot \left(\frac{\pi}{4ln2}\right)^{\frac{3}{2}}. \end{aligned} \tag{2.9}$$

Finally, this yields the peak intensity I_0 in the focal plane:

$$I_0 = \frac{0.83 \cdot W}{t_{FWHM} \cdot d_{FWHM}^2}. \tag{2.10}$$

2.2 Free Electron in a Plane Wave

[2]Before describing effects of laser-matter interaction, it is first worth considering a single free electron with a plane electromagnetic wave in vacuum and neglecting radiation due to the acceleration of the electron. Starting with a wave propagating in direction $\vec{e}_3 = \vec{z}$ and the electric field being linearly polarized along $\vec{e}_1 = \vec{x}$, the electron equation of motion is

$$\frac{d\vec{p}}{dt} = \frac{d\left(\gamma \cdot m_e \cdot \vec{v}_e\right)}{dt} = -e\left(\vec{E}\left(\vec{r},t\right) + \vec{v}_e \times \vec{B}\left(\vec{r},t\right)\right), \tag{2.11}$$

where e and m_e are the electron charge and rest mass, v_e is the velocity of the electron and $\gamma = 1/\sqrt{1 - v_e^2/c^2}$ the Lorentz factor. Due to the electric field, the electron

---

[2] This section follows [58, 59]

starts oscillating along $\vec{x}$ with a maximum velocity $v_{e,max}$ that can be approximated in the non-relativistic regime ($v_e << c$) as $v_{e,max} = \frac{eE_0}{m_e\omega}$. The second term results in a force acting on the electron along the wave propagation direction $\vec{z}$. Following from $E_0 = c \cdot B_0$, this term becomes dominant when v_e approaches c. The dimensionless parameter a_0 marks the point where the longitudinal force exceeds the tranverse force and is defined as

$$a_0 = \frac{v_{e,max}}{c} = \frac{e \cdot E_0}{c \cdot m_e \cdot \omega}. \tag{2.12}$$

For $a_0 << 1$, the non-relativistic approximation is valid, while for $a_0 >> 1$ the longitudinal force will dominate. In terms of field amplitudes and intensity, this relativistic threshold ($a_0 = 1$) can be expressed as [60]

$$\begin{aligned} E_0 &= \frac{a_0 \cdot c \cdot m_e \cdot \omega}{e} = \frac{a_0}{\lambda\,[\mu m]} \cdot 3.21 \cdot 10^{12}\, \frac{V}{m}, \\ B_0 &= \frac{E_0}{c} = \frac{a_0}{\lambda\,[\mu m]} \cdot 1.07 \cdot 10^{4}\, \frac{T}{m}, \\ I &= \frac{1}{2} \cdot c \cdot \epsilon_0 \cdot E_0^2 = \frac{a_0^2}{\lambda^2\,[\mu m^2]} \cdot 1.37 \cdot 10^{18}\, \frac{W}{cm^2}, \end{aligned} \tag{2.13}$$

where $\lambda = 2\pi c/\omega$. In order to obtain the motion of the electron, it is useful to express the plane wave in terms of a vector potential $\vec{A}\,(\vec{r}, t)$ defined as

$$\begin{aligned} \vec{E}\,(\vec{r}, t) &= -\frac{\partial \vec{A}\,(\vec{r}, t)}{\partial t}, \\ \vec{B}\,(\vec{r}, t) &= \vec{\nabla} \times \vec{A}\,(\vec{r}, t)\,, \end{aligned} \tag{2.14}$$

and expanding 2.11 by $\vec{p}$, which gives the electron energy equation $\frac{d\left(\gamma \cdot m_e \cdot c^2\right)}{dt} = -e \cdot \vec{v}_e \cdot \vec{E}\,(\vec{r}, t)$. Following the calculations of [58, 60], the momentum components for an electron initially at rest yield

$$\begin{aligned} p_x &= e \cdot A, \\ p_z &= \frac{1}{2} \cdot \frac{p_x^2}{m_e \cdot c} = \frac{e^2 \cdot A^2}{2 \cdot m_e \cdot c}, \end{aligned} \tag{2.15}$$

where $A = A_0 \cdot sin\left(\phi\right)$ with $\phi = \vec{k}\vec{r} - \omega t + \phi_0$. Using $\vec{p} = \gamma m_e \frac{d\vec{r}}{dt} = \gamma m_e \frac{d\phi}{dt}\frac{d\vec{r}}{d\phi} = \gamma m_e \left(-\frac{\omega}{\gamma}\right)\frac{d\vec{r}}{d\phi}$, the trajectories can be derived from integrating 2.15:

$$\begin{aligned} x\left(\phi\right) &= \frac{e \cdot A_0}{m_e \cdot \omega} cos\left(\phi\right) = \frac{c \cdot a_0}{\omega} cos\left(\phi\right), \\ z\left(\phi\right) &= -\frac{e^2 \cdot A_0^2}{4 \cdot m_e^2 \cdot c \cdot \omega}\left(\phi - \frac{1}{2} sin\left(2\phi\right)\right) = -\frac{c \cdot a_0^2}{4 \cdot \omega}\left(\phi - \frac{1}{2} sin\left(2\phi\right)\right), \end{aligned} \tag{2.16}$$

with $a_0 = \frac{eA_0}{mc}$. The motion along the direction of the electric field is an oscillation with ϕ, while the motion along the wave propagation direction combines an oscillatory motion with 2ϕ and a linear drift in z-direction. The cycle-averaged drift velocity is given by

$$v_{drift} = \langle \frac{z}{t} \rangle = c \cdot \frac{a_0^2}{a_0^2 + 4}. \tag{2.17}$$

Considering a more realistic case of finite pulse length, where for example the field component is scaled by a temporal Gaussian envelope function as shown for the intensity calculations above, the electron will be at rest after the pulse has passed, albeit at another position along the propagation axis. Therefore the electron has no net energy gain after the interaction, which is in agreement with the Lawson-Woodward theorem [61, 62]. In the focus of a laser pulse, however, the transverse interaction region is not infinitely large (see Gaussian envelope assumption for intensity calculation). Thus, an electron sitting on the z-axis is pushed outwards during one half-cycle of the electric field and with the field changing sign, the restoring force becomes smaller due to the weaker electric field outside. As it does not return to its initial position, the electron will move further and further away from the propagation axis in each cycle and can gain a finite velocity after the pulse has passed. By accounting for the spatial dependency of the electric field one can introduce the (non-relativistic) ponderomotive force

$$\vec{F}_{pond} = -\frac{e^2}{4 \cdot m_e \cdot \omega^2}\vec{\nabla}\left(\vec{E}^2_{spatial}\right), \tag{2.18}$$

where $\vec{E}_{spatial}$ comprises the spatial dependence of the electric field $\vec{E}\left(\vec{r}, t\right) = \vec{E}_{spatial} \cdot cos\left(\omega t\right)$. The electron gets pushed along the direction of the gradient away from high-intensity regions ($I \propto E^2$). For relativistic treatment, an additional scaling by $1/\langle\gamma\rangle$ is required [58], where $\langle\gamma\rangle = \sqrt{1 + a_0^2/2}$ is the cycle-averaged Lorentz factor of the electron.

2.3 Ionization Processes

In the context of laser-plasma experiments, the first step is to consider the transformation from matter into the plasma state, i.e. the ionization of matter via interaction with the laser pulse. In the case of a single photon interacting with an atom, the photon energy $E_{ph} = \frac{h \cdot c}{\lambda}$, where h is Planck's constant and λ the photon wavelength, must be higher than the ionization energy E_{ion} of the target material to free an electron. Considering a Titanium:Sapphire laser with a central wavelength of 800 nm, as used in this experiment, a single photon ($E_{ph} = 1.55\,eV$) is not able to ionize most materials (typically 5 - 15 eV required). In the focus of a high-power laser pulse, there are however certain effects that can cause ionization.

Multiphoton Ionization

In the focus of a laser pulse, extremely high intensities can be achieved. This corresponds to a high flux of photons and a non-zero probablity of multiple photons interacting with a single atom. Thus, ionization can be achieved if $n_{min} \cdot E_{ph} = E_{ion} + E_{kin} > E_{ion}$ where n_{min} is the minimum number of absorbed photons requiered to exceed the ionization energy. The energy difference yields the kinetic energy of the now free electron. This process is called **Multiphoton Ionization (MPI)** (e.g. [63, 64]), with an ionization rate given by [63]

$$w_n = \sigma_n \cdot I^n, \tag{2.19}$$

where σ_n is the n-photon cross section and I the laser intensity. If more photons than n_{min} are absorbed (a process called **Above Threshold Ionization (ATI)** (e.g. [65, 64])), the electron inherits the excess energy as additional kinetic energy. As the photons provide quantized amouts of energy, the energy spectrum of these electrons shows distinct peaks, seperated by E_{ph} [66]. It should be noted that for above mechanisms the intensity is assumed to be small, hence the Coulomb potential of the atom is not disturbed.

Field Ionization

With increasing intensity, the laser electric field is capabale of distorting the binding potential of the atom. In the simplest picture, the disturbed potential is obtained by a superposition of the atomic potential ϕ_{atom} and an (at that moment) linear potential of the laser ϕ_L:

$$\phi = \phi_{atom} + \phi_L = -\frac{Z \cdot e}{4 \cdot \pi \cdot \epsilon_0 \cdot x} - E_0 \cdot x. \tag{2.20}$$

An electron can tunnel through this lowered potential barrier, a process known as **Tunnel Ionization (TI)** (e.g. [67]). The ionization rates can be calculated using different approaches, e.g. Keldysh [68] or the more advanced model by Ammosov, Delone and Krainov [69] which is able to account for complex many-electron atoms.

If the laser is able to suppress the potential barrier far enough such that the local maximum of the modified Coulomb potential is below the ionization potential of the atom, the electron becomes quasi-free. The position of the local maximum yields

$$x_{max} = \sqrt{\frac{Z \cdot e}{4\pi \cdot \epsilon_0 \cdot E_0}}. \tag{2.21}$$

Inserting this into 2.20 and by setting $-E_{ion} = e \cdot \phi\left(x_{max}\right)$ one obtains the necessary laser electric field for **Barrier Suppression Ionization (BSI)** (e.g. [70]) to occur:

$$E_0 = \frac{E_{ion}^2 \cdot \pi \cdot \epsilon_0}{Z \cdot e^3}, \tag{2.22}$$

from which the required laser intensity directly follows via equation 2.7. In the case of hydrogen ($E_{ion} = 13.6\,eV$), an intensity of $I = 1.4 \cdot 10^{14}\,W/cm^2$ would be needed for barrier suppression, while C^{4+} ($E_{ion} = 64.5\,eV$) would require $I = 4.3 \cdot 10^{15}\,W/cm^2$.

To estimate whether the ionization is dominated by MPI or TI, the so-called Keldysh parameter can be considered, which is defined as [68]

$$\gamma_k = \sqrt{\frac{E_{ion}}{2 \cdot \phi_{pond}}} = \sqrt{\frac{\epsilon_0 \cdot m_e \cdot c \cdot \omega^2}{e^2} \frac{E_{ion}}{I}}, \tag{2.23}$$

where ϕ_{pond} is the ponderomotive potential which is defined as $\vec{F}_{pond} = -\vec{\nabla}\phi_{pond}$. For the case $\gamma_k >> 1$, MPI is the important mechanism while for $\gamma_k << 1$ TI will dominate. Schematics of the optical ionization mechanisms are illustrated in figure 2.1.

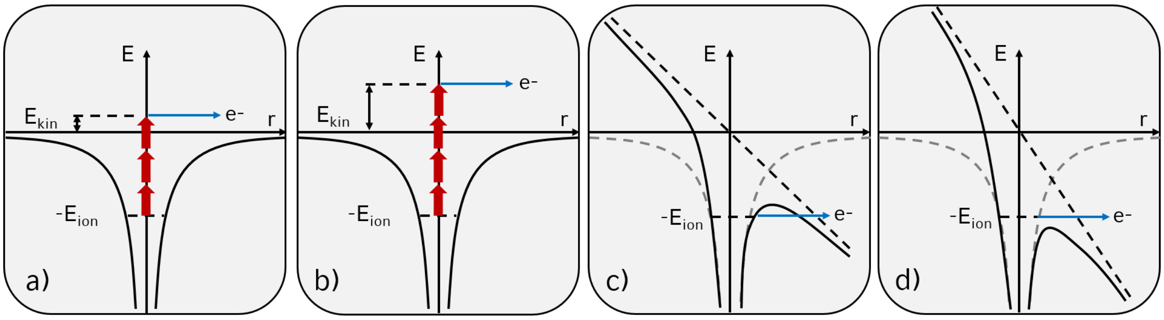

Figure 2.1: Illustration of optical ionization mechanisms: a) Multiphoton Ionization: the electron absorbs the minimum number of photons such that its energy is above the ionization energy E_{ion}. The resulting energy difference is transferred to the electron as kinetic energy. b) Above Threshold Ionization: The electron absorbs more than the required number of photons, inheriting the additional energy as kinetic energy. c) Tunnel Ionization: The potential barrier is modified by the linear potential of the laser. The electron can tunnel through the lowered barrier. d) Barrier Suppression Ionization: The potential barrier is lowered by the potential of the laser such that the electron becomes quasi-free.

Collisional Ionization

Collisional Ionization occurs when electrons (or other particles) with kinetic energies beyond the ionization threshold collide with atoms and becomes increasingly relevant the higher the density of the target. This mechanism is strongly dependent on the electron density and the energy of the electrons. Accounting for a velocity distribution of the electrons, the rate of ionizing collisons can be written as

$$w = n_e \cdot \langle \sigma_i v_e \rangle, \tag{2.24}$$

where n_e is the density and v_e the velocity of colliding electrons and σ_i is the ionization cross section, given by the Lotz formula for the case $E_{kin} >> E_{ion}$ as [71, 72]

$$\sigma_i = a_i \cdot q_i \frac{ln\left(E_{kin}/E_{ion}\right)}{E_{kin} \cdot E_{ion}}, \tag{2.25}$$

where a_i is an emipirical constant [71] and q_i is the number of electrons in the ions outer shell. For a Maxwellian energy distribution of the electrons the ionization rate yields [73]

$$w_{thermal} = \frac{n_e \cdot a_i \cdot q_i}{E_{ion}\sqrt{k_B T_e}} \int\limits_{E_{ion}/k_B T_e}^{+\infty} \frac{e^{-x}}{x} dx. \tag{2.26}$$

This rate only accounts for collisions caused by electrons with a thermal energy high enough to cause ionization. However, the kinetic energy component of the oscillatory electron motion in the laser field has to be considered as well. Following the argumentation of [73] and using $v_e\left(t\right) = \frac{eE_0}{m_e\omega} sin\left(\omega t\right)$, the cycle-averaged ionization rate becomes

$$w_{laser} = \frac{n_e \cdot a_i \cdot q_i}{\pi \cdot E_{ion} \cdot \sqrt{m_e \cdot \phi_{pond}}} \int\limits_{E_{ion}}^{2\phi_{pond}} \frac{ln\left(E_{kin}/E_{ion}\right)}{2 \cdot E_{kin}} \frac{1}{\sqrt{1 - \frac{E_{kin}}{2\phi_{pond}}}} dE_{kin}. \tag{2.27}$$

When a sufficient number of electrons is released from the target and heated effectively, collisional ionization can produce high charge states at intensities much lower than required for field ionization [74].

2.4 Plasma

[3]Having introduced the main mechanisms that show how matter can be ionized by interaction with high-intensity lasers, the main feature resulting from this interaction, the plasma, can now be described. A plasma can be defined as *"a quasineutral gas of charged and neutral particles which exhibits collective behavior"* [75]. Due to mobility of charged parts within the plasma, local accumulations of charges can occur. Furthermore, moving charges generate magnetic fields. The associated forces can influence charged particles over a long range and consequently, the plasma reacts collectively to disturbances. As the plasma has been created from neutral matter, the total number of positive and negative charges is equal, thus the plasma is observed neutral over large distances. The plasma tends to preserve neutrality by shielding local charge concentrations or external potentials. As the ions are much heavier, the reaction of the plasma is mostly governed by the electrons while the ions form an uniform background. The distance on which shielding decreases the potential to 1/e is the Debye length

$$\lambda_D = \sqrt{\frac{\epsilon_0 \cdot k_B \cdot T_e}{n_e \cdot e^2}}, \tag{2.28}$$

where n_e is the electron density. A denser plasma has a shorter Debye length since more electrons per volume are available for shielding. The term quasi-neutrality can thus be understood that on scales much larger than λ_D the plasma appears neutral

---

[3] This section follows [75]

due to shielding while on shorter scales high fields can occur.

In the case of an external field (e.g. a laser) acting on the plasma, electrons will be displaced, resulting in the plasma trying to restore neutrality by pulling back the electrons. Overshooting on the way back to their initial position will then lead to oscillations of the electrons with the so-called electron plasma frequency

$$\omega_{p,e} = \sqrt{\frac{n_e \cdot e^2}{\epsilon_0 \cdot m_e}}. \tag{2.29}$$

In the relativistic case, the electron mass needs to be scaled with $\langle\gamma\rangle$, the time averaged Lorentz factor. The inverse of this frequency is the time the electrons with a thermal velocity $v_{e,th} = \lambda_D \cdot \omega_{p,e} = \sqrt{k_B T_e / \left(\langle\gamma\rangle m_e\right)}$ need to recover quasi-neutrality on the scale of the Debye length. From this it becomes clear that external fields can be shielded from the plasma if the plasma frequency is higher than the external field frequency ω. Since $\omega_{p,e}$ is depending on the electron density, it is useful to define the threshold where both frequencies become equal:

$$n_e = \langle\gamma\rangle \frac{\epsilon_0 \cdot m_e \omega^2}{e^2} = \langle\gamma\rangle \frac{1.1 \cdot 10^{21}\, cm^{-3}}{\lambda^2\, [\mu m^2]} = n_c. \tag{2.30}$$

This density threshold is called critical density n_c. A plasma with a density below n_c is called underdense, while in the case $n_e > n_c$ the plasma is overdense.

Propagation of transverse electromagnetic waves in a plasma

The propagation of transverse electromagnetic waves in a vacuum is with a phase velocity $v_{ph} = c$ and the dispersion relation is $\omega = kc$. In the case of a plasma, the current density $\vec{j} \neq 0$. When neglecting losses (for example due to collisions), the dispersion relation for the propagation of electromagnetic waves in a plasma yields [75]

$$\omega^2 = \omega_p^2 + c^2 \cdot k^2. \tag{2.31}$$

Here, $\omega_p = \omega_{p,e}$ as the ion contribution can be neglected due to their high mass. The phase velocity in a plasma becomes

$$v_{ph} = \frac{\omega}{k} = \frac{c}{\sqrt{1 - \frac{\omega_p^2}{\omega^2}}} = \frac{c}{\eta}, \tag{2.32}$$

with the plasma refractive index $\eta = \sqrt{1 - \omega_p^2/\omega^2} = \sqrt{1 - n_e/n_c}$. For an underdense plasma ($\omega > \omega_p$), the refractive index has a real value < 1. An electromagnetic wave can therefore propagate in a plasma with a phase velocity greater than c. The group velocity however is always smaller than c as

$$v_{gr} = \frac{d\omega}{dk} = \frac{k \cdot c^2}{\omega} = \eta \cdot c. \tag{2.33}$$

In an overdense plasma ($\omega < \omega_p$), η becomes purely imaginary, the wave can no longer propagate through the plasma and becomes evanescent. Taking the complex notation of the field and considering propagation along the z-axis with a steplike density-gradient one finds:

$$e^{ikz} = e^{-|k|z} = e^{-\frac{z}{l_s}}. \tag{2.34}$$

$l_s = c/\sqrt{\omega_p^2 - \omega^2}$ is the so-called skin depth, at which the field drops to 1/e inside the overcritical region. For highly overdense plasmas ($\omega_p >> \omega$), the skin depth can be approximated by $l_s \approx c/\omega_p$.

2.5 Laser Absorption

The plasma can gain energy from the laser via a variety of absorption mechanisms. A general distinction can be made between collisional and collisionless types of energy absorption. In the following, the main mechanisms for the case of dense plasmas are briefly explained. For a more detailed description of the relevant processes, see, e.g., [76].

Inverse Bremsstrahlung

Energy can be absorbed via collisions of electrons, oscillating in phase with the laser field, and ions by transfering part of the quiver energy into random motion energy, thereby heating the plasma. The average heating rate is obtained by [77]

$$\frac{dE_e}{dt} = 2 \cdot \phi_{pond} \cdot \langle \nu_{ei} \rangle, \tag{2.35}$$

where E_e is the gained energy of the electron and $\langle \nu_{ei} \rangle$ is the cycle-averaged electron-ion collsion frequency which for a Maxwellian velocity distribution yields [77]

$$\langle \nu_{ei} \rangle = \frac{4\sqrt{2\pi}}{3} \frac{Z^2 \cdot n_i \cdot e^4 \cdot ln\Lambda}{(4 \cdot \pi \cdot \epsilon_0)^2 \sqrt{m_e} \left(k_B \cdot T_e\right)^{3/2}}, \tag{2.36}$$

with the electron density in m^{-3} and $ln\Lambda = ln\left(12\pi\lambda_D^3 n_e/Z\right)$ being the Coulomb logarithm. Using the common units $n\,[cm^{-3}]$ and $T_e\,[eV]$, $\langle \nu_{ei} \rangle$ can be expressed as [78]

$$\langle \nu_{ei} \rangle\,[1/s] \approx 3 \cdot 10^{-6} \frac{Z^2 \cdot n_i\,[cm^{-3}]}{\left(T_e\,[eV]\right)^{3/2}} \cdot ln\Lambda. \tag{2.37}$$

When the oscillatory motion increases with higher laser intensity, the thermal energy and the quiver energy become comparable. To account for a non-Maxwellian distribution, the collision frequency then has to be multiplied with an additional correction factor [79] $F = \left(1 + v_{e,osc}/\left(3 \cdot v_{e,th}^2\right)\right)^{-3/2}$, where $v_{e,osc} = eE_0/\left(m_e\omega\right)$ is the electron quiver velocity. Moreover, when the electron energy is dominated by the quiver energy, rising intensities will increase electron temperatures, leading to a decrease of the collision frequency. Thus, at intensities above $10^{15}\,W/cm^2$, collisional absorption begins to abate and other processes become dominant.

Resonance Absorption

At higher intensities, absorption is no longer determined by single particle effects (collisions) but is governed by collective effect (collisionless). Considering a dense plasma with continuously increasing density, electromagnetic waves can propagate up to the critical density ($n_e = n_c$) where they are reflected. In the case of an inhomogeneous plasma (the plasma may have already expanded due to heating via collision absorption) with a density gradient ∇n_e along e.g. the z-axis, an electrostatic oscillation in the form of an electron plasma wave can be exited under certain conditions, a process called **Resonance Absoprtion**. For this mechanism, the electric field component along the density gradient drives the coherent oscillation of the density perturbation. Thus, oblique incidence of the wave under an angle θ is required, where θ is defined as the angle between the wave vector $\vec{k}$ and the direction of the density gradient. If the conditions are met, the incident wave will propagate until it reaches a density of

$$n_e = n_c \cdot cos^2\theta. \tag{2.38}$$

The wave will be partially reflected but a certain amount can tunnel towards the region of critical density. At this point the laser will cause fluctuations of the charge density with the plasma frequency. The plasma will respond resonantly and a plasma wave can be excited. This wave can be absorbed by the plasma via collisions, electron trapping or wavebreaking, depending on the intensity regime [77]. The fractional absorption f_A can be estimated by [78]

$$\begin{aligned} f_A &\approx \phi^2\left(\tau\right)/2, \\ \phi\left(\tau\right) &\approx 2.3 \cdot \tau \cdot e^{-2\tau^3/3}, \end{aligned} \tag{2.39}$$

where $\tau = \left(\omega L/c\right)^{1/3} sin\theta$ is defined by the angle of incidence θ and the plasma scale length L (distance from the plasma-vacuum boundary to the critical density). The optimum angle of incidence for resonance absorption dependes on the plasma scale length and approximately yields [78]

$$\theta_{op} \approx sin^{-1}\left(0.8 \cdot \left(\frac{c}{\omega L}\right)^{1/3}\right). \tag{2.40}$$

Vacuum/Brunel Heating

Considering the above mechanism in the case of very steep gradients, the oscillation amplitude of electrons along the gradient can exceed the plasma scale length, the electrons hence behave like individual particles (or particle bunches) rather than a fluid in which waves can be launched. However, absorption is still possible: thermal electrons at the edge of the plasma-vacuum boundary can be dragged out of the plasma within half a laser cycle and driven back into the overdense region when the field changes sign. As the electron can penetrate across this boundary into the plasma while the electric field is shielded over the skin depth, the electron can transfer energy to the plasma via collisions. This effect was first described by Brunel in 1987 [80]. Electrons, entering the plasma, have velocities close to the quiver velocity in vacuum. Therefore the fractional absorption rate can be obtained from the ratio of the absorberd power per laser cycle and incoming laser power as [76]

$$f_{vac} = \frac{P_a}{P_L} = \frac{eE_d^3}{16\pi^2 m\omega} \cdot \frac{8\pi}{cE_L^2 cos\theta} = \frac{4}{\pi}\frac{sin^3\theta}{cos\theta} a_0, \tag{2.41}$$

with $E_d = 2E_L sin\theta$, where E_L is the electric field of the incoming laser. It is clear that f_{vac} can obtain high values for increasing laser intensity (a_0) and angle of incidence (θ) and ultimately these values can become too high (>1). Thus appropriate corrections need to be made to account for relativistic effects and imperfect reflection of the driving field (see [80]).

Relativistic j x B Heating

At very high laser intensities ($a_0 >> 1$) it was already shown that the v x B term in equation 2.11 dominates the relativistic motion of a single (free) electron in vacuum. At a vacuum-plasma boundary, this v x B force hence dominates the generation of electrons injected across the vacuum-plasma interface and **j x B heating** [81] becomes the major absorption mechanism. It is closely related to the process of Brunel heating with the main difference being that the force driving electrons into the plasma is no longer the electric field but the v x B component. The dynamics follow a similar behaviour, although the oscillation frequency is now 2ω and the mechanism scales as a_0^2 (see equation 2.16). In contrast to resonance absorption and Brunel heating, this mechanism works for any polarization except circular and provides highest absorption for normal incidence.

All mechanisms presented here (and many more, e.g. anomalous skin effect [82] and sheath inverse bremsstrahlung [83]) describe (mostly qualitatively) how the energy of a laser pulse can be transferred to plasma electrons. In reality, however, the plasma properties change rapidly and several processes can occur at the same time or boundaries are not very strict (e.g. long versus short plasma scale length, v x B versus E). Nevertheless, certain distinctions can be made that help to determine the dominant process. For low laser intensities (I $< 10^{15}\,W/cm^2$) and $v_{e,osc} << v_{e,th}$, absorption occurs mainly via collisions. For increasing intensities, resonance absorption and Brunel heating dominate. Long density gradients of the plasma favor resonance absorption, while for steep density gradients absorption is governed by the Brunel mechanism [84]. In the case of relativistic intensities ($a_0 >> 1$) it could be shown that experimental results can be best explained by j x B heating [85]. Considering the experimental parameters of this work, the peak intensity of $10^{16}\,W/cm^2$ indicates that resonance absorption or Brunel heating may be the dominant mechanims. Due to the spherical geometry of the target, all angles of incidence are present. Thus absorption will be strongly dependend on the plasma scale length at the time when the fs-short laser pulse interacts with the target.

2.6 Plasma Expansion

[4] The description of plasma dynamics is a challenging task. The motion of single charged particles can be described by equation 2.11. In dense plasmas, however, collective effects occur due to the large number of interacting particles. One attempt to model the dynamics is kinetic theory, which describes the plasma behavior by means of particle distribution functions $f\left(\vec{r},\vec{v},t\right)$. This distribution has to satisfy the Boltzmann equation:

$$\frac{\partial f}{\partial t}+\vec{v}\cdot\vec{\nabla}_r f+\frac{\vec{F}}{m}\cdot\vec{\nabla}_v f=\left(\frac{\partial f}{\partial t}\right)_{coll}. \tag{2.42}$$

Here, $\vec{F}$ is the force acting on the particles and $\left(\partial f/\partial t\right)_{coll}$ describes the influence of collisions on f. Neglecting collisions in the case of a hot plasma and assuming a purely electromagnetic force, equation 2.42 reduces to the Vlasov equation

$$\frac{\partial f}{\partial t}+\vec{v}\cdot\vec{\nabla}f+\frac{q}{m}\left(\vec{E}+\vec{v}\times\vec{B}\right)\cdot\vec{\nabla}_v f=0. \tag{2.43}$$

Together with Maxwell's equations, 2.43 provides a full description of the collisionless plasma behaviour. If one focuses in particular on macroscopic (averaged) values of the plasma, a fluid description is often sufficient. Here the distribution function is assumed to be Maxwellian everywhere, thus it is defined by a single temperature T. A simple approach is to treat electrons and ions as two seperate, but intersecting fluids. The relevant equations can be obtained by taking velocity moments $M_n=\int v^n f\left(v\right)dv$ of the Vlasov equation. This results in the continuity equation (M_0)

$$\frac{\partial n}{\partial t}+\vec{\nabla}\cdot\left(n\vec{u}\right)=0 \tag{2.44}$$

and the equation of motion (M_1)

$$m\cdot n\cdot\left(\frac{\partial\vec{u}}{\partial t}+\left(\vec{u}\cdot\vec{\nabla}\right)\vec{u}\right)=q\cdot n\cdot\left(\vec{E}+\vec{u}\times\vec{B}\right)-\nabla p, \tag{2.45}$$

where n is the particle density distribution and $\vec{u}$ the velocity field of the fluid. Thermal motion is taken into account by the pressure term ∇p. In order to form a closed set of equations, p needs to be defined. This could be achieved via the energy equation (M2), however, this would include a term for the heat flow which again requires a new equation. The growing set of equations can be reduced by making simplifying

---

[4] This section follows the argumentation of [75] and [78]

assumptions about the heat flow, obtaining the equation of state. In the isothermal case this reads

$$p = n \cdot k_B \cdot T, \tag{2.46}$$

while in the adiabatic case one obtains

$$\frac{p}{n^\gamma} = const., \tag{2.47}$$

where γ is the ratio of specific heats, determined by the degrees of freedom N ($\gamma = (N+2)/N$).

Finding analytic solutions for above-mentioned equations is extremely difficult. Here, simulations play a key role in finding numerical solutions under specified conditions. Complex systems and the interplay of various effects can nowadays be calculated with resonable computational effort. In the realm of collisionless kinetic theory, Particle-In-Cell simulations (PIC) are a powerful tool to model the laser-plasma interaction. In the macroscopic fluid model, hydrodynamic codes (e.g. RALEF [86]) or magnetohydrodynamic simulations (e.g. FLASH [87]) provide insight into the plasma dynamics on larger scales.

Although the interaction and dynamics is best modeled with such simulation tools, it is possible to gain insight into the plasma behaviour by making some simplifying assumptions. Two simple models that describe the expansion of a spherical plasma by pressure forces are introduced in the following, closely following the argumentation of [88].

Hydrodynamic Expansion

One driving force of expansion is the hydrodynamic pressure by heated electrons. This mechanism may be interpreted as hot electrons expanding towards the vacuum but not being energetic enough to leave the plasma due to charge seperation fields building up. Accordingly, the cold ions are dragged along by the expanding electrons. Since the net charge of the plasma is almost neutral on scales larger than the Debye length, this kind of expansion is also called quasi-neutral expansion.

Assuming that the temperature is uniform over the whole plasma (frequent collisions to establish temperature), the pressure caused by the electrons reads

$$p_e = n_e \cdot k_B \cdot T_e. \tag{2.48}$$

An adiabatic increase dV of the plasma volume V due to expansion results in a temperature decrease of the electrons dT_e:

$$V \cdot n_e \cdot \frac{3}{2} \cdot k_B \, dT_e = -p_e \, dV. \tag{2.49}$$

This expression is valid under the assumption that the electron temperature establishes faster than the plasma expansion. For a plasma volume of $4/3 \cdot \pi \cdot r^3$ one thus finds

$$dT_e = -2 \cdot T_e \frac{dr}{r}. \tag{2.50}$$

Integration of equation 2.50 provides the relation between plasma radius and electron temperature:

$$T_e = T_{e0} \left(\frac{r_0}{r} \right)^2, \tag{2.51}$$

where T_{e0} and r_0 represent the initial temperature and radius of the plasma. Treating both the electrons and ions as charged fluids with homogeneous, temporally decreasing density, energy conservation demands

$$n_i \frac{d}{dt} \left(\frac{3}{2} \cdot k_B \cdot T_i \right) = -n_e \frac{d}{dt} \left(\frac{3}{2} \cdot k_B \cdot T_e \right). \tag{2.52}$$

Using equations 2.50 and 2.51, 2.52 becomes

$$\frac{dT_i}{dt} = 2 \frac{n_e}{n_i} \frac{T_{e0}}{r} \left(\frac{r_0}{r} \right)^2 \frac{dr}{dt}. \tag{2.53}$$

For ions at the boundary of the plasma, the relation $1/2 \cdot m_i \cdot (dr/dt) = 3/2 \cdot k_B \cdot T_i$ applies. Taking the temporal derivative of this equation and inserting it into 2.53, the equation for surface ion motion is obtained:

$$m_i \frac{d^2 r}{dt^2} = \frac{3 \cdot k_B \cdot T_{e0} \cdot r_0^2 \cdot \left(Z - \frac{Q}{N_i} \right)}{r^3}. \tag{2.54}$$

Here $n_e = n_i \cdot (Z - Q/N_i)$ was used, with Q being the number of electrons that have escaped the plasma and N_i is the total number of ions. If Z, Q and N_i are assumed to have no time dependence, equation 2.54 can be integrated towards

$$\left(\frac{dr}{dt}\right)^2 = \frac{3 \cdot k_B \cdot T_{e0} \cdot \left(Z - \frac{Q}{N_i}\right)}{m_i} \cdot \left(1 - \left(\frac{r_0}{r}\right)^2\right) \tag{2.55}$$

under the condition dr/dt = 0 at t = 0. In the case of $r \to \infty$, the ion fluid expands with a velocity

$$v_{i,\infty} = \sqrt{\frac{3 \cdot k_B \cdot T_{e0} \cdot \left(Z - \frac{Q}{N_i}\right)}{m_i}}, \tag{2.56}$$

which is well know as the ion sound velocity.

Coulomb Explosion

Another type of pressure emerges if a sufficient number of hot electrons surpass the charge seperation field and leave the plasma completely. A surplus of positive charges leads to a repulsion of ions and thus explosion. Treating the plasma as a spherical capacitor with radius r and a number of Q charges on the surface, the corresponding pressure can be calculated as

$$p_{coulomb} = \frac{Q^2 \cdot e^2 \cdot k_e}{8 \cdot \pi \cdot r^4}, \tag{2.57}$$

where $k_e = 1/(4\pi\epsilon_0)$ is the Coulomb constant. Similar to the previous case, an equation of motion for an ion sitting on the surface of an ionized sphere is obtained:

$$m_i \cdot \frac{d^2r}{dt^2} = \frac{Q \cdot Z \cdot e^2 \cdot k_e}{r^2}. \tag{2.58}$$

Assuming temporal independence of Q and Z, this results in [88]

$$\left(\frac{dr}{dt}\right)^2 = \frac{2 \cdot Q \cdot Z \cdot e^2 \cdot k_e}{m_i \cdot r_0}\left(1 - \frac{r_0}{r}\right). \tag{2.59}$$

Comparing 2.55 and 2.59 clearly shows a different scaling with the plasma radius r as a factor describing the expansion behaviour. It is therefore essential to verify which of the two regimes applies. Such an estimate will be discussed in context with experimental results in chapter 5.

2.7 Scalar Diffraction Theory

[5]The investigation of laser generated plasmas is often performed by external electromagnetic pulses, as already introduced in chapter 1. By studying these pulses in detail, one can derive relevant plasma parameters. As the measurement is performed at some distance from the interaction area, it is essential to have a precise understanding of the propagation behaviour. A powerful tool to describe all relevant physical effects is the scalar diffraction theory.

In reality, the electric and magnetic fields are vector fields whose relationship is described by Maxwell's equations 2.1. The propagation in homogeneous, isotropic media is determined by the wave equations 2.2. Assuming that all scalar field components behave in the same way, the two wave equations can be replaced by a single scalar wave equation:

$$\nabla^2 u\left(\vec{r},t\right) - \frac{\eta^2}{c^2}\frac{\partial^2 u\left(\vec{r},t\right)}{\partial t^2} = 0. \tag{2.60}$$

Here, $u\left(\vec{r},t\right)$ respresents each of the scalar field components. In the case of a monochromatic wave, one can define $u\left(\vec{r},t\right)$ as

$$u\left(\vec{r},t\right) = Re\left[U\left(\vec{r}\right)\cdot e^{-i\omega t}\right], \tag{2.61}$$

where $U\left(\vec{r}\right)$ is the complex-valued amplitude. Inserting this expression into 2.60 yields

$$\left(\nabla^2 + k^2\right)U\left(\vec{r}\right) = 0, \tag{2.62}$$

with $k = \eta\omega/c$. 2.62 is the time-independent Helmholtz equation.

Kirchhoff integral theorem

It is possible to determine $U\left(\vec{r}\right)$ at a point P_0 in terms of the field on a surface S enclosing P_0 and its first derivative. This is known as the integral theorem of Kirchhoff [89]:

$$U\left(P_0\right) = \frac{1}{4\pi}\iint\limits_S\left(\frac{\partial U}{\partial n}\cdot\frac{e^{ikr_{01}}}{r_{01}} - U\frac{\partial}{\partial n}\frac{e^{ikr_{01}}}{r_{01}}\right)dS, \tag{2.63}$$

where r_{01} is the distance from a surface element to the point P_0 and $\frac{\partial}{\partial n}$ is the differentiation along the surface normal $\vec{n}$. Depending on the direction of $\vec{n}$ (inward or

---

[5] This section follows [89].

outward), the integral switches sign. A detailed derivation of the theorem via a Green's function approach can be found in various textbooks (e.g. [89, 90]).

Fresnel-Kirchhoff diffraction formula

Using 2.63, one can now consider the simple case of diffraction by an aperture in an infinite plane screen, where the field shall be obtained at a point P_0 behind the screen. In this context, the enclosing surface splits up into two parts: a plane surface S_1 directly behind the screen and a circular segment S_2 with radius R around P_0 that closes the surface. Thus 2.63 becomes

$$U\left(P_0\right) = \frac{1}{4\pi} \iint\limits_{S_1+S_2} \left(\frac{\partial U}{\partial n} \cdot \frac{e^{ikr_{01}}}{r_{01}} - U \frac{\partial}{\partial n} \frac{e^{ikr_{01}}}{r_{01}} \right) dS. \tag{2.64}$$

With the help of various conditions (namely the Sommerfeld radiation condition and the Kirchhoff boundary conditions, see [89] for more details) the integral can be reduced to

$$U\left(P_0\right) = \frac{1}{4\pi} \iint\limits_{\Sigma} \left(\frac{\partial U}{\partial n} \cdot \frac{e^{ikr_{01}}}{r_{01}} - U \frac{\partial}{\partial n} \frac{e^{ikr_{01}}}{r_{01}} \right) dS, \tag{2.65}$$

where Σ represents the surface of the aperture. A further reasonable approximation is that the distance r_{01} will at most times be considerably larger than the optical wavelength, i.e. $k >> r_{01}^{-1}$. Assuming that the aperture is illuminated by a spherical wave originating from a point P_2,

$$U\left(P_1\right) = A \frac{e^{ikr_{21}}}{r_{21}}, \tag{2.66}$$

whereby the same condition, $k >> r_{21}^{-1}$, applies. This results in the Fresnel-Kirchhoff diffration formula [89]:

$$\begin{aligned} U\left(P_0\right) &= \frac{A}{i\lambda} \iint\limits_{\Sigma} \frac{e^{ik(r_{21}+r_{01})}}{r_{21}r_{01}} \left(\frac{cos\left(\vec{n}, \vec{r_{01}}\right) - cos\left(\vec{n}, \vec{r_{21}}\right)}{2} \right) dS \\ &= \iint\limits_{\Sigma} U'\left(P_1\right) \frac{e^{ikr_{01}}}{r_{01}} dS. \end{aligned} \tag{2.67}$$

Based on the latter expression one can deduce that the field at P_0 results from an infinite amount of point sources within the aperture Σ, whose phase and amplitude are defined by $U'\left(P_1\right)$. This perfectly resembles Huygens principle.

Rayleigh-Sommerfeld diffraction formula

Although the Fresnel-Kirchhoff diffraction formula provides excellent agreement with experimental results, the boundary conditions applied by Kirchhoff provoke some mathematical difficulties. A more consistent solution is given by the Rayleigh-Sommerfeld diffraction formula which follows from choosing a more appropiate Green's function and reads

$$\begin{aligned} U_1\left(P_0\right) &= \frac{A}{i\lambda} \iint_{\Sigma} \frac{e^{ik(r_{21}+r_{01})}}{r_{21}r_{01}} cos\left(\vec{n}, \vec{r_{01}}\right) dS, \\ U_2\left(P_0\right) &= -\frac{A}{i\lambda} \iint_{\Sigma} \frac{e^{ik(r_{21}+r_{01})}}{r_{21}r_{01}} cos\left(\vec{n}, \vec{r_{21}}\right) dS. \end{aligned} \tag{2.68}$$

Comparing this result with the one obtained by Kirchhoff, one notices that both differ only in their cosine terms (also called obliquity factor). Similarly, Huygens principle is obtained by

$$U\left(P_0\right) = \frac{1}{i\lambda} \iint_{\Sigma} U\left(P_1\right) \frac{e^{ikr_{01}}}{r_{01}} cos\left(\vec{n}, \vec{r_{01}}\right) dS. \tag{2.69}$$

Angular spectrum

The angular spectrum of the wave provides a different approach to solving the problem of wave propagation and diffraction. An arbitrary monochromatic field distribution can be expressed as the sum of an infinite amount of plane waves, each traveling in a different direction. Thus the distribution can be determined at an observation point by accounting for the contribution of each plane wave in this point after propagation. An undefined wave with a propagation component along z may be expressed in the xy-plane by a complex distribution $U\left(x, y, 0\right)$ at z = 0. The superposition of plane waves reads

$$U\left(x, y, 0\right) = \int_{-\infty}^{\infty} \int_{-\infty}^{\infty} A\left(f_x, f_y, 0\right) \cdot e^{i2\pi(f_x x + f_y y)} df_x df_y, \tag{2.70}$$

where $A\left(f_x, f_y, 0\right)$ is the Fourier transform of $U\left(x, y, 0\right)$ with spatial frequencies f_x and f_y. Expressing the wavevector of a simple plane wave in terms of direction cosines α, β and γ [89] allows to define the spatial frequencies as $f_x = \alpha/\lambda$ and $f_y = \beta/\lambda$.

Thus the angular spectrum of $U\left(x,y,0\right)$ reads

$$A\left(\frac{\alpha}{\lambda},\frac{\beta}{\lambda},0\right)=\int_{-\infty}^{\infty}\int_{-\infty}^{\infty}U\left(x,y,0\right)\cdot e^{-i2\pi\left(\frac{\alpha}{\lambda}x+\frac{\beta}{\lambda}y\right)}dxdy. \tag{2.71}$$

The field distribution in a parallel plane along z can then be found via

$$U\left(x,y,z\right)=\int_{-\infty}^{\infty}\int_{-\infty}^{\infty}A\left(\frac{\alpha}{\lambda},\frac{\beta}{\lambda},z\right)\cdot e^{i2\pi\left(\frac{\alpha}{\lambda}x+\frac{\beta}{\lambda}y\right)}d\frac{\alpha}{\lambda}d\frac{\beta}{\lambda}. \tag{2.72}$$

As U is subject to the Helmholtz equation, one finds that A must fulfill

$$\frac{d^2}{dz^2}A\left(\frac{\alpha}{\lambda},\frac{\beta}{\lambda},z\right)+\left(\frac{2\pi}{\lambda}\right)^2\left(1-\alpha^2-\beta^2\right)A\left(\frac{\alpha}{\lambda},\frac{\beta}{\lambda},z\right)=0, \tag{2.73}$$

which results in a solution for A in the form of

$$A\left(\frac{\alpha}{\lambda},\frac{\beta}{\lambda},z\right)=A\left(\frac{\alpha}{\lambda},\frac{\beta}{\lambda},0\right)e^{\frac{i2\pi}{\lambda}\sqrt{1-\alpha^2-\beta^2}z}. \tag{2.74}$$

The relation between $A\left(\frac{\alpha}{\lambda},\frac{\beta}{\lambda},z\right)$ and $A\left(\frac{\alpha}{\lambda},\frac{\beta}{\lambda},0\right)$, often denoted as H, describes how the angular spectrum changes during propagation.

Fresnel and Fraunhofer approximation

Analytic evaluation of above formalisms can be quite challenging. Therefore, two approximations are commonly used in diffraction theory: the Fresnel approximation and the Fraunhofer approximation. Both can be used to reduce the Huygens-Fresnel formula 2.69 introduced earlier. Assuming an observation point P_0 in the xy-plane and a planar aperture in a parallel plane defined by ξ and ν with a distance z between both planes, the oblicity factor yields $cos\left(\vec{n},\vec{r_{01}}\right)=z/r_{01}$ and 2.69 becomes

$$U\left(x,y\right)=\frac{z}{i\lambda}\iint_{\Sigma}U\left(\xi,\nu\right)\frac{e^{ikr_{01}}}{r_{01}^2}d\xi d\nu, \tag{2.75}$$

where $r_{01}=z\sqrt{1+\left(\frac{x-\xi}{z}\right)^2+\left(\frac{y-\nu}{z}\right)^2}$. Taylor-expansion of this term allows for further simplification:

$$r_{01} \approx z\left(1+\frac{1}{2}\left(\frac{x-\xi}{z}\right)^2+\frac{1}{2}\left(\frac{y-\nu}{z}\right)^2+...\right). \tag{2.76}$$

For the $1/r_{01}^2$-component, it is acceptable to neglect all terms except the frist one, while in the exponential, quadratic terms need to be retained. Equation 2.77 thus becomes

$$U\left(x,y\right)=\frac{e^{ikz}}{i\lambda z}\int\limits_{-\infty}^{\infty}\int\limits_{-\infty}^{\infty}U\left(\xi,\nu\right)e^{\frac{ik}{2z}\left((x-\xi)^2+(y-\nu)^2\right)}d\xi d\nu, \tag{2.77}$$

which is know as the Fresnel diffraction integral. This expression is accurate for the observation plane being located in the near field, i.e. close to the aperture. The Fresnel approximation may also be applied to the angular spectrum. The square root term, describing relation between $A\left(\frac{\alpha}{\lambda},\frac{\beta}{\lambda},z\right)$ and $A\left(\frac{\alpha}{\lambda},\frac{\beta}{\lambda},0\right)$, can be simplified in the same way:

$$H=e^{ikz}\cdot e^{-\frac{i\pi z}{\lambda}\left(\alpha^2+\beta^2\right)}. \tag{2.78}$$

Thus, in the case of the angular spectrum, the Fresnel approximation is valid if the spectrum is restricted to small angles. This is also called the paraxial approximation.

If the distance between the observation plane and the source (aperture) is much larger than the source itself, the Fraunhofer approximation ($2z >> k\left(\xi^2+\nu^2\right)_{max}$) can be applied. In this scenario (also described as the far field), the quadratic terms of equation 2.76 can be neglegted and the equation for the field distribution reads

$$U\left(x,y\right)=\frac{e^{ikz}e^{\frac{ik}{2z}\left(x^2+y^2\right)}}{i\lambda z}\int\limits_{-\infty}^{\infty}\int\limits_{-\infty}^{\infty}U\left(\xi,\nu\right)e^{-ikz(x\xi+y\nu)}d\xi d\nu. \tag{2.79}$$

One may recognize that is expression is almost exactly the Fourier transform of the source (field distribution at the aperture).

Paraxial wave equation for inhomogeneous media

So far, all models above assume propagation in homogeneous media. The situation gets much more complicated if this is not the case. Considering a spatial dependence of the refractive index, the Helmholtz equation reads [91]

$$\left(\nabla^2 + k^2\left(\vec{r}\right)\right) U\left(x,y,z\right) = 0, \tag{2.80}$$

where $k\left(\vec{r}\right) = \eta\left(\vec{r}\right)\omega/c$. Using the ansatz $U\left(x,y,z\right) = U'\left(x,y,z\right)e^{i\langle k\rangle z}$, where $\langle k\rangle$ is spatial average of the wave number in the propagation volume, equation 2.80 yields:

$$\frac{\partial^2}{\partial z^2}U'\left(x,y,z\right) + 2i\langle k\rangle\frac{\partial}{\partial z}U'\left(x,y,z\right) + \nabla^2_{x,y}U'\left(x,y,z\right) + \left(k^2\left(\vec{r}\right) - \langle k\rangle^2\right)U'\left(x,y,z\right) = 0. \tag{2.81}$$

Using the slowly varying envelope approximation, which assumes that the wave envelope has only small changes during the period of a wavelength ($|\langle k\rangle U'| >> |\partial U'/\partial z|$) [91], the equation simplifies to the paraxial wave equation for inhomogeneous media

$$2i\langle k\rangle\frac{\partial}{\partial z}U'\left(x,y,z\right) + \nabla^2_{x,y}U'\left(x,y,z\right) + \left(k^2\left(\vec{r}\right) - \langle k\rangle^2\right)U'\left(x,y,z\right) = 0, \tag{2.82}$$

which can be applied to calculate the propagation under such conditions. In order to obtain the wave equation in terms of changes of the refractive index, one can utilize the common approximation $\eta = \sqrt{\epsilon_r}$ where ϵ_r is the relative permittivity. With this one finds $k^2\left(\vec{r}\right) = \langle k\rangle^2 + \langle k\rangle^2\Delta\epsilon\left(\vec{r}\right)$ [92]. Moreover, $\eta\left(\vec{r}\right) = \langle\eta\rangle\left(1 + \Delta\eta\left(\vec{r}\right)\right) \approx \sqrt{\epsilon_r} + \sqrt{\epsilon_r}\Delta\epsilon\left(\vec{r}\right)/2$, hence $\Delta\eta\left(\vec{r}\right) = \Delta\epsilon\left(\vec{r}\right)/2$. Finally, one obtains

$$2i\langle k\rangle\frac{\partial}{\partial z}U'\left(x,y,z\right) + \nabla^2_{x,y}U'\left(x,y,z\right) + 2\langle k\rangle^2\Delta\eta\left(\vec{r}\right)U'\left(x,y,z\right) = 0. \tag{2.83}$$

Chapter 3

Experimental Setup

Contents

3.1 High-Power Laser Systems (ZEUS) 35

3.2 Pump-Probe Setup of Levitating Spheres 41

3.3 Diagnostics 43

3.3.1 Pump 44

3.3.2 Probe 45

3.3.3 Laser Characterization 51

This chapter explains the experimental setup for the optical probing of the expanding microspheres. It will start with the general structure of today's high-power laser systems exemplified by the 3 TW laser ZEUS which was used for this experimental campaign. Subsequently, the experiment and the main diagnostics will be explained.

3.1 High-Power Laser Systems (ZEUS)

The world's first laser was developed by Theodore Maiman in 1960 [14]. It was based on stimulated emission, a concept theoretically described by Einstein [93] and experimentally proven by Ladenburg in 1928 [94]. The utilization of this process was incorporated into the name: light amplification by stimulated emission of radiation. Atoms not only can emit (or absorb) photons spontaneously but can also be stimulated to do so. These characteristics can be exploited to amplify light and provide the basis of every laser. Typically, three components are needed for the lasing process - a gain medium, a pump laser and a resonator (see figure 3.1). The pump laser transfers

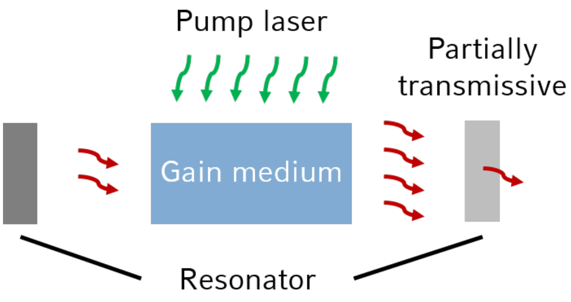

Figure 3.1: The basic setup of a laser is shown. The pump laser transfers energy into the gain medium. Photons that pass the gain medium are multiplied and are sent back to the gain medium multiple times by the resonator mirrors. One of these mirrors is partially transmissive to allow photons to escape the resonator.

energy into the gain medium by exiting atoms into states of higher energy. Population inversion is achieved if more atoms are in an exited state than in the ground state and stimulated emission can surpass absorption losses in the gain medium. When a photon with the correct wavelength (matching a decay channel of the atom) passes through the gain medium, the atoms return to their ground state and release photons with identical wavelength, direction and phase as the incident photon. By that, light is amplified each time passing the gain medium. The resonator often consists of two mirrors at both ends of the gain medium. Only photons with a certain direction are reflected back into the crystal and are amplified multiple times. The resonator can therefore be used to limit the emission direction of the laser. Additionally, one of the resonators has a slightly imperfect reflectivity which allows to couple out part of the light for further amplification.

Laser light can either be present in the form of a continuous wave (CW) or short pulses. The most common methods for the generation of laser pulses are Q-switching [16] and Mode-locking (e.g. [95]), where the latter is able to be produce ultrashort pulses in the femtosecond regime. The pulse duration τ is limited by the spectral bandwidth $\Delta\nu$ of the laser and is defined by the time-bandwidth product $\Delta\tau \cdot \Delta\nu$ where both values are considered in terms of full width at half maximum. The minimum of this product is determined by the shape of the spectrum (e.g. 0.441 for a Gaussian spectrum) and defines a lower limit for the achievable pulse duration for a given bandwidth. For example, Titanium-Sapphire (Ti:Sa) as a gain medium supports a broad spectral bandwidth of up to 300 nm, making it an excellent candidate for the generation of ultrashort laser pulses.

In theory, these pulses could be amplified further but due to the short pulse duration, they would quickly rise to problematic intensities in terms of nonlinearities and subsequent damage of laser optics during propagation and amplification. A potential solution for this problem would be to consistently increase the beam diameter to reduce the intensity, however this would lead to immense costs for optics and turns out to be a very uneconomical approach. Therefore, many modern laser systems use the principle of Chirped Pulse Amplification (CPA) [17] which was invented in 1985 and represents one of the major steps in the history of laser development. The principle of CPA is based on amplifying a temporally stretched laser pulse, distributing the pulse energy over a longer period of time and thereby significantly decreasing the pulse intensity. In order to achieve pulse stretching, CPA makes use of the broad spectral bandwidth of the laser pulses (typically 50 to 100 nm FWHM for Ti:Sa lasers). By inserting a grating or prism stretcher into the beam, a wavelength-dependent difference in path length can be generated, stretching the pulse duration to several hundred picoseconds. This allows for a much higher energy gain during the amplification process while simultaneously staying under the critical limits and keeping optics at a reasonable small size. In order to achieve the highest intensity in the end, the pulse is compressed back to its initial pulse duration after the last amplifier. The concept of CPA is illustrated in figure 3.2.

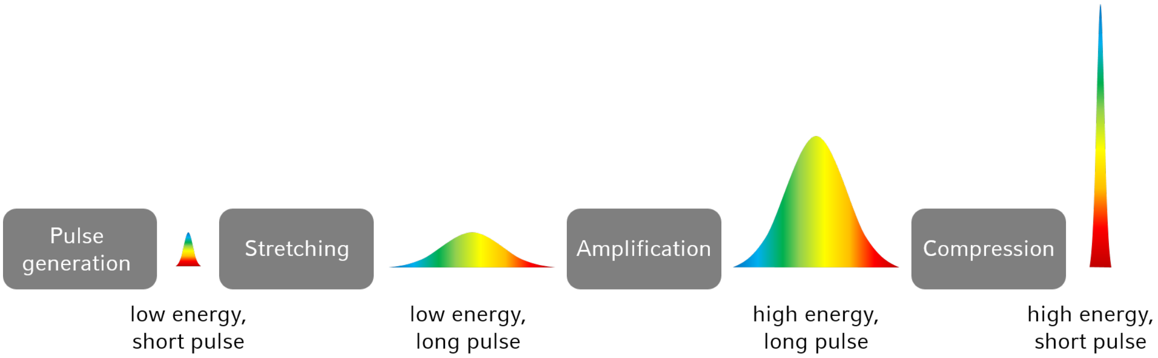

Figure 3.2: The basic principle of CPA: After generation, the short and low-energetic pulse is stretched in time. It is then amplified towards the desired energy and recompressed to its original pulse duration after the final amplifier.

The amplification of a laser pulse is achieved in the same way as its generation. Pump lasers transfer energy into the amplifier crystals where they invert the gain medium and the pulse is amplified by passing through the crystal multiple times. The gain G in a single pass is given by $G = \exp\left(J_{st}/J_{sat}\right)$ [96] where J_{st} is the fluence stored in the medium and J_{sat} is the saturation fluence (extraction of J_{sat} leads to a drop in medium inversion to 1/e). The number of passes in which the pulse can gain energy is limited by the amount of pump energy stored in the crystal, eventually leading to a saturation effect in the process where losses in the amplifier begin to surpass the amplification. At this point, the laser pulse is coupled out of the amplifier and sent to the next stage. Two of the most common layouts are the regenerative amplifier (Regen) [97] and the multipass amplifier [98] (see figure 3.3). The main difference between those two types is the beam path during amplification. In the Regen, the pulse is sent into the amplifier via a polarizing beamsplitter. Its polarization is flipped by a Pockels cell, trapping the pulse inside a cavity. After saturation occurs in the amplification process, the polarization is switched back and the pulse is kicked out by the beamsplitter. The repeating path of the Regen is often used for additional manipulation of the pulse spectrum or phase during the amplification. The multipass layout consists of multiple mirrors that fold the beam path such that it passes the crystal several times but always under slightly different angles. In contrast to the Regen, the number of passes can not be changed easily in this scheme.

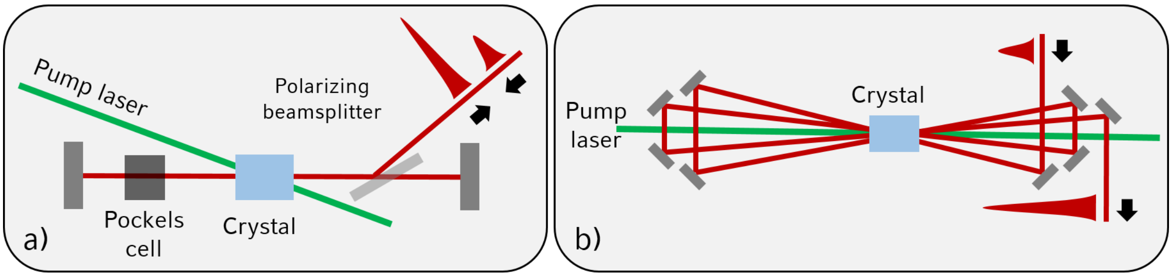

Figure 3.3: Amplifier schemes used in high power laser systems: a) Regen amplifier: the pulse is coupled into a cavity via polarization-switching in a Pockels cell. After several roundtrips through the amplifier crystal, the pulse is kicked out by switching back the polarization. b) Multipass amplifier: the pulse is sent through the amplifier crystal several times by folding the beam path with a set of mirrors.

After the final amplification stage, the pulse is re-compressed temporally, ideally to its initial duration. This is achieved by another set of gratings or prisms that compensate the dispersion that was introduced during the stretching of the pulse. As the pulse has a very high intensity at this point, all following optics have to be appropriately large in order to prevent non-linear effects such as self-focusing or self-phase modulation and potential damage of the optics. Above a certain intensity it is therefore necessary to put the compressor, all following guiding optics and the experimental setup into a vacuum system.

Zinths Extremly Useful Superlaser (ZEUS)

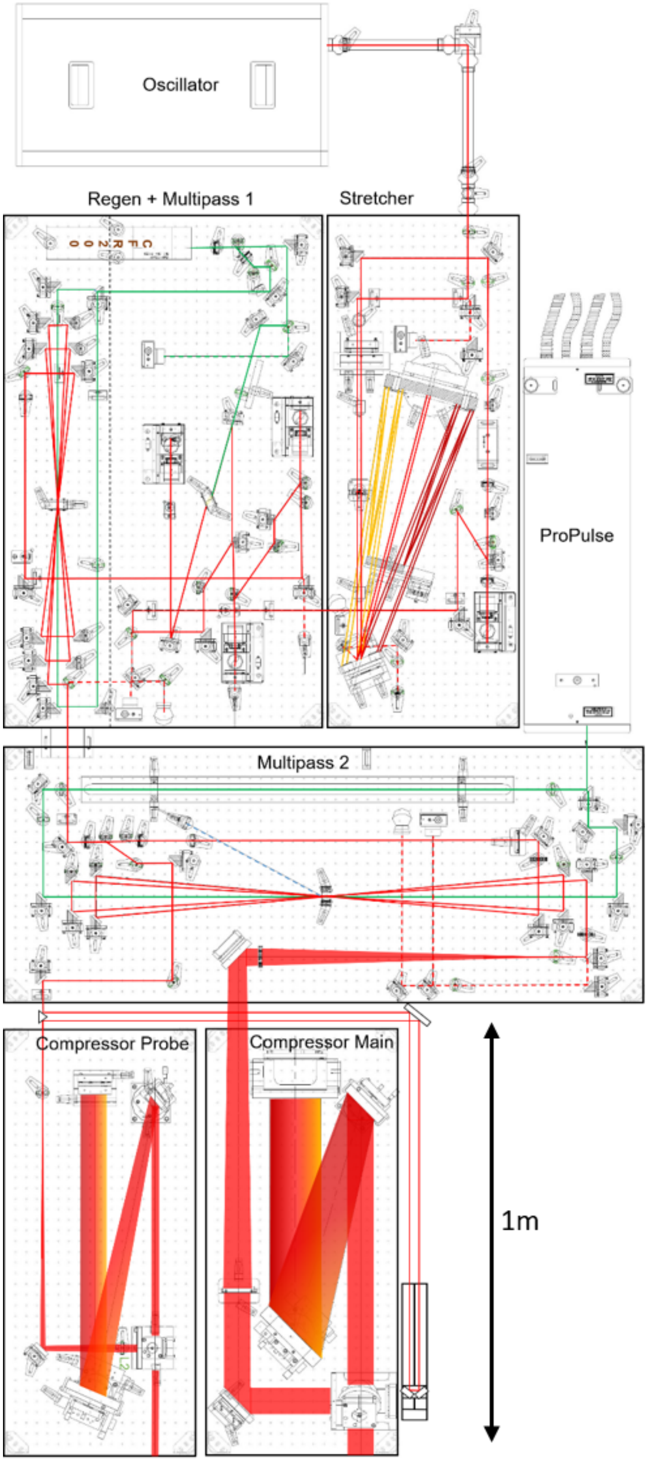

Figure 3.4: This sketch shows the layout of the ZEUS laser system. It consists of an oscillator, a stretcher, one regenerative and two multipass amplifier and two compressors. Additionally the motorized delay line for the probe pulse is depicted.

At the end of 2017, we gratefully received a TW-class laser system from the research group of Prof. Wolfgang Zinth, which was named "Zinths Extremely Useful Superlaser"

(ZEUS), in honor of its former owner. During the course of this work, the system was transferred to CALA and reassembled along with a laser laboratory and an associated target area. ZEUS is a 3 TW Ti:Sa dual-beam laser based on CPA and with a footprint of only five square meter a true tabletop system. Figure 3.4 shows a schematic of the complete layout. The first component is the oscillator with a Ti:Sa crystal that is pumped with a 2 W, 532 nm CW laser. It generates ultrashort pulses with 1.5 nJ energy and a Gaussian spectral bandwidth of 50 nm FWHM which are released with a repetition rate of 75 MHz. The stretcher of the ZEUS laser is designed in a so-called Öffner design [99], a multipass, single grating configuration that allows for aberration-free stretching of the pulse to several hundreds of picoseconds. A Pockels cell is used to reduce the repetition rate of the laser pulses to 10 Hz. Once the pulse has passed the stretcher, it is guided into the first amplifier stage, consisting of a Regen amplifier and a multipass amplifier. Both amplifier crystals are pumped by the same Nd:YAG laser, delivering 110 mJ at 532 nm in 6 ns - long pulses (FWHM) at a repetition rate of 10 Hz. 10 mJ are used for the Regen while the rest is used for the multipass crystal. In the Regen, timed switching of polarization via a Pockels cell traps the laser pulse in a z-shaped cavity. After the amplification reaches saturation, the polarization of the pulse is switched back by a second Pockels cell and the pulse is coupled out of the amplifier. A third Pockels cell is used to suppress pre-cessing light that was generated during the amplification. In the multipass amplifier, the pulse energy increases from 190 μJ up to 26 mJ by passing the crystal five times. Entering the next amplification stage the pulse is split with a ratio of 50/50 by a combination of waveplates and polarizers. One part is first increased in diameter from 3 mm to 10 mm by a telescope and then amplified in a second multipass amplifier up to 250 mJ. After amplification, the beam size is increased again to the final diameter of 40 mm and the pulse is then guided towards the high-energy compressor. The other part of the pulse bypasses the multipass and directly enters a motorized delay stage. The additional delay is necessary in order to compensate for the shorter path length and to allow control for the temporal overlap of both pulses later in the experiment. Its beam diameter is increased to 15 mm and guided towards the low-energy compressor. Both compressors have the same double-grating layout, differing only in the size of the optical components. Here, the dispersion introduced by the stretcher is compensated again, resulting in a temporal compression of both pulses down to 65 fs FWHM duration. One third of the pulse energy is lost during the compression, resulting in final energies of 150 mJ for the high-energy (HE) pulse and 5 mJ for the low-energy (LE) pulse. In contrast to many other high-power laser systems, compression and subsequent guiding towards the experimental setup can be done in air as the relatively low intensity of both pulses due to their rather large beam diameter does not trigger sizeable non-linear effects in air.

3.2 Pump-Probe Setup of Levitating Spheres

The main goal of the experimental campaign was to investigate the temporal behavior of an expanding spherical plasma that is generated by focusing a high-power laser onto a levitating, micron-sized sphere. In this context, the HE pulse serves as the pump, as it ignites the plasma which is then studied by the LE pulse, that acts as the probe. The arrival time of the probe pulse with respect to the pump can be controlled by the motorized delay stage mentioned earlier in the laser section, allowing for investigation of the expanding plasma at different time steps. The delay between pump and probe can be adjusted over a time period of 1 ns. The experiment was conducted in a vacuum chamber and the main components are sketched in figure 3.5. Both the pump and probe pulse were guided towards the chamber via individual sets of two mirrors each in order to adjust their direction when coupling into the chamber. Both beam paths were equipped with two alignment irises in order to provide reproducible beam guiding into the chamber for each day of the experiment. The pulses enter the experimental chamber at a height of 200 mm via fused silica windows. The windows have an anti-reflection coating to reduce light being back-reflected into the laser. The pump is directly focused by a gold coated, 90 degree off-axis parabolic mirror with a focal length of 152.6 mm. The geometrical position of the focus defines the target chamber center (TCC), which is the designated interaction point in the experiment. A compact vacuum-compatible microscope can be used to characterize the size and position of the focal spot of the pump and assure overlap between focus and microsphere. The microscope consists of a 20x objective, two lenses and two CMOS cameras, providing simultaneous images of the focal plane with a magnification of 3 and 20, respectively.

During the experiment, the pump is focused onto polystyrene spheres with a diameter of 1 μm. These spheres are positioned via a electro-dynamic ion trap, also called Paul trap [55]. This device uses a combination of dynamic and static electric fields to confine charged particles. The polystyrene spheres are provided by a reservoir which is located above the trap. As the spheres are naturally neutral, they need to be charged for the trapping process. This is achieved by an ion gun from which the

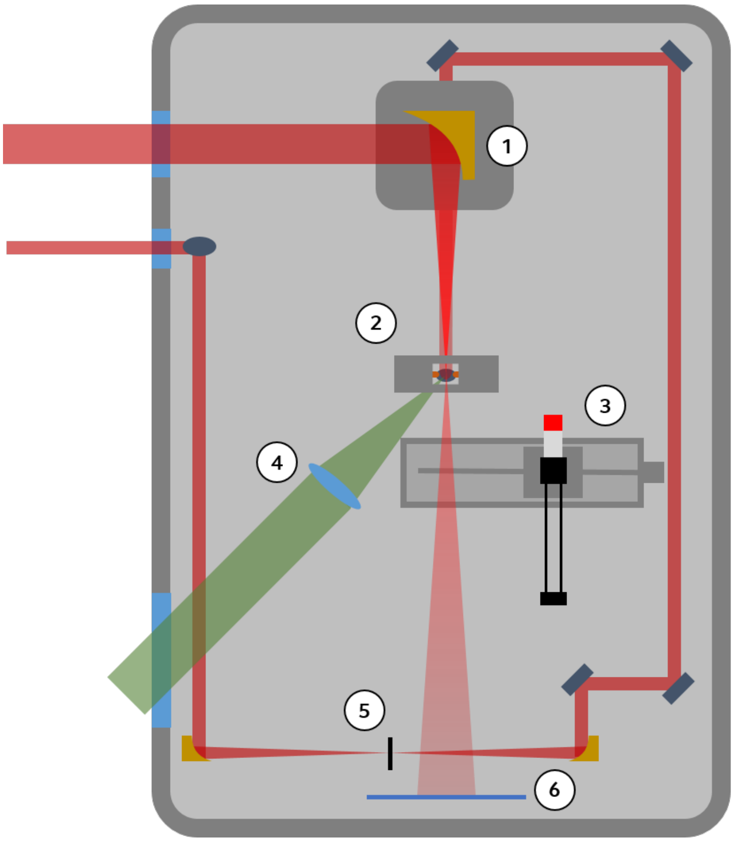

Figure 3.5: This sketch illustrates the experimental pump-probe setup at the ZEUS laser. The high energy (HE) pulse is focused by an off-axis parabolic mirror (1) with a focal length of 152 mm. The target is a micron-sized sphere which is positioned by a Paul trap (2). A motorized vacuum microscope (3) is used to determine the focus size of the high energy pulse and the position of the sphere prior to each shot. Optical measurement of the sphere position (4) is used for feedback and active damping. The low energy (LE) pulse is sent through a spatial filter, consisting of two off-axis parabolic mirrors and a pinhole, to improve the beam quality. It is then guided below the Paul trap from where it is sent upwards and focused towards the center of the Paultrap. A scatter screen (6) is used to monitor the beam profile of the HE pulse. Diagnostics of the LE pulse above the Paul trap are not shown in this sketch for the sake of clarity.

particle collects surface charges while falling into the trap. Four AC electrodes produce a rotating saddle potential that is superimposed by a constant DC endcap potential so that particle movement can be confined to a few micrometer in all three dimensions. To achieve maximum damping, the particles are illuminated with a 660 nm diode laser and the stray light is used to image the particle onto a position sensitive device (PSD) outside of the vacuum chamber. The signal from the PSD is fed back for active particle damping [55].

After entering the chamber, the probe is sent through a periscope to reduce the beam height to 50 mm. This periscope also flips the polarization of the probe pulse with respect to the pump. The probe is then guided towards a spatial filter, consisting of two 1 inch, 90 degree off-axis parabolic mirrors with focal lengths of 150 mm and a 50 micrometer high-power pinhole which is placed on a xyz-stage. The main purpose of the spatial filter is to smoothen the spatial beam profile of the probe by cutting out high-frequency distortions. This process also changes the spatial distribution from (modulated) flat-top to Gaussian. The alignment through the filter is monitored by a motorized beam block that is covered with a lens tissue and acts as a scatter screen. By observing this screen with a camera, alignment through the spatial filter can be optimized by adjusting both coupling mirrors outside of the vacuum chamber. The probe is then guided towards an elliptical mirror below the Paul trap that sends it upwards. On the way up, the probe is focused by a achromatic lens with a focal length of 60 mm. The focus of the probe is located approximately 1 mm below the polystyrene spheres.

3.3 Diagnostics

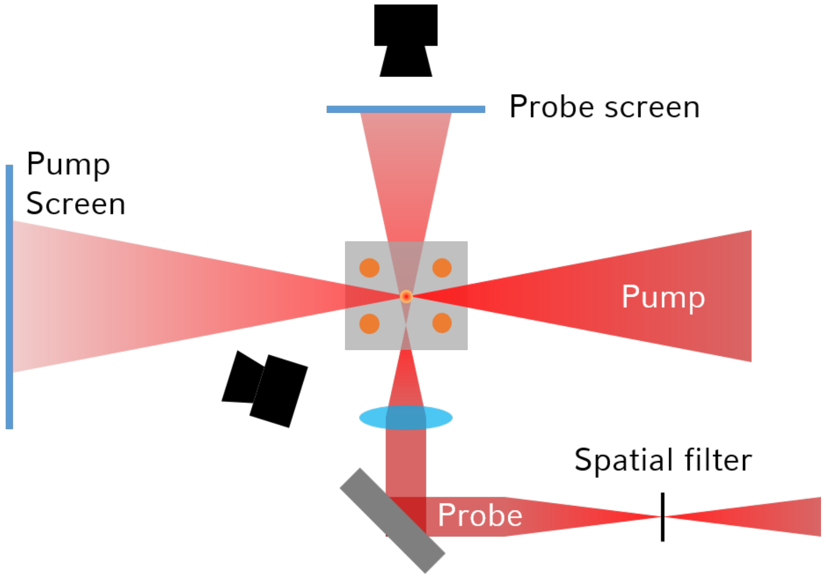

Figure 3.6: Sideview of the two main experimental diagnostics for the pump and the probe pulse: The transmitted light of the pump is collected on a scatter screen which is observed by a camera. The same is done for the probe, but in this case the camera is observing the backside of the scatter screen.

The main diagnostics of the experimental campaign are transmission profiles of the pump and probe pulse which were measured by a combination of scatter screens and CMOS cameras as illustrated in figure 3.6. Those diagnostics will be described in detail in this section. Moreover, relevant properties of the laser, such as pulse length, energy and pointing are either monitored for every shot or measured before the experiment.

3.3.1 Pump

One of the most challenging tasks when focusing a high-power laser onto a micron-sized sphere is to achieve overlap between the two. Both at the beginning as well as randomly throughout the experiment the position of the pump focus is observed via the vacuum microscope and adjusted such that it is located at TCC. The same procedure is applied for each sphere, positioning them in TCC by adjusting either the trapping position in the Paul trap or the complete trap. Although the confinement of the sphere motion is in the micrometer range, there is still residual motion of the target with respect to TCC. Depending on the position of the sphere in the Gaussian-like spatial distribution of the pump focus, the intensity with which the sphere is irradiated changes from shot to shot. This can in turn alter the expansion behaviour and it is therefore essential to monitor potential displacements. Monitoring can be achieved by investigating the transmitted light of the pump laser after the interaction with the sphere. For this purpose, a piece of sandblasted glass with dimension 200 mm x 250 mm was placed downstream of the interaction point at a distance of 490 mm. A 1.3 megapixel CMOS camera from IDS in combination with a 1/1.8" objective is used to record the transmitted laser light on the screen (see figure 3.6). In order to prevent saturation of the image, a neutral density filter was placed in front of the objective. For each target, a transmission image was recorded for four scenarios: (1) probe only with target, (2) pump and probe with target, (3) pump and probe without target and (4) a dark image with both lasers blocked. Figure 3.7 shows two exemplary images of the transmission, with scenario (3) visible in a) and scenario (2) in b). The bright spots on the transmission image with target is stray light which is created when part of the pump pulse is scattered from Paul trap elements.

During the experimental campaign, these images were mainly used to get a crude estimate of the overlap that was achieved for each shot by comparing the transmission for shots with target and subsequent shots without target (also called empty shots). When the brightness and shape did not change between both images, it was assumed that the target was missed by the pump (missing can here be understood in the way of most part of the pump intensity passing the target without any interaction). In contrast, when overlap was achieved, the brightness of the transmission profile in the

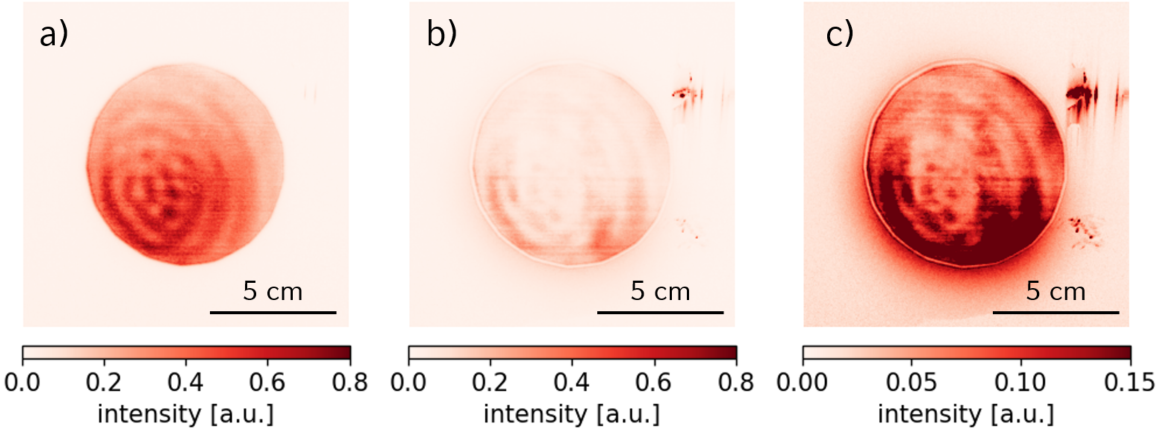

Figure 3.7: Exemplary transmission profiles of the pump laser: a) without target and b) with target. c) shows the same profile as b) but was subsequently oversaturated for better visibility of the corona surrounding the otherwise sharp beam profile boundary and originates from laser-plasma interaction.

target case was severly reduced (by up to 65 %). Moreover it was discovered that additional light appears outside the pump beam profile boundary that is imprinted by an aperture. In most cases, this corona was not symmetric but more emphasized on one side as can be seen in figure 3.7 c). This was assumed to originate from partial overlap between pump focus and target and utilized to re-adjust the position of the target in the next shot. This procedure increases the hit probability during experiment substantially.

3.3.2 Probe

Following the interaction with the pump pulse, the created spherical plasma will expand into the vacuum. In order to study the temporal behaviour of this process, the probe was used to observe the plasma conditions for each shot. By changing the delay between pump and probe, those observations provide a time-resolved study of the dynamic changes. The measurement of the plasma is based on the concept of inline holography [48] and set-up as follows: After being guided below the Paul trap, the probe is sent upwards and focused shortly in front of the levitating sphere with an estimated distance of 1 mm between focus and TCC. After passing the target, the light from the probe is collected on a piece of sandblasted glass (50 mm x 50 mm) which is positioned 103 mm above TCC. The backside of this screen is imaged by a 1.3 megapixel camera from IDS with a 1/1.8" objective. Figure 3.6 shows a sketch of the probe concept.

The observation of the plasma expansion can be divided into three different scenarios, illustrated in figure 3.8: the first scenario is negative delay between pump and probe, that is the probe passes the sphere prior to the pump. This case is used to determine whether the plasma is ionized prior to the pump arrival by pre-ceeding light and if so, at what time the onset happens. As we will see later, this approach works because the probe profile of a transparent sphere and a sphere in which the free electron density exceeds the critical density differ dramatically (see e.g. figure 3.9). The second scenario is zero delay, where pump and probe arrive at the same time, determining the state of the target at the time of main pulse interaction. In the last scenario, the probe has positive delay, i.e. it observes the target after the interaction. This stage provides information about the subsequent expansion dynamics of the sphere.

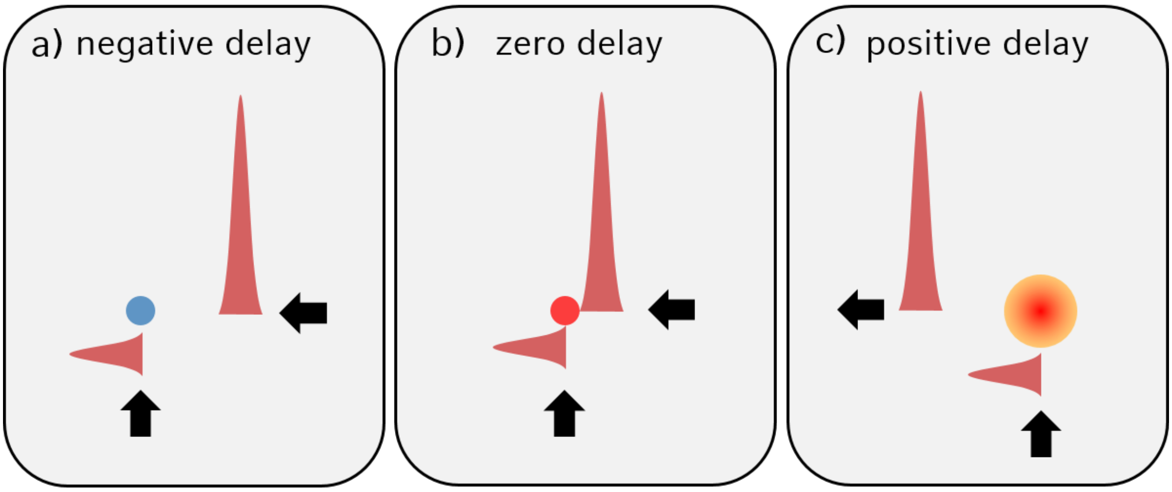

Figure 3.8: The three main probing scenarios are shown: a) negative delay (probe arrives before pump, b) zero delay and c) positive delay (probe arrives after pump).

The main observable in this probing setups are diffraction patterns that are visible on the scatter screen. As the target is placed behind the probe focus, the target is smaller than the area illuminated by the probe in the TCC plane. Light diffracted by the target will interfere with light passing the target and result in a ring pattern (inline-holographic image) that is observed on the scatter screen. Changes of the target will alter this diffraction pattern accordingly and allow to determine the extend of expansion by evaluating the recorded patterns. As the imprinted patterns are often very weak and hardly visible, an image without target is subtracted from the diffraction patterns to enhance visibility of the interference pattern. The basic justification is that the inline-holographic image I_{ihi} is given by the superposition of the signal field E_s and a reference field E_r. Hence, $I_{ihi} = E_r^2 + E_s^2 + 2E_rE_s$, where the cross term E_rE_s contains the required information on the plasma. For each shot, images are recorded for the same four cases as for the transmission: the first is probe only with the undisturbed target, which was used to judge on target quality, for example to differentiate between single targets and clusters. The second case is pump and probe with target where the expansion can be examined while the third one is pump and probe without target, providing the reference intensity distribution. The last image is again a dark image with pump and probe blocked. Figure 3.9 shows exemplary data that was recorded during the experiment: a) and b) are raw images of the probe scatter screen for the case of probe only and pump-probe with target (delay +193 ps), respectively. Pictures c) and d) show the same images after the reference image is subtracted. The visibility of the diffraction pattern is clearly increased.

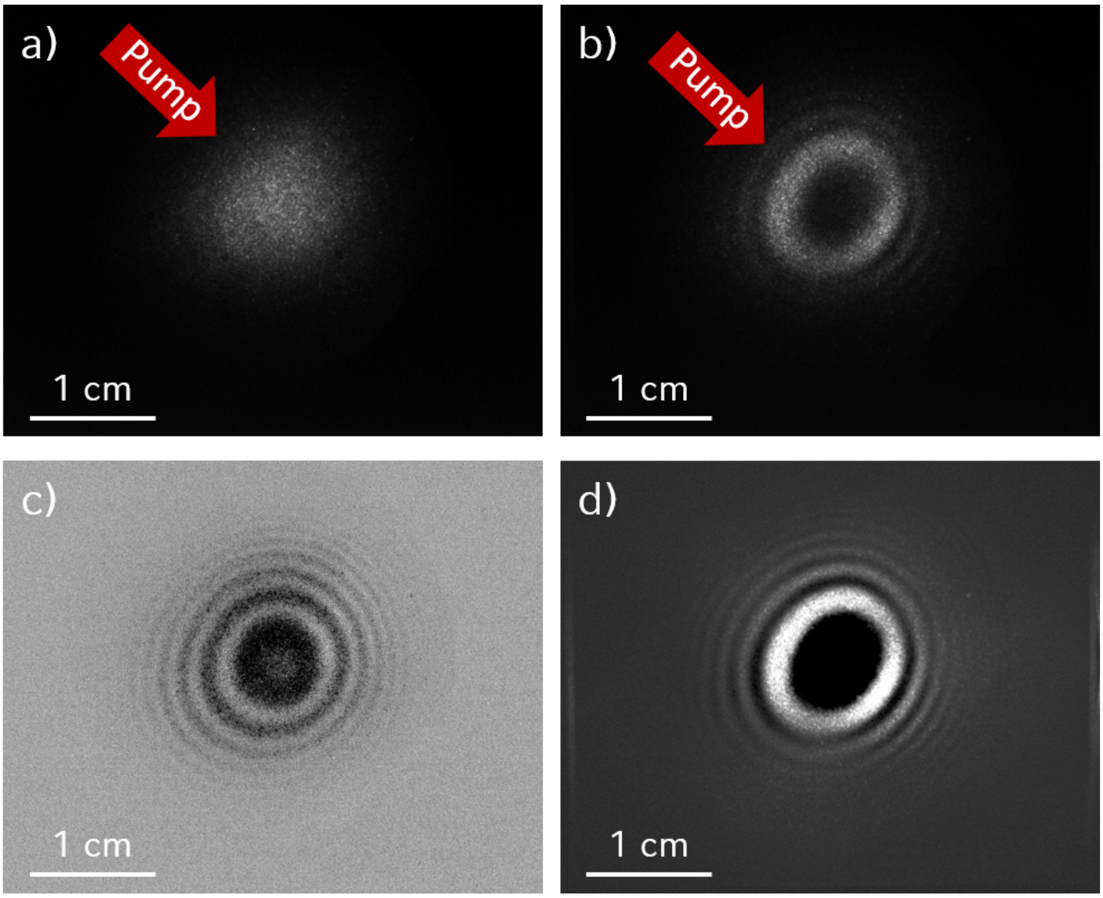

Figure 3.9: Exemplary images recorded on the probe screen: a) shows the diffraction pattern of an undisturbed sphere (pump blocked) while b) depicts the pattern of the same target 193 ps after interaction with the pump pulse. c) and d) show the interference term E_rE_s after subtracting the reference image from a) and b).

Constraints on the probe pulse The purpose of the probe pulse is to solely investigate the state of the sphere at a certain time. It is therefore essential to prevent any interaction between target and probe that influences the expansion dynamics of the sphere. For this reason the energy of the probe pulse was reduced prior to the LE compressor by inserting two neutral density filters with a combined value of 4.5, yielding an estimated final probe energy of $\sim 5\ \mu$J in the vacuum chamber. This energy also proved to be a safe value for the high-power pinhole of the spatial filter, where plasma ignition at the edges was visible for higher energies. Although the energy was drastically reduced, particles were repeatedly ejected from the Paul trap or started to strongly oscillate. These additional problems were identified while taking data with probe only shots and might have been caused by the probe removing surface charges from the particle and by that affecting the trapping process. Further reduction of the probe energy was not feasible in order to maintain an acceptable signal level on the probe images. It was therefore decided to reduce the probe intensity by increasing the pulse length. The grating distance of the LE compressor was changed until probe only shots did not disturb the target motion any longer. Measuring the additional displacement of the compressor gratings to $\sim$ 10 mm yielded a pulse duration of $\Delta\tau = \Delta\tau_{in} \cdot \sqrt{1 + \left(4 \cdot ln2 \cdot D_2 / \left(\Delta\tau_{in}\right)^2\right)^2} \sim 2.6$ ps, using $\Delta\tau_{in} = 65$ fs and a group delay dispersion $D_2 = 61900\ fs^2$. This probe pulse duration is much longer than the minimally possible 65 fs, but is acceptable with respect to the duration of expansion over 600 ps targeted in this study.

Reducing self-emission and stray light While probe only shots yielded stable and well observable diffraction patterns, the background on the probe scatter screen with the pump pulse incident increased significantly. Those features overlap with the probe pulse and can render recording diffraction images impossible, due to the image being either over-satured (see figure 3.10 a)) or the high noise level when adding filters to the probe camera. The main sources of this cross-beam background are most likely scattering of the pump pulse by the plasma and light emitted from the expanding plasma itself, potentially delayed and over a long period. In order to reduce the disturbance, a two inch polarizer with a extinction ratio of $10^5 : 1$ was placed above the scatter screen and rotated such that the transmission was maximized for the probe pulse. Stray light from the pump that does not match this polarization is attenuated by the polarizer. The polarization of the probe was rotated at 90 degrees with respect to the pump by the periscope at the entrance of the vacuum chamber such that pump and probe have perpendicular polarization at TCC, potentially enhancing the contrast between probe and pump pulse. In order to reduce the light emitted by the plasma, a spectral edge-pass filter with a cut-on wavelength of 750 nm was placed in front of the camera. Previous studies have shown that a large amount of the emitted light is located in the wavelength-region of 2ω (400 nm in this case) which is strongly reduced by the filter. The final setup is shown in figure 3.10 b). Although both measures helped to reduce noise in the probe images, the pump energy remained limited to below 1 mJ in order to record probe images with an acceptable signal-to-noise ratio. The pump energy was hence reduced by not pumping the second multipass amplifier, yielding between 600 and 650 μJ.

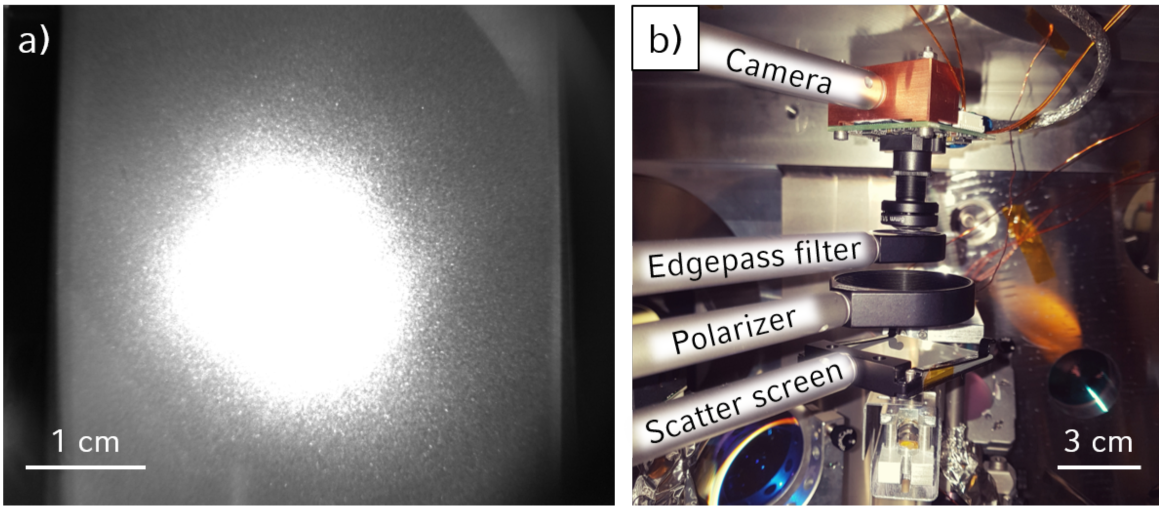

Figure 3.10: a) shows an oversaturated image of the probe screen when using high pump energy. Measures taken to attenuate stray light and self-emission can be seen in b).

Probe image post-processing The measures described above significantly reduced the influence of stray light on the recorded probe images. In order to make the existing diffraction rings even more clearly visible, additional filters were subsequently used in the processing of the results. First, high-frequency noise was reduced with the aid of an averaging filter. For this purpose, a uniform filter was applied to the raw images in Python, which replaces the value of each pixel by the average value of an area centered around the pixel. The size of this area can be set separately for each data set. Thereby, a balance between smoothing of high frequency noise and preservation of fine diffraction structures at the edge of the image was chosen. Furthermore, a visible offset of the diffraction pattern towards positive values is evident in the raw data. This is probably due to stray light from the particle which was not completely suppressed by the measures described above. In order to determine the shape of this component, measurements were carried out in which only the pump was focused on the particle and the resulting scattered light was recorded on the probe screen. The probe pulse was blocked at the entrance of the experimental chamber. It was found that in the most general case the distribution can be approximated by an elliptical 2D Gaussian distribution, where the major axis can be tilted.

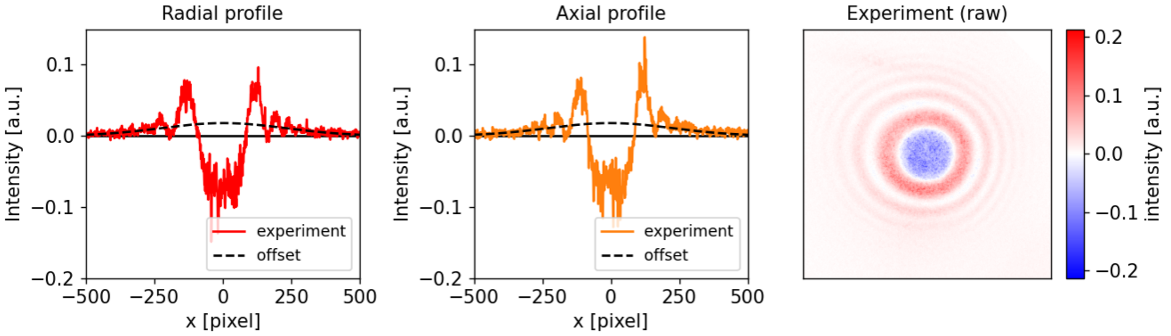

Figure 3.11: Raw image of experimental diffraction pattern with corresponding radial (red line) and axial (orange line) profiles. The black dashed line indicates an Gaussian-like offset of the diffraction pattern that is caused by background contributed through pump-plasma interaction.

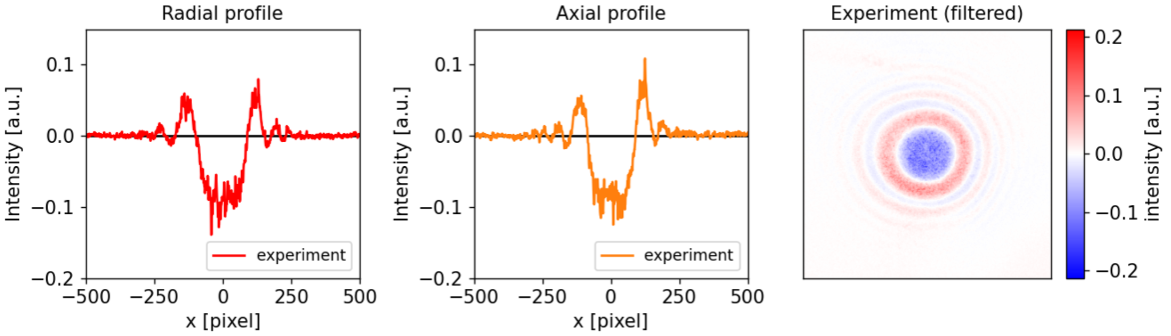

Figure 3.12: Filtered image of experimental diffraction pattern with corresponding radial (red line) and axial (orange line) profiles.

Therefore, a Gaussian distribution was empirically determined for each individual data set to minimize the offset as best as possible. This distribution is then subtracted from the raw image. In figure 3.11, the described offset is clearly visible in both the radial and axial profile of the raw image. The profiles of the subtracted Gaussian distribution are indicated as black dashed lines. The final result after applying all filters is shown in figure 3.12. Only a weak uniform filter with a size of 3x3 pixels was used to preserve diffraction structures at the edge. By successful removal of the offsets all diffraction structures are arranged along the zero line which facilitates a later comparison with simulations.

Zero timing In the framework of this experiment, the zero time (or t_0) is defined as the moment in time when the pump pulse reaches its maximum intensity at TCC. For determining the expansion of the target as a function of time, precise knowledge of the temporal relation of the probe pulse and t_0 is essential. This relation was determined by the aid of an air plasma in the residual gas of the experimental chamber. The onset time of plasma generation can be measured by the probe by changing the position of the delay stage until the plasma-caused disturbance in the probe profile becomes visible on the scatter screen. The pulse energy of the pump was attenuated, such that the disturbance was only visible in a very narrow time window. The onset time then marks the peak of the pulse. As pump and probe have different path lengths inside the vacuum chamber, the onset time (and thus t_0) measured with residual gas differs from the vacuum value due to the different speed of light. Therefore, the pressure is gradually decreased and the onset time is measured for each pressure. By interpolating the onset time for zero pressure, the correct vacuum value of t_0 is determined. The error of this method is approximated to be $\pm 0.5\,ps$.

3.3.3 Laser Characterization

Energy, pulse duration and spectrum The pulse duration is measured prior to the experiment for each pulse after the compressor using the FROG 8-9-USB device from Swamp Optics. The dispersion by the glass windows when entering the vacuum chamber was pre-compensated by putting duplicate windows in front of the FROG. Optimized compression yielded values of 60-65 fs (FWHM) for both pump and probe pulses. The manual chirping of the probe pulse was not measurable by the FROG but was calculated by applying the additional compressor dispersion to the 65 fs duration as described earlier. The pulse spectrum was continuously monitored with a spectrometer (EPP2000C-25, StellarNet) in the stretcher by coupling the zero order beam of the grating into an optical fiber connected to the spectrometer. The pulse energy was measured after each amplifier and additionally before the vacuum entrance windows. The pump pulse contained on average $600 \pm 10 \mu$J after compression while the strongly attenuated probe pulse was too weak for measurements after the compressor. However, by measuring the probe pulse energy without filtering (5 mJ after compression) and by accounting for the attenuation of the neutral density filters ($\sim 10^3$), the energy can be estimated to $\sim 5\mu J$.

Laser stability: pointing and energy Achieving overlap of the pump focus and the target is already a challenging task due to the residual motion of the trapped sphere. Additional complexity arises if the laser adds to fluctuations. Laser motion can be differentiated into long-term drifts and short-term jitter. While the jitter is more of a stochastic process, drifts have typically a correlation to more obvious parameters. At the ZEUS laser, the high-frequency laser jitter causes a variation of the laser position in the focal plane of $\pm 0.3\,\mu m$ and is much smaller than the residual target motion of $\pm 3\,\mu m$. Slow drifts however caused a long-term change of propagation direction over the complete laser. This led for example to a substantial change of focus position for the pump, misalignment in the spatial filter for the probe and reduced energy for both. The cause for this drift is not fully understood yet but most likely due to temperature changes in the lab. The drift becomes non-negligible after two to three hours and must be compensated by realigning the laser. For this purpose, the position of the beam is monitored by a set of cameras at certain points via leakage through the laser mirrors or by flipping alignment marks into the beam path. Motorized mirrors then allow for remote re-alignment of the laser back to the correct position [100]. Instability of the laser energy is correlated mainly to the described drift. On the other hand, shot-to-shot fluctuations are due to unstable pump lasers or initial misalignment of the amplifiers. These fluctuations are measured over a period of 500 pulses after each amplifier during the first laser alignment by an energy meter and amplifiers are optimized until a stability of less than 3% RMS is obtained. Subsequent measurements have shown that this value is constant as long as the propagation of the laser is correct.

Spatial distribution of pump in the focal plane The spatial distribution of the pump pulse in the focal plane was determined with the vacuum microscope and attenuated pulses. Three images of the spatial distribution were taken with varying filter settings and combined in the analysis to provide a final image with a dynamic range of three orders of magnitude. The final result normalized to the peak is analysed in figure 3.13. With an evaluated FWHM of 5.9 μm and an assumed pulse energy of 600 μJ contained in a pulse duration of 65 fs (FWHM), this yields a peak intensity of $1.6 \cdot 10^{16}\, W/cm^2$ and a normalized laser vector potential a_0 of about 0.1.

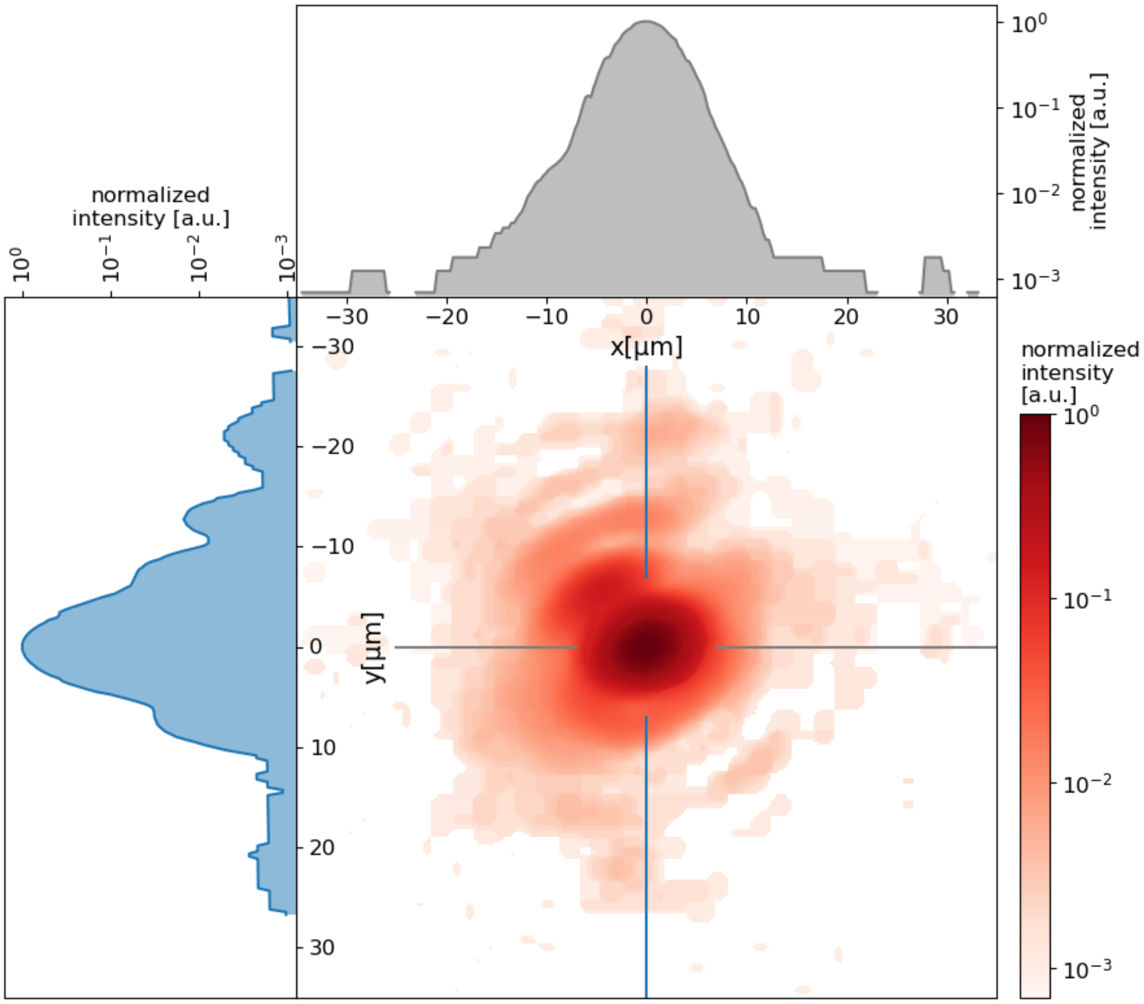

Figure 3.13: Normalized spatial intensity distribution of the pump pulse in the focal plane. Intensity profiles at x=0 μm and y=0 μm are shown in blue and grey, respectively.

Temporal intensity distribution While the peak intensity of a fs-laser pulse is by its virtue confined to some 10s or 100s of femtoseconds, the total pulse energy can be distributed over many nanoseconds. Depending on the exact temporal intensity distribution, such pre-ceeding (or trailing) light can significantly influence the laser-plasma interaction even when its intensity is relatively low. The causes for such badly timed pump light are manifold: Amplified Spontaneous Emission (ASE), originating from the Ti:Sa crystals during amplification, creates a light-background on the nano- to picosecond level. Reflections in transmittive optics can create short, distinct post-pulses and convert via non-linearities in the amplifier medium to pre-pulses [101]. Due to the high intensities achieved in the laser focus, those can easily reach the ionization threshold of the target ($10^{12} - 10^{13}\,W/cm^2$) and influence the laser-target interaction. It is therefore critical to measure the temporal intensity distribution of the laser with high dynamic range over a long time interval around the fs pulse. At the ZEUS laser, this was done by a third-order-auto-correlator (Tundra, UltraFast Innovations, 10^{12} dynamic range) with a scan range of two nanoseconds (from -1.8 ns to +0.2 ns around the fs pulse). The measured autocorrelation trace is plotted in figure 3.14: the left ordinate shows the intensity distribution normalized to the maximum of 1 as obtained by the auto-correlator, while the right ordinate was scaled to the previously calculated intensity of $1.6 \cdot 10^{16}\,W/cm^2$. The red bar marks the intensity range at which severe plasma generation of polystyrene is expected. As can be seen, only the main pulse surpasses this range, indicating that no premature plasma generation is expected.

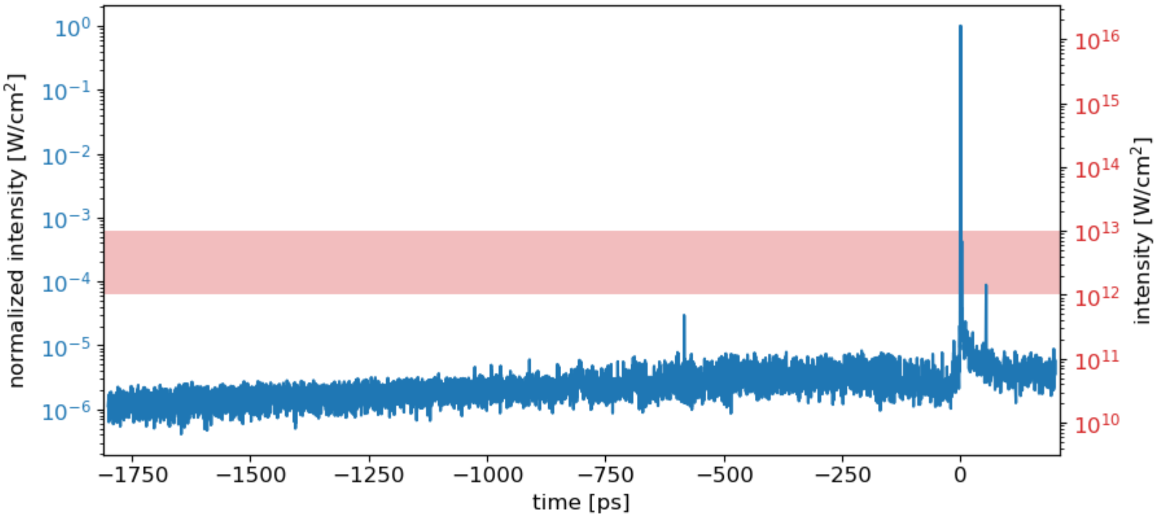

Figure 3.14: Autocorrelation trace: the left axis shows the normalized signal while the right axis is scaled to the peak intensity $1.6 \cdot 10^{16}\,W/cm^2$ (this experiment). The red bar indicates the area of assumed plasma generation threshold ($10^{12} - 10^{13}\,W/cm^2$).

Chapter 4

Simulations

Contents

4.1 Simulation Setup 56

4.1.1 Setup of Pump Simulation 57

4.1.2 Setup of Probe Simulation 61

4.1.3 Implementation of Density Distribution 64

4.2 Density Models 69

4.2.1 Initial Sphere and Particle Number 70

4.2.2 Exponential Distribution 71

4.2.3 Single Gaussian Distribution 75

4.2.4 Dual Gaussian Distribution 79

4.3 RALEF Simulations 86

4.4 Methodology 90

This chapter describes the numerical calculations for generating artificial, i.e. simulated diffraction patterns of various plasma density models. Starting with the simulation setup, three models for the spherical plasma in order of growing complexity are introduced. The most suitable model is compared with hydrodynamic simulations. Finally, the methodology is presented of how plasma parameters can be extracted when comparing experimentally recorded and numerically calculated diffraction patterns.

4.1 Simulation Setup

In order to make statements about the state of the plasma at different times, diffraction patterns of simple 3D density distributions are created with the help of numerical calculations. These can later be compared to experimental data. For this purpose, the Python package LightPipes is used. This beam propagation toolbox uses scalar diffraction theory and allows to simulate propagation of coherent light through optical elements. LightPipes was chosen because it allows to create self-defined objects with non-uniform refractive indices as well as to calculate the associated diffraction effects while the source code is accessible. Light is treated in LightPipes as a square, two-dimensional array of complex amplitudes and its propagation can be modeled by four different functions: an FFT approach using the spectral method (see equation 2.74), FFT computation of a convolution of the Fresnel-Kirchhoff diffraction integral (see equation 2.77), direct calculation of the Fresnel-Kirchhoff diffraction integral and a propagation method for non-uniform media (see equation 2.82). More details on the implementation of these propagators and the complete package can be found in [102].

Limitations of LightPipes As all numerical simulations, LightPipes is subject to some limitations which are described below:
Since the code computes on a discrete grid and the computation time increases rapidly with increasing number of grid points, there is a certain limit to the accessible resolution. For all simulations a compromise between physically reasonable resolution and acceptable computing time has to be found.
The temporal evolution of a light pulse is not taken into account and therefore changes of diffracting objects during propagation cannot be considered. In addition, Lightpipes requires the specification of a single wavelength and is thus unable to calculate diffraction effects over the entire broadband spectrum of an ultrashort laser pulse. Since the pulse lengths are short compared to the expected temporal changes of the plasma and the real bandwidth of the pulse is comparatively narrow at 15 nm FWHM, these limitations are considered acceptable.
Physical properties such as energy or intensity of the light are also not taken into account and effects such as ionization and absorption are not considered. Similarly, contributions to the diffraction patterns in the form of e.g. self-emission from the plasma itself are not modelled. These limitations can also be neglected in view of the plasma states assumed to be quasi-stationary during the pulse length and the measures taken in the experiment to reduce such contributions.

Finally it has to be noted that reflections occuring for example in the interaction of laser light with an overcritical plasma cannot be investigated because fields in LightPipes are calculated only in one (main) direction and an analysis of potential reflections is therefore not possible.

LightPipes allows the simulation of optical components to reproduce the experiment setting as described in section 3.3.1 for the pump and section 3.3.2 for the probe. Distances and beam sizes are taken from experimentally determined values and parameters such as focus size and beam size on the screen are compared with experimental results to ensure the best possible match with the real situation. The implementation of the density profile is based on simple analytical functions. Here, the 3D distribution along the propagation axis is divided into a set of successive 2D arrays through which the field propagates. A detailed description will be given later in the relevant section 4.1.3.

4.1.1 Setup of Pump Simulation

Figure 4.1 shows a schematic of the simulation setup for the pump pulse. The exemplary intensity distributions are calculated from the fields in the respective positions. In the first step, a square homogeneous field with a size of 200 mm x 200 mm and a grid with 2048 x 2048 points (resolution 98 μm) is generated. This field is multiplied by a mask whose distribution represents the near field of the laser before focusing (figure 4.1(1)). The exact specifications of the applied mask are described later in more detail. The input field is then focused by simulating a lens with a focal length corresponding to the real value of the off-axis parabolic mirror of 152.6 mm. This step is stopped half a target diameter before focus such that the center of the spherical target can be placed exactly in the focal plane (figure 4.1(2)). To maintain a reasonable resolution in the focal plane, LightPipes uses a conversion to spherical coordinates for this process. Here the coordinate system is bent similar to the converging spherical wavefront and then propagated. To prevent a grid with zero size in the focal plane, a combination of a (weak) phase mask and a (strong) geometric coordinate transform is used. The focusing of the field is determined by the combination of both, resulting in the correct focal length of 152.6 mm while the bending of the coordinate system is governed by the transform, resulting in a non-zero gridsize after propagation. At the end, a back transformation to Cartesian coordinates is performed, where the rescaled grid size depends on the target diameter. In the present case, the resulting grid size varies between 311 μm x 311 μm and 317 μm x 317 μm and corresponding resolutions of 152 - 155 nm. Subsequently, the field is propagated stepwise through 2D arrays representing the selected density distribution in the form of an inhomogeneous refractive index distribution (figure 4.1(3)). The propagation is performed in Cartesian coordinates with the same grid size and resolution as in stage 2. The step size along the propagation axis has the same value as the resolution of the grid to ensure a symmetrical implementation of the density distribution.

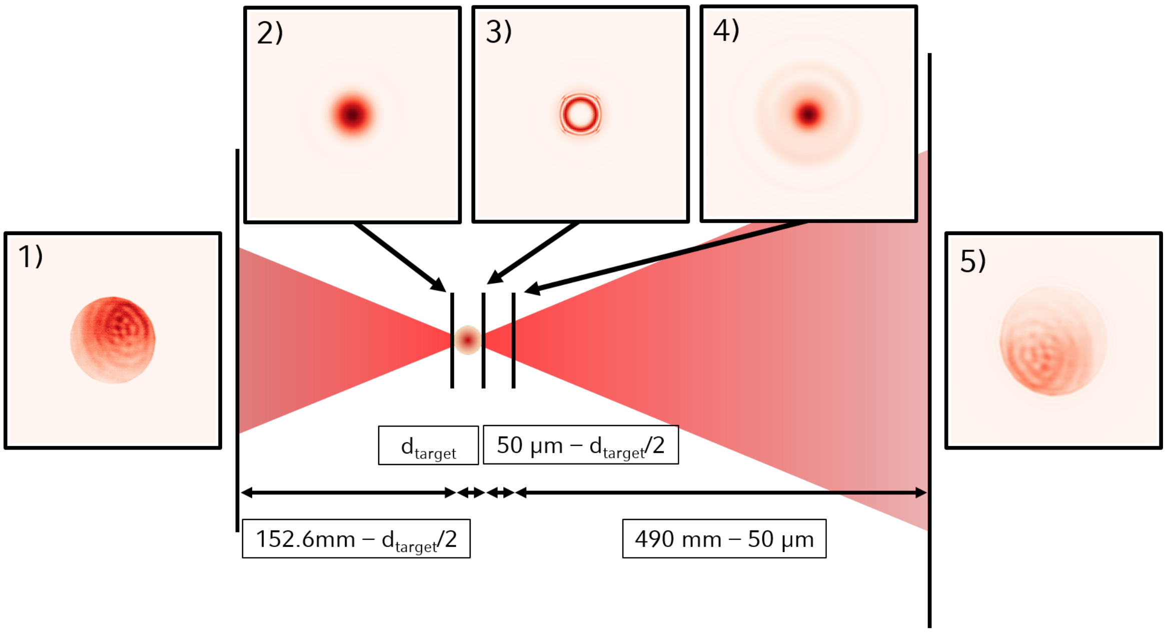

Figure 4.1: Setup of the pump simulation with cutouts of exemplary intensity distributions and corresponding values of gridsize (GS), dimension of cutout (CO) and grid resolution (RES): 1) Initialization of the field with applied mask to model input field (GS: 200 mm x 200 mm, CO: 50 mm x 50 mm, RES: 98 μm); 2) propagation towards focus (GS: 311 μm x 311 μm, CO: 40 μm x 40 μm, RES: 152 nm); 3) propagation through density distribution (GS: 311 μm x 311 μm, CO: 40 μm x 40 μm, RES: 152 nm); 4) short propagation after target (GS: 311 μm x 311 μm, CO: 40 μm x 40 μm, RES: 152 nm); 5) propagation to screen (GS: 500 mm x 500 mm, CO: 125 mm x 125 mm, RES: 245 μm). The black vertical lines are to illustrate changes in the size of the simulation grid.

After the target, the field is freely propagated 50 μm minus half a target diameter in Cartesian coordinates with the same grid parameters (figure 4.1(4)). This step helps to stabilize the simulation. For the last step (propagation towards screen), the field is again propagated in spherical coordinates, where the geometric transform is governed by the designated final grid size of 500 mm x 500 mm. In order to counter the effect of the geometric transform, an additional phase mask is applied to the field, such that its divergence after the focus is not altered by the coordinate transformation. After a propagation distance of 490 mm - 50 μm a back-transformation to Cartesian coordinates is performed. The result output can be converted to an intensity distribution, which is the simulation equivalent of the experimentally recorded transmission image which will later be used to determine the density distribution of the plasma (figure 4.1(5)). To simulate an empty shot, the same procedure is used whereby the 2D arrays of the target are provided with a homogeneous refractive index of 1 to simulate the propagation through vacuum. The decision to also propagate stepwise was made to check if the propagator delivers physically correct results and to exclude simulation related errors.

Calibration of pump setup

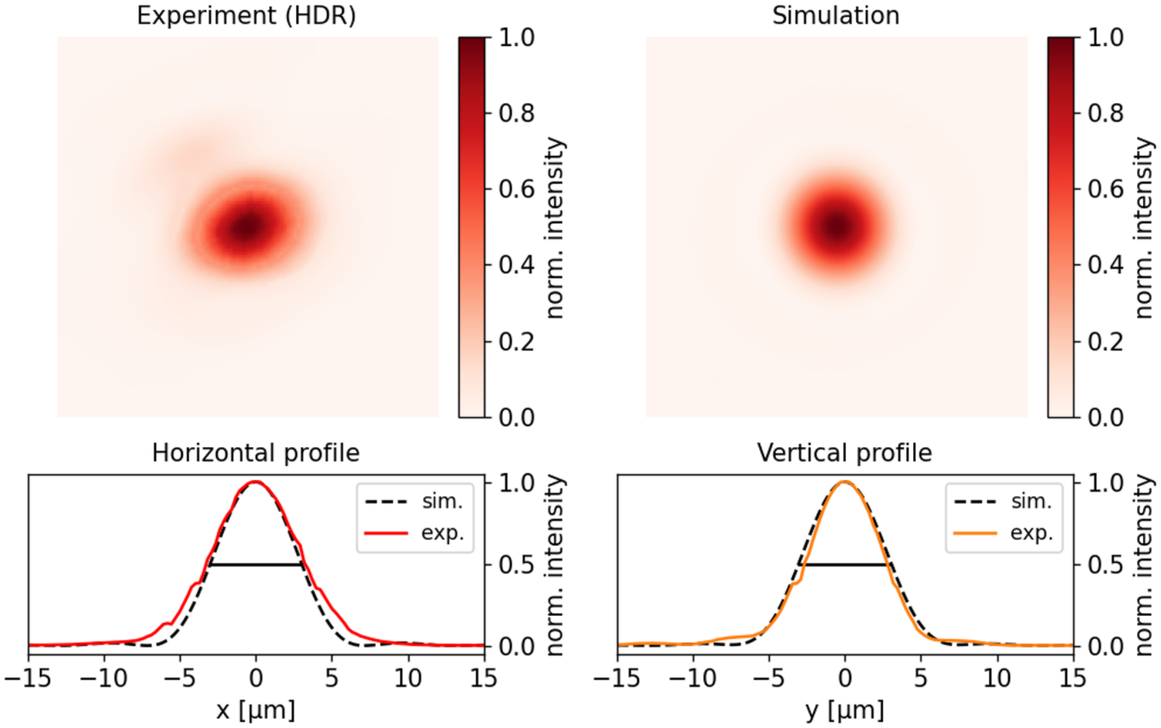

Figure 4.2: Comparison of the experimentally determined laser focus (see figure 3.13) and the final intensity distribution in the focal plane obtained from the pump simulation. The black solid line illustrates a FWHM of 6 μm.

In order to calibrate the simulation, experimental results can be used as a reference.

In the case of the pump, these results are the size of the laser in the focal plane (measured with the vacuum microscope) and the pump profile of an empty shot (recorded on the transmission screen). In order to obtain the simulation result of the focus, the propagation of step 2 is performed over the complete focal length of 152.6 mm and an intensity distribution is calculated from the field at the end of the propagation. As the field is initially implemented with a flat phase the diameter of the intensity distribution in focus is governed by the diameter of the applied mask in step 1. Using the experimentally determined beam diameter of 24 mm resulted in a focus with 5.3 μm, which is smaller than the experimentally determined FWHM of 6 μm. This deviation is likely caused by aberrations of the wavefront, which are present in the experiment and slightly increase the real focus size. These aberrations are not implemented in the simulation for simplicity. In order to obtain an equal FWHM of the focus in both experiment and simulation it was decided to reduce the diameter of the input mask to 21 mm. Figure 4.2 shows a comparison of the experimentally obtained focus image (see figure 3.13) and the final intensity distribution in the focal plane obtained from the simulation. Both agree well in terms of the FWHM.

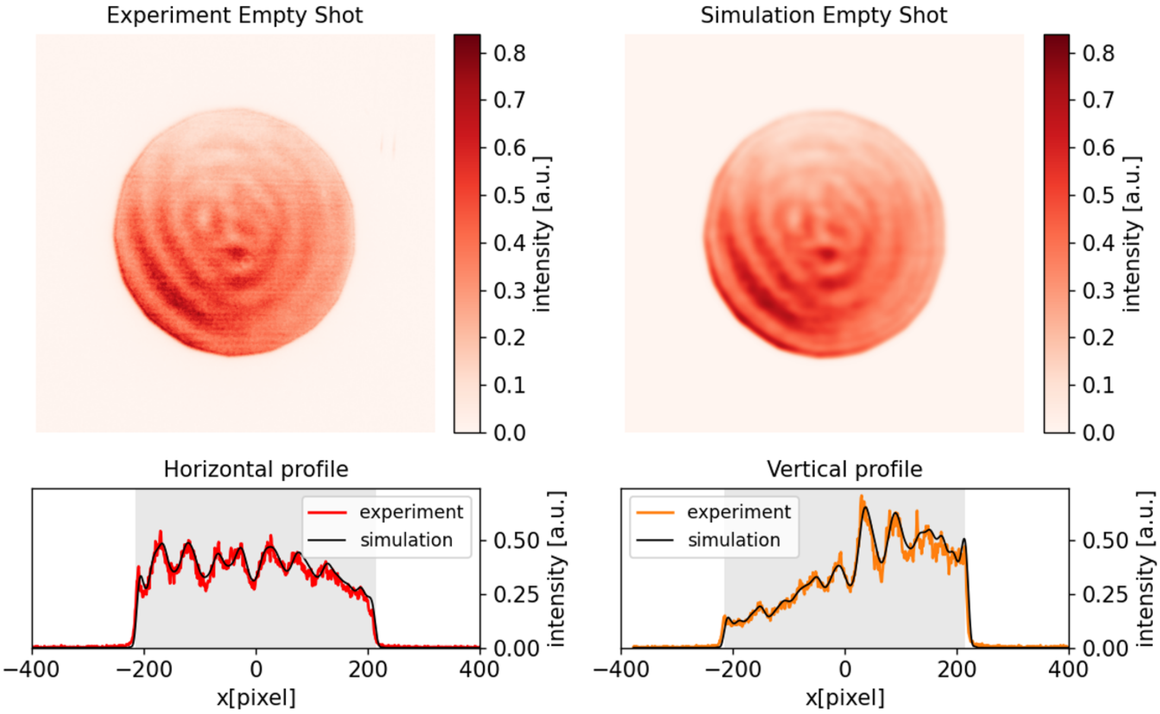

Figure 4.3: Comparison of the experimentally recorded beam profile on the pump screen (empty shot) and the final intensity distribution obtained from the pump simulation (empty shot).

The second reference for the pump simulation is the intensity profile of an empty shot without target. The experimentally recorded transmission image can be compared with the intensity distribution calculated from the final field in the simulation (step 5). To model a distinct beam profile, the input mask with a diameter of 21 mm is multiplied with a 2D distribution such that the initial intensity distribution of the simulation equals the experimentally obtained intensity distribution on the transmission screen. It is assumed that diffraction effects in free propagation through the vacuum are negligible and therefore the intensity distribution in the near field before and after focusing are almost identical. As empty shot data is available for each target, this process can be applied for all shots, hence accounting for potential fluctuations in the beam profile. Figure 4.3 shows a comparison of an exemplary transmission profile and an intensity distribution resulting from the corresponding simulation, where great agreement between both cases can be seen.

4.1.2 Setup of Probe Simulation

The structure of the probe simulation is very similar and is illustrated in figure 4.4 with cutouts of exemplary intensity distributions obtained from the respective fields. At the beginning, again a homogeneous field is created, but this time with a size of 440 mm x 440 mm and a grid of 4096 x 4096 points (resolution 107 μm). To model the beam in front of the probe lens, a mask is applied similar to the pump simulation (figure 4.4(1)). Details on the mask specifications are again given later in this subsection. This input field is then focused with a focal length of 60 mm, following the same procedure for the transformation to spherical coordinates as for the pump case. After back-transformation to Cartesian coordinates, the re-scaled grid in the focal plane has a size of 938 μm x 938 μm and a resulting resolution of 230 nm (figure 4.4(2)). Subsequently, the beam propagates freely 770 µm minus half a target diameter (figure 4.4(3)), using the same grid size and resolution. Analogous to the case of the pump, the field is propagated step-wise through 2D arrays with inhomogeneous refractive index based on the density distribution of interest (figure 4.4(4)). After the target, the field freely propagates 200 µm minus half a target diameter (figure 4.4(5)), keeping the grid size at 938 μm x 938 μm (this step again helps to stabilize the simulation). In the last step, the grid is transformed to spherical coordinates, using the same method as in step 5 of the pump simulation. After a propagation of 103 mm - 970 μm, a back-transformation to Cartesian coordinates is done, resulting in a final grid size of 42 mm x 42 mm with 102 μm resolution (figure 4.4(6)). The intensity distribution,

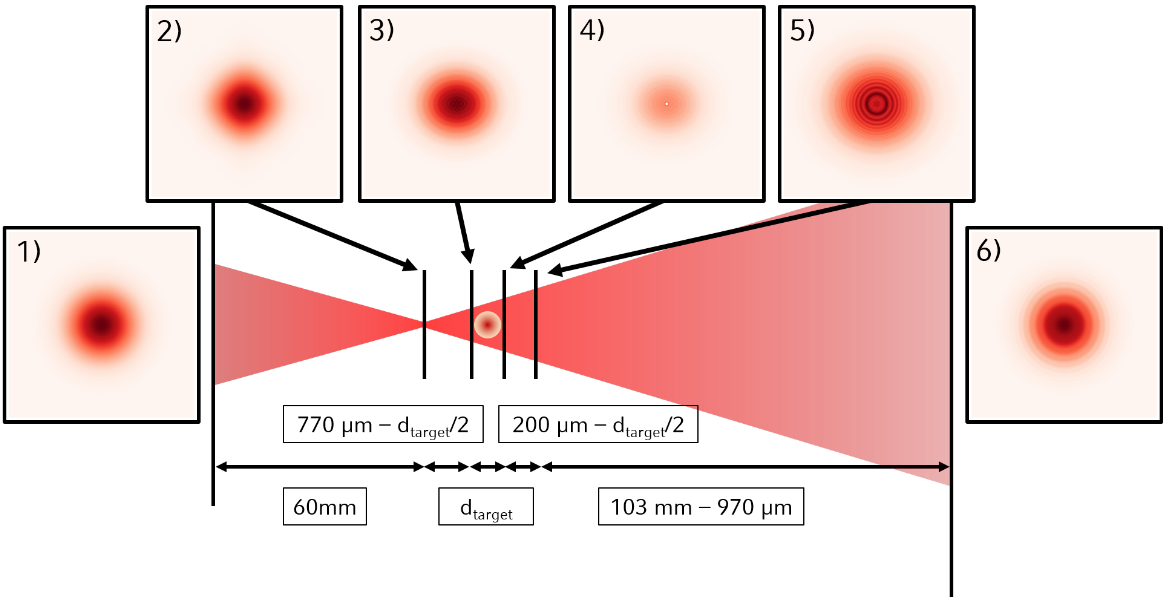

Figure 4.4: Setup of the probe simulation with cutouts of exemplary intensity distributions and corresponding values of gridsize (GS), dimension of cutout (CO) and grid resolution (RES): 1) Initialization of the field with applied mask to model input field (GS: 440 mm x 440 mm, CO: 25 mm x 25 mm, RES: 107 μm); 2) propagation towards focus (GS: 938 μm x 938 μm, CO: 30 μm x 30 μm, RES: 230 nm); 3) propagation towards target (GS: 938 μm x 938 μm, CO: 300 μm x 300 μm, RES: 230 nm); 4) propagation through density distribution (GS: 938 μm x 938 μm, CO: 300 μm x 300 μm, RES: 230 nm); 5) short propagation after target (GS: 938 μm x 938 μm, CO: 300 μm x 300 μm, RES: 230 nm); 6) propagation to screen (GS: 420 mm x 420 mm, CO: 420 mm x 420 mm, RES: 102 μm). The vertical black lines are to illustrate changes in the size of the simulation grid.

obtained from the final field is the equivalent to the experimentally recorded transmission images on the probe screen. Empty shots are calculated by implementing a homogeneous density distribution with $n_e = 1$.

Calibration of probe setup

The two references that can be used to calibrate the probe simulation are the recorded intensity distribution of an empty shot and the diffraction pattern of a non-ionized 1 μm plastic sphere obtained from a probe only shot. The empty shot is used to define the mask applied to the initial field. As the distance from the probe lens to the probe screen is fixed and can be precisely measured in the experimental setup, the mask can be adjusted such that the resulting intensity distribution of the simulation best matches the experimentally recorded distribution on the probe screen. Since the probe

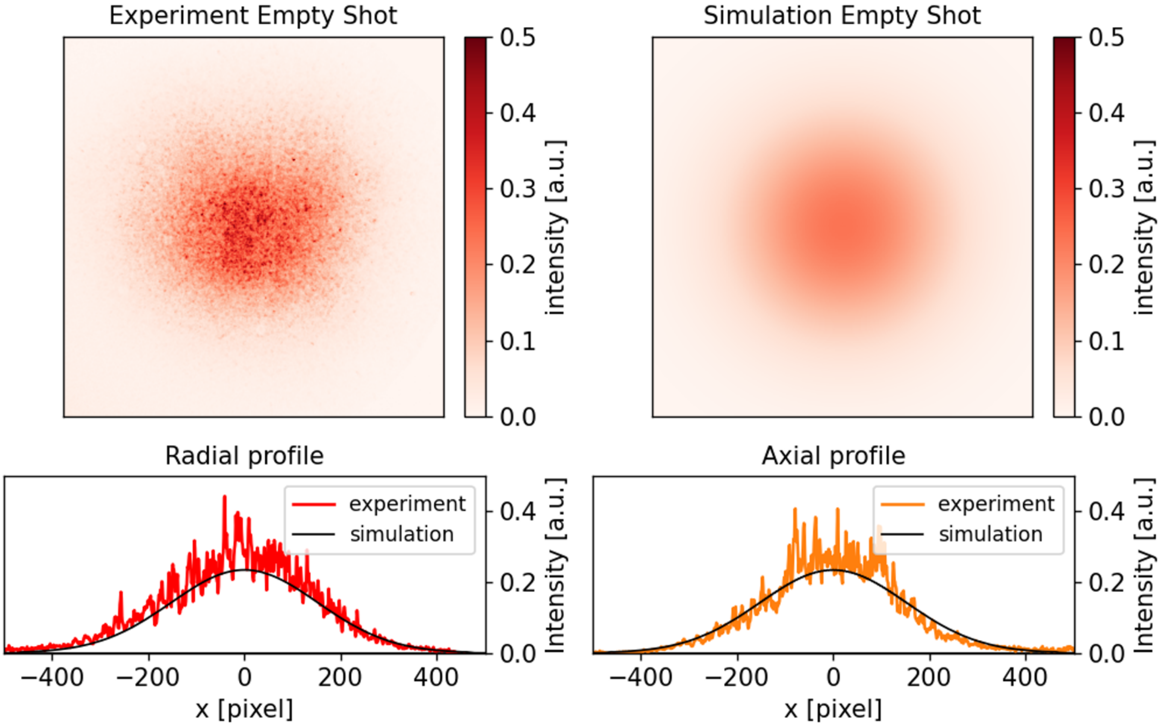

Figure 4.5: Comparison of the experimentally recorded beam profile on the probe screen (empty shot) and the final intensity distribution obtained from the probe simulation (empty shot).

beam has a Gaussian beam profile after the spatial filter, a combination of a Gaussian aperture and a circular aperture is applied. The best overlap with the experimental reference was achieved for a Gaussian aperture with 8.5 mm diameter (1/e intensity) and a circular aperture of 18.5 mm diameter. Figure 4.5 shows a comparison of the calculated intensity distribution and an exemplary recorded empty shot image.

The second reference are experimentally obtained diffraction patterns from non-ionized 1 μm plastic spheres with known refractive index. As those patterns result from the interaction with a well defined target, they can be used to calibrate the propagation distance between the probe focus and the target position. By implementing a density distribution that represents such a sphere, this distance can be adjusted until the simulated diffraction pattern best matches the experimental equivalent (figure 4.6). Using this method, a propagation of 0.77 mm yielded the best overlap and is in line with the experimentally approximated value of 1 mm.

A closer look at figure 4.6 reveals a small ovality of the experimentally recorded

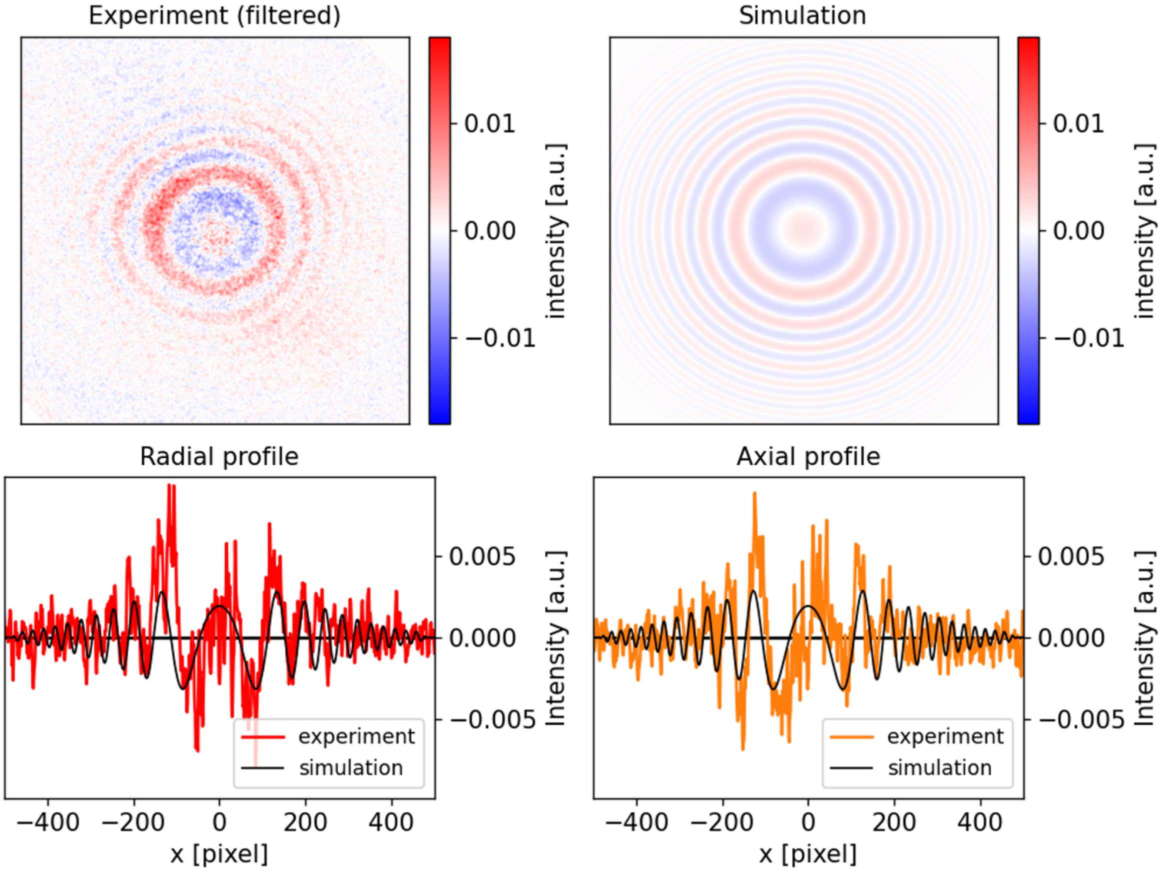

Figure 4.6: Comparison of the experimentally obtained diffraction pattern of an unexpanded 1 μm plastic sphere and the final intensity distribution obtained from the probe simulation.

diffraction pattern. It is assumed that this ovality is the result of a slightly skewed passage of the probe pulse through the focusing lens in the experiment. To account for this, a vertical astigmatism is imprinted on the input field with the help of a second order Zernike aberration. Using this approach, the ovality can be nicely reproduced in the simulation (good overlap between experiment and simulation in both dimensions in figure 4.6). The amount of aberration was determined for each data set recorded within a single campaign to include daily alignment changes and amounted between 0.23 λ and 0.27 λ.

4.1.3 Implementation of Density Distribution

The optical properties of the original sphere and respectively the plasma are implemented in the simulation by a discrete three-dimensional refractive index distribution.

The initial target is assumed to be a sphere with a diameter of 1 μm and a refractive index of 1.577. After the interaction with the pump pulse we assume the refractive index of a collisionless plasma:

$$\eta\left(\vec{r}\right) = \sqrt{1 - \frac{n_e\left(\vec{r}\right)}{n_c}} \tag{4.1}$$

where $n_e\left(\vec{r}\right)$ denotes the electron density distribution and n_c the critical density of the laser.

LightPipes offers the possibility to propagate the light field over a specified distance through a square two-dimensional array with inhomogeneous refractive index distribution via the 'Step' function. To represent the three-dimensionality of the sphere or plasma, the refractive index distribution is divided along the propagation direction (z) into successive slices of 2D arrays (xy). The concept is visualized in figure 4.7. The sum of all two-dimensional arrays forms a box in which the entire density distribution is implemented. Effects on the field are calculated slice by slice over the whole propagation length through the box.

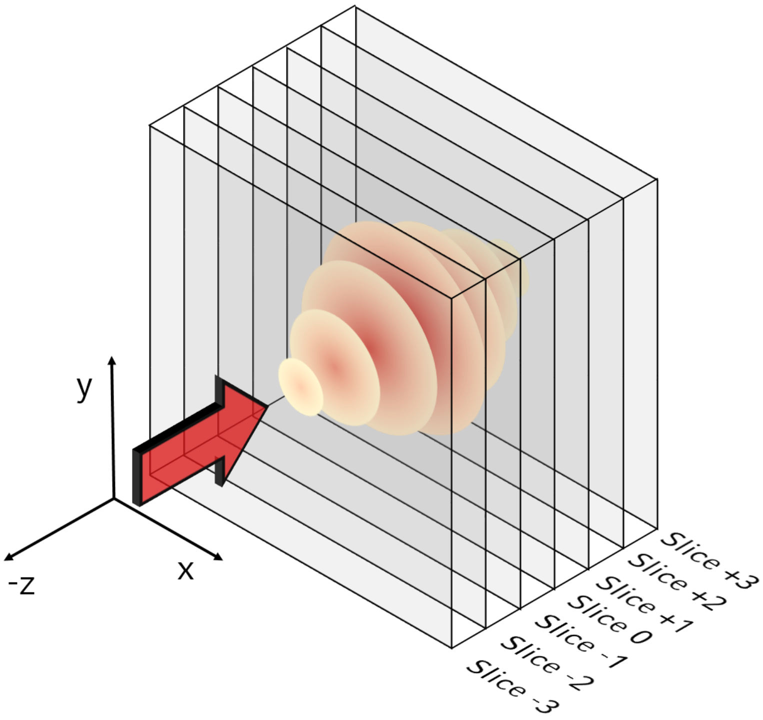

Figure 4.7: Concept of implementation of the density distribution: The 3D distribution is divided along the propagation axis z into a set of 2D arrays each containing a specified slice of the total density distribution

At the beginning of each simulation, the total size of the density distribution is determined first. Based on this distribution, the number and thickness of each slice is specified. For the initial target, this size is defined by the sphere diameter. For plasmas, the case is different: since the density distribution is calculated by analytical functions, it may happen that the density distribution has no defined end ($n_e = 0$). This would lead to an unpredictable number of slices. Therefore, the density distribution is limited in all three dimensions to the radius r_{targ}. r_{targ} is artificially defined such that the integral over the density distribution $\int\limits_0^{r_{targ}} 4\pi n_e\left(r\right) r^2 dr$ yields 99.99% of all electrons. To guarantee a uniform resolution in all dimensions, r_{targ} is divided by the resolution of the xy-grid. This results in the number of slices n_{slices}. The thickness of each slice is chosen to match the grid resolution.

The density distribution is given as $n_e\left(\vec{r}\right)$, which reduces to $n_e\left(r\right)$ under the assumption of spherical symmetry (see next section). For a implementation in the simulation this needs to be transformed into $n_e\left(x, y, z\right)$. Each grid point within the box of the density distribution is defined by its position x_{ijk}, y_{ijk}, z_{ijk}. In order to assign a radius r to each point, the position of the center (x_0, y_0, z_0) of the density distribution is determined. This value is in the center of the array which is defined by $n_{slices}/2$ (see slice 0 in figure 4.7). The distance to this center results in a radius for each position via

$$r_{ijk} = \sqrt{\left(x_{ijk} - x_0\right)^2 + \left(y_{ijk} - y_0\right)^2 + \left(z_{ijk} - z_0\right)^2}. \tag{4.2}$$

With this radius, the value of the refractive index $\eta\left(r_{ijk}\right)$ belonging to the specific position can be assigned from the analytical function. Since in reality the distribution is not always located in the center of the laser focus, there is also the possibility to move the center along x and y. A shift along the z axis can be realized by changing the propagation lengths prior to the target simulation.

The implementation of the individual values of the refractive index is subject to a restriction with regard to the continuity of the distribution. Each point of the array can only be assigned to a single value depending on the distance to the center; the same applies to the thickness of the array. Accordingly, an analytically continuous distribution must be approximated in the simulation in the form of a step-like distribution (see figure 4.8). By choosing the best possible resolution at reasonable computational effort, this limitation was tried to be minimized. In both simulations, the grid resolution (pump 150 nm, probe 230 nm) is kept well below the wavelength of 790 nm. However, this must be considered with care for the simulation of small structures.

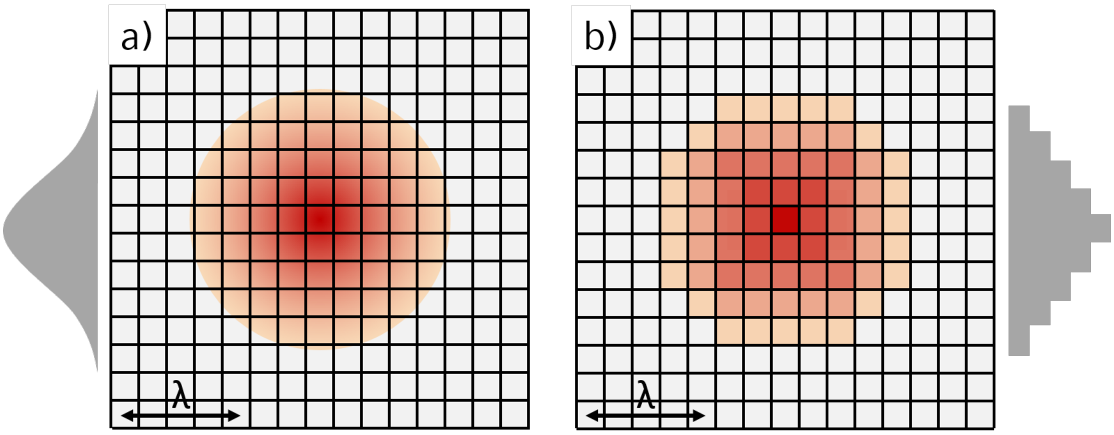

Figure 4.8: Discretization of the refractive index values: a) shows an exemplary analytic distribution, while b) illustrates how this distribution is implemented in the simulation.

Test case for implementation of overcritial densities It should be noted again that in case $n_e > n_c$ (overcritical density), the refractive index 4.1 has a purely imaginary value. This leads to a strong attenuation (shielding) of the electric field inside the plasma. As already described in section 2.4, the penetration depth after which the electric field drops to 1/e is the skin depth, which can be written in terms of particle densities as:

$$l_s = \frac{\lambda}{2 \cdot \pi \cdot \sqrt{\frac{n_e}{\gamma \cdot n_c} - 1}} \tag{4.3}$$

where λ is the laser wavelength and γ is the averaged Lorentz factor. In the present experiment with $I \approx 10^{16} \frac{W}{cm^2}$, $\gamma \approx 1$ and therefore does not play a significant role.

To ensure that the damping behavior is modeled correctly, the following test case was constructed (see figure 4.9(a)): a round beam with a diameter of 150 µm is generated in the center of a homogeneous field with flat phase. This beam is propagated a specified distance through a refractive index distribution using the 'Steps' function. The distribution is constructed in such a way that centrally within a circle of 100 µm diameter an imaginary refractive index emerges that corresponds to a defined overcritical electron density. Outside of this circle a real refractive index of 1 is used to represent vacuum. When passing through, the central part of the field is damped. By converting to the corresponding intensity distribution, it is then possible to check whether the damping is calculated correctly. Figure 4.9(b) shows the calculated transmitted intensities for three different electron densities. The black dashed line corresponds to the theortical attenuation as a function of the penetration depth x:

$$I(x) = I_0 \cdot e^{-2 \cdot \frac{x}{l_s}} \tag{4.4}$$

where I_0 is the intensity of the initial field and l_s the skin depth to the respective electron density.

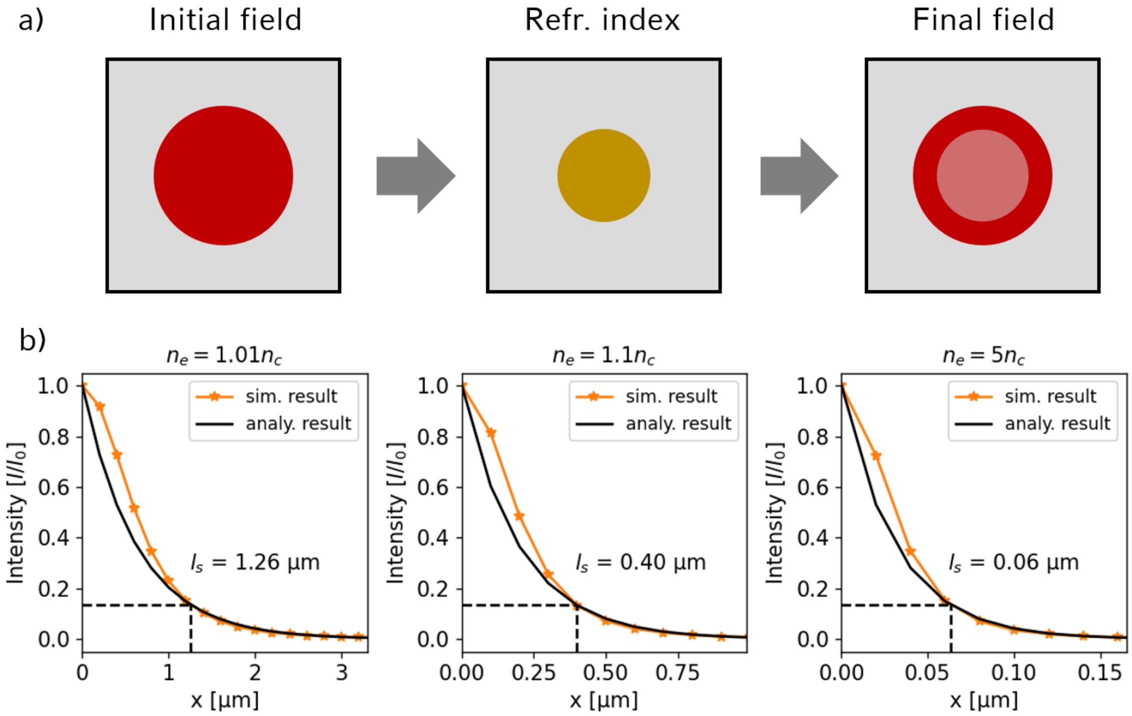

Figure 4.9: Test case for imaginary refractive index: a) illustrates the concept while b) shows results for the centrally transmitted intensity (orange line) compared to the theoretical damping (black line). The black dashed line indicates the position of the skin depth where the intensity drops to $1/e^2$ of the initial value.

As can be seen, the attenuation of intensity as a function of penetration depth resembles the theoretical model [1]. Deviations from the model occur for small pene-

---

[1] To achieve these results, a small modification in the implementation of the imaginary refractive

tration depths and attenuations. This is probably due to numerical inaccuracies and might improve with higher resolution. However, since the exponential decay of the intensity is in principal implemented correctly, it can be assumed that the transition to an overcritical plasma density, in particular the attenuation of the field by the overcritical region within the spherical microplasma is properly modeled in the presented simulations.

4.2 Density Models

As mentioned above, the aim is to compare the experimentally obtained diffraction patterns with results of the numerical simulations. In order to parameterize the plasma and its expansion, three simple models were developed to represent the electron density distribution of the plasma in the simulation. The choice of the models is based on findings of previous publications in the field of plasma expansion as well as evolutionary improvement in the understanding of the observed diffraction patterns. It is most important to note that although the diffraction patterns are dominated by the undercritical regions of the plasma density, where light can propagate and pick up phase, the models take into account all regions, even if not accessible by the diagnosing light. To keep the number of free parameters in the models small, the following simplifying assumptions were made:

Static distribution The models provide a static distribution function of the electrons based on the choice of parameters. For the simulation it is assumed that no time-dependent changes of this distribution occur over the observation period. For the pump, this assumption means that the overall electron density does not change during the 65 fs pulse duration, which means that intra-pulse dynamics are assumed to average out. The probe images can only give limited information with a temporal resolution of 2.6 ps and the effect of faster dynamics (in particular around t = 0 ps) must be considered later in the data analysis.

Spherical symmetry The modeled distributions are all spherically symmetric, as is the inital target. This assumption implies that the resulting plasma is heated uniformly and the thermalization time is small compared to the expansion time. Occurring

---

index in the 'Steps' function was necessary. A test case provided by the developers of the code was used to ensure this modification did not change the behaviour of the code in the case of a real-valued refractive index.

instabilities and asymmetric density disturbances (such as directed shocks or jets) cannot be considered quantitatively. This simplification is justified in the case of transmission of the pump when irradiating the target sphere centric. However, starting with spherically symmetric distributions as a zero order approximation (similar to the Zernike approach) is undoubtedly a valid starting point. Comparing the such calculated diffraction pattern with the experimental results (that show asymmetry) offers the possibility to determine the direction of occurring asymmetries and exploring their origin. For example, global distribution shifts within the laser can be taken into account in the simulation and illute the potential interpretation of deviations from symmetry.

Conservation of particle number For the calculation of the distribution it is assumed that the plasma is fully ionized and electrons are not able to escape from the plasma, i.e. the number of electrons in the system is constant at all times. The confinement might not be entirely valid. But it is worth highlighting that by using levitating and hence fully isolated targets, a refill from ground or non-irradiated target regions through the return current is impossible. This prior knowledge might be the most interesting constraint for interpreting the results.

4.2.1 Initial Sphere and Particle Number

Simulations of the initial sphere are used to validate the probing configuration. For each data set, it is also possible to determine whether the target was a single sphere or a cluster (comparison with data from probe only shots). In the simulation, the particle is implemented as a sphere with radius $r_0 = 0.5$ µm and homogeneous refractive index of 1.577. As the limiting radius, $r_{targ} = 1\ \mu m$ was used.

For the calculation of the electron density distribution of plasmas, the total number of electrons N_{tot} and the density in units of the critial density $n_0\,[n_c]$ present in the initial sphere is required. The target material polystyrene consists of $(C_8H_8)_n$ with a density of $1.05\,g/cm^3$ and a molar mass of $104.15\,g/mol$. Assuming complete ionization, the total number of electrons yields $N_{tot} = 1.78 \cdot 10^{11}$ and the corresponding electron density is $3.41 \cdot 10^{23}\,cm^{-3}$. With a critical density $n_c = 1.76 \cdot 10^{21}\,cm^{-3}$ for the central wavelength of the laser, this results in an initial, homogeneous density of $n_0 = 194\,n_c$ within r $< 0.5\ \mu m$.

4.2.2 Exponential Distribution

The first model describes the density distribution in terms of the critical density n_c with an exponential decay, similar to the model proposed by Peltz et al. [103]. The density initially distributes as a sphere with radius $r_0 = 0.5\,\mu m$ and a homogeneous density $n_0 = 194 n_c$ (see green curve in figure 4.10). As expansion starts, the function of the distribution can be divided into two segments (due to spherical symmetry only the radial distribution is defined):

$$n_e = \begin{cases} n_{core}, & r < r_{core}, \\ n_{core} \cdot e^{\frac{-(r - r_{core})}{d}}, & r \geq r_{core}. \end{cases} \tag{4.5}$$

In the range $0 < r < r_{core}$, the density has a constant value of n_{core} which corresponds to the initial density value n_0. r_{core} can take values between r_0 (initial sphere) and 0. The area outside of r_{core} describes a blurring of the sphere edge by an exponential decay of the density with increasing radius (red curve in figure 4.10). The parameter d defines the steepness of the decay.

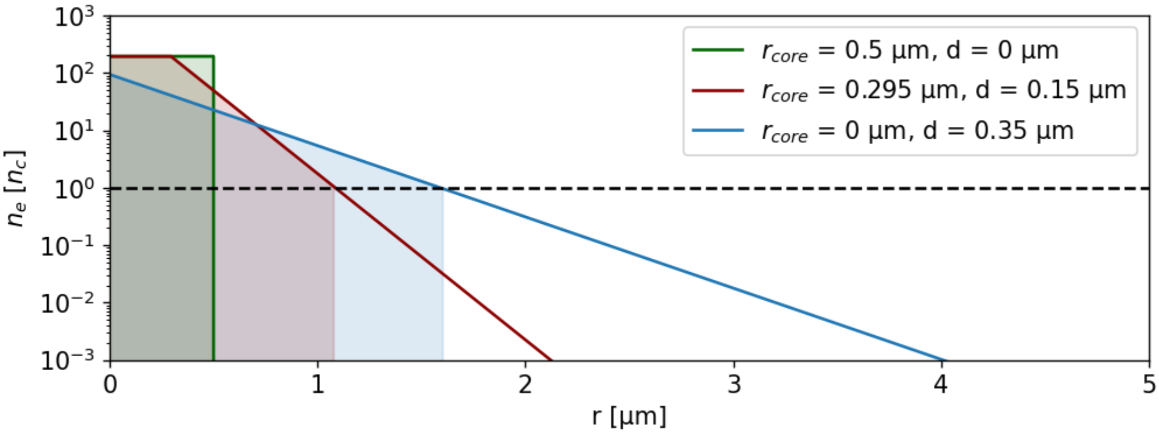

Figure 4.10: Three examples of the electron density model with exponential decay are shown: the green curve shows the initial plasma with $r_{core} = 0.5$ µm, the red curve illustrates the intermediate case with a shrinking core ($r_{core} = 0.295$ µm) and the blue curve depicts the case when the core density falls below the initial density ($r_{core} = 0$ µm).

At the beginning of the expansion, the density distribution can be described by an intermediate state (red curve in figure 4.10). Towards the interior, there is a homogeneous region of constant density whose radius r_{core} approaches 0 as the expansion progresses. Outside this area, the density decreases exponentially. As soon as r_{core} has dropped to 0, the density at r = 0 drops below the value of initial density. From here on, the profile is determined exclusively by the exponential decay (blue curve in figure 4.10).

For the simulation, the parameter d is changed, all other parameters are defined by the particle number conservation condition. The corresponding integral is calculated for both domains of the function:

$$\frac{N_{tot}}{4\cdot\pi} = \frac{n_0\cdot {r_0}^3}{3} = \int\limits_{0}^{r_{core}} dr\, r^2\cdot n_{core} + \int\limits_{r_{core}}^{\infty} dr\, r^2\cdot n_{core}\cdot e^{\frac{-(r-r_{core})}{d}}, \tag{4.6}$$

where N_{tot} is the total number of electrons in the plasma. From this, the corresponding density n_{core} can be determined for the given d:

$$n_{core} = \frac{n_0\cdot {r_0}^3}{{r_{core}}^3 + 3\cdot d\cdot({r_{core}}^2 + 2\cdot d\cdot r_{core} + 2\cdot d^2)}. \tag{4.7}$$

Since n_{core} is upper bounded by the value n_0, this also defines the parameter r_{core} in the range $0\,\mu m < d \leq 0.295\,\mu m$. For $d > 0.295\,\mu m$ the value of n_{core} falls below n_0 and r_{core} thus becomes 0.

To determine the limiting radius of the distribution for the simulation as described above, the integral of the distribution of r_{targ} is calculated up to a radius of 500 µm:

$$N_{outside} = \int\limits_{r_{targ}}^{500\,\mu m} dr\, r^2\cdot n_{core}\cdot e^{\frac{-(r-r_{core})}{d}}, \tag{4.8}$$

where $N_{outside}$ is the number of particles outside the sphere spannend by r_{targ}. r_{targ} is chosen such that $N_{outside} = 10^{-4}N_{tot}$.

In the following, an exemplary comparison of simulation results with experimentally acquired data is shown. This example serves to verify the model and is therefore only compared qualitatively. A detailed description of the methodology used to determine the agreement between simulation and experiment is given in the next section. The shot used for comparison was taken in the probe setting at time t = 0 ps. Therefore, it offers the optimal opportunity to investigate the density model simultaneously in the simulation of pump and probe. Since both diagnostics represent the same plasma state in time (except for potential asymmetries), the result of both simulations should match the experimental images for the same set of parameters. In the experimental data, the transmission shows a significant darkening of the recorded beam profile. In addition, a corona is cleary recognized. It is therefore assumed that the particle was hit by the laser and the plasma is already expanding. The diffraction pattern of the probe also shows clear changes compared to the image taken with probe only, which represents the diffraction pattern of the initial, un-ionized plastic sphere. The shot is therefore suitable to verify the modeling of the density gradient.

First, the simulation of the pump transmission is considered: Figure 4.11 compares experimentally acquired images and the corresponding simulations. In a) the acquired transmission image with target is depicted. The best matching simulation result with $d = 0.6\,\mu m$ and a resulting core density of 18.7 n_c is presented in b). In principle, the intensity distribution of the two profiles agrees well here. The percentage reduction of the integrated brightness in the experiment by 26.7 % can be reproduced in the simulation with a value of 28.9 %.

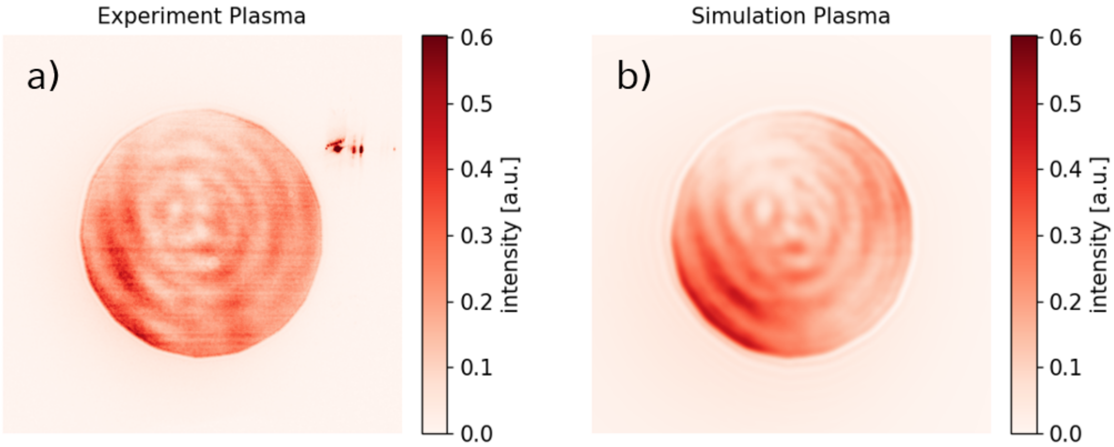

Figure 4.11: Comparison of experimentally recorded and simulated transmission images using the density model with exponential decay: a) shows the experimentally recorded image and b) the corresponding best-fit simulation result.

However, a close comparison of the intensity profiles reveals significant deviations. Figure 4.12 shows horizontal and vertical profiles of figure 4.11 a) and b). Differences can be seen especially in the shape of the corona but also in parts of the central beam profile. This type of deviation is present in many other examined data sets.

Looking at the probe, the comparison of experiment and simulation yields the fol-

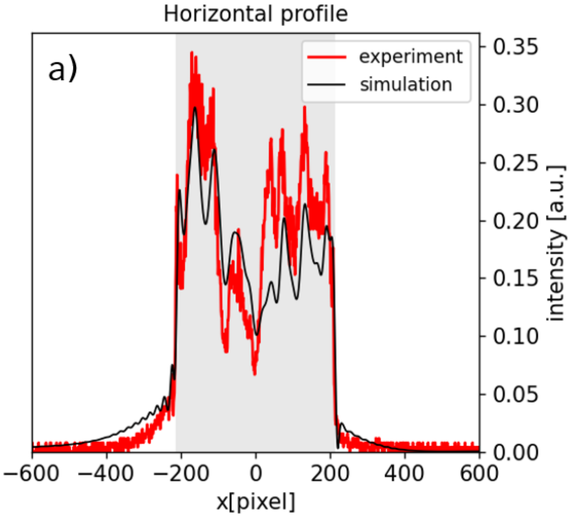

Figure 4.12: Profiles of images in 4.11 a) and b): horizontal (a)) and vertical (b)), where the colored curves represent experimental data and the black curves show simulation results. The grey area marks the area illuminated by the empty shot, indicating the onset of the observed corona.

lowing result: Figure 4.13 shows in a) the recorded diffraction pattern after scattered light has been filtered from the raw data. The corresponding simulation with d = 0.6 µm is shown in b). There is qualitative resemblence.

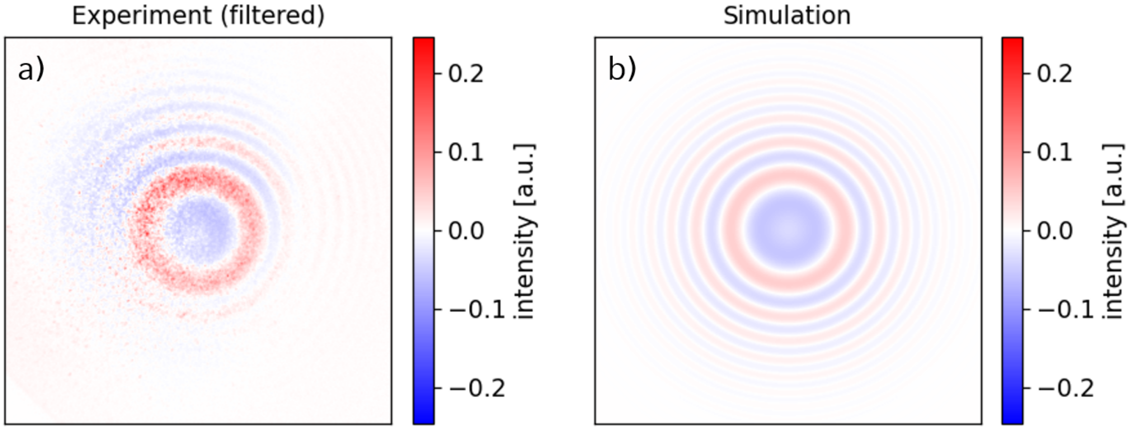

Figure 4.13: Comparison of experimentally recorded and simulated probe images using the density model with exponential decay: a) shows the experimentally recorded image with applied filtering while the corresponding simulation result is presented in b).

The analysis of radial and axial profiles (figure 4.14) confirms this similarity. Wherever rings are clearly formed and identifiable, the positions of the peaks in simulation

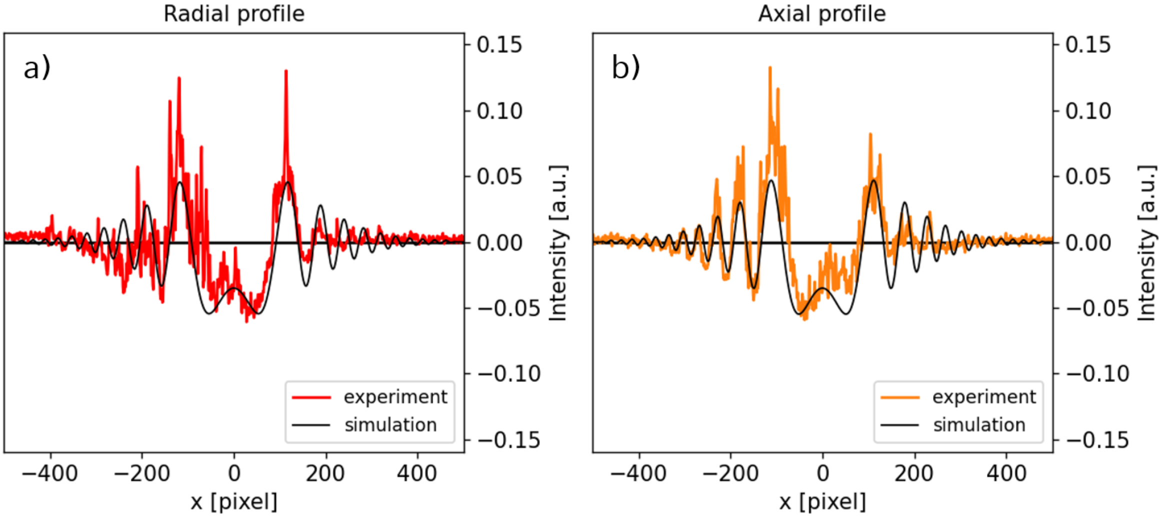

Figure 4.14: Profiles of images in 4.13 a) and b): radial (a)) and axial (b)); the colored curves represent experimental data and the black curves show simulation results.

and experiment agree. Also, the relationship of the individual peak heights to each other can be reproduced well by the simulation. A slight deviation can be observed in the height of the central peak in the axial profile.

In summary, the density model with exponential decay is in principle able to explain the general appearance of experimental images at t = 0 ps, which indicates that the chosen parameters model the size and core density of the plasma in the correct order of magnitude. However, significant discrepancies between experimental data and simulation are evident, especially for the transmission image of the pump. It is postulated that these deviations can be reduced by adapting the profile of the density gradient. Moreover, the distribution would form a non-vanishing static shock in the center when r_{core} becomes zero. This is unsatisfying and will be resolved by empirically extending the complication of the density model.

4.2.3 Single Gaussian Distribution

The second model of the electron density distribution describes the decay of the density at the edge of the sphere with a Gaussian function. This model is based on theoretical predictions of the plasma expansion by Kovalev et al. [104] and Murakami et al. [105]. As in the case of exponential decay, the distribution starts with a sphere of diameter $r_0 = 0.5\,\mu m$ and homogeneous density $n_0 = 194\,n_c$. In the same way, the distribution divides again into two sections with constant density n_{cold} in the range $0 < r < r_{cold}$ and the Gaussian decay for $r \geq r_{cold}$ with l_{cold} defining the steepness of the decay:

$$n_e = \begin{cases} n_{cold}, & r < r_{cold}, \\ n_{cold} \cdot e^{\frac{-(r-r_{cold})^2}{2 \cdot l_{cold}^2}}, & r \geq r_{cold}. \end{cases} \tag{4.9}$$

The index "cold" might be suprising here but will become clear when introducing the final density model. Figure 4.15 represents the initial state (green curve), an intermediate state of early expansion with a homogeneous plateau of radius $r_{cold} = 0.213\,\mu m$ and steep decay ($l_{cold} = 0.2\,\mu m$) (red curve), and a pure Gaussian distribution with $n_e < n_c$ and $l_{cold} = 0.8\,\mu m$ (blue curve).

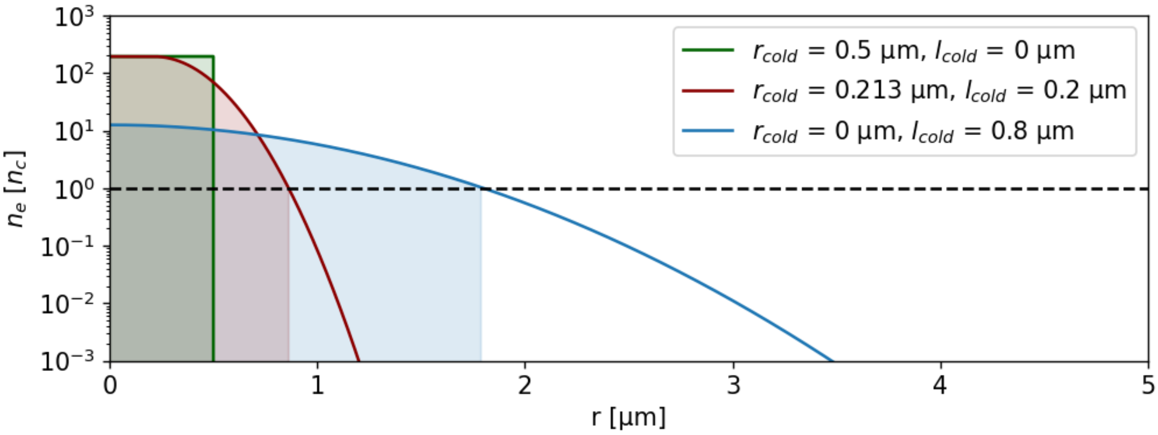

Figure 4.15: Three examples of the electron density model with Gaussian decay: the green curve shows the initial plasma with $r_{cold} = 0.5$ µm, the red curve illustrates the intermediate case with a shrinking core ($r_{cold} = 0.213$ µm) and the blue curve depicts the case when the core density falls below the initial density ($r_{cold} = 0$ µm). The distribution becomes an ordinary Gaussian function.

After choosing the variable simulation parameter l_{cold}, all other parameters are determined again by the condition of particle number conservation. The total number of electrons is calculated via:

$$\frac{n_0 \cdot {r_0}^3}{3} = \int_0^{r_{cold}} dr\, r^2 \cdot n_{cold} + \int_{r_{cold}}^{\infty} dr\, r^2 \cdot n_{cold} \cdot e^{\frac{-(r-r_{cold})^2}{2 \cdot l_{cold}^2}}. \tag{4.10}$$

For the core density n_{cold} this yields:

$$n_{cold} = \frac{n_0 \cdot {r_0}^3}{{r_{cold}}^3 + \frac{3}{2} \cdot l_{cold} \cdot \left({r_{cold}}^2 \cdot \sqrt{2 \cdot \pi} + 4 \cdot l_{cold} \cdot r_{cold} + l_{cold}^2 \cdot \sqrt{2 \cdot \pi} \right)}, \tag{4.11}$$

while r_{cold} is once more defined by the upper limit of $n_{cold} = n_0$ for $0 < l_{cold} \leq 0.321\,\mu m$ and $r_{cold} = 0$ for all other values of l_{cold}. For the calculation of the limiting radius, the same conditions apply as before, but the calculation is adjusted according to the distribution function to:

$$N_{outside} = \int\limits_{r_{targ}}^{500\,\mu m} dr\, r^2 \cdot n_{cold} \cdot e^{\frac{-(r-r_{cold})^2}{2 \cdot l_{cold}^2}} . \tag{4.12}$$

Simulations of probe and transmission are compared with the same experimental data as before. The best overlap is obtained with a value of $l_{cold} = 1.1\,\mu m$ and a core density of $n_{core} = 4.8\,n_c$.

The experimental image and the reconstruction agree to a large extent (figure 4.16). This also reflects in the percentage of brightness loss whereby the simulated value of 29.4% is very close to the experimentally determined percentage of 26.7%.

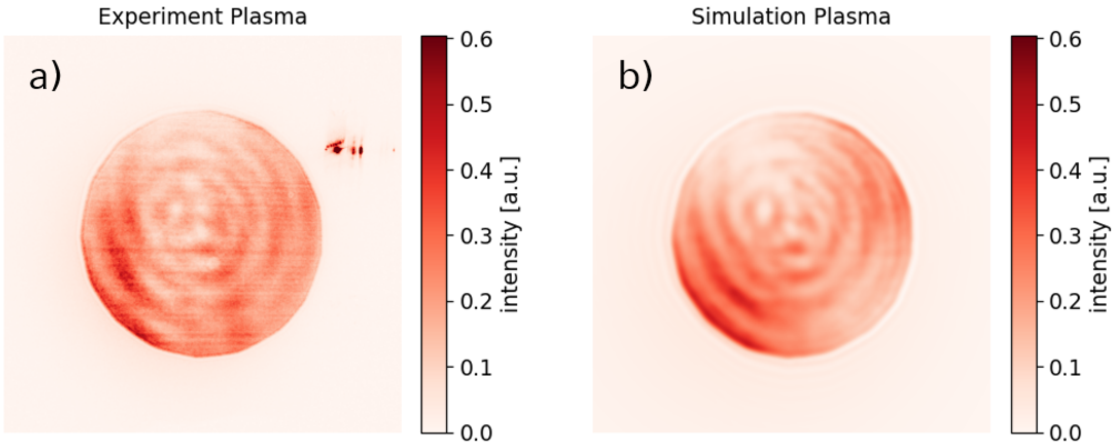

Figure 4.16: Comparison of experimentally recorded and simulated transmission images using the density model with Gaussian decay: a) shows the experimentally recorded image and b) the corresponding best-fit simulation result.

The analysis of the profiles (figure 4.17) shows a higher correlation than the model with exponential decay, especially in the central area. The shape of the corona also

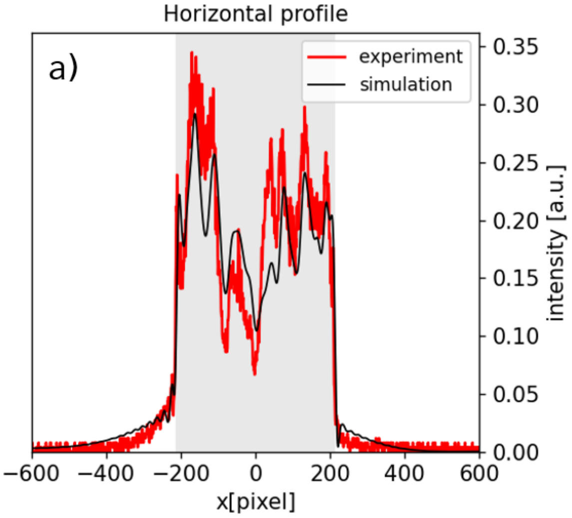

Figure 4.17: Profiles of images in 4.16 a) and b): horizontal (a)) and vertical (b)), where the colored curves represent experimental data and the black curves show simulation results. The grey area marks the area illuminated by the empty shot, indicating the onset of the observed corona.

fits better here, although there are still deviations in steepness. This discrepancy can also be found in other transmission images examined. Here the extent of the deviation becomes larger the more prominent the corona is in the experimental images.

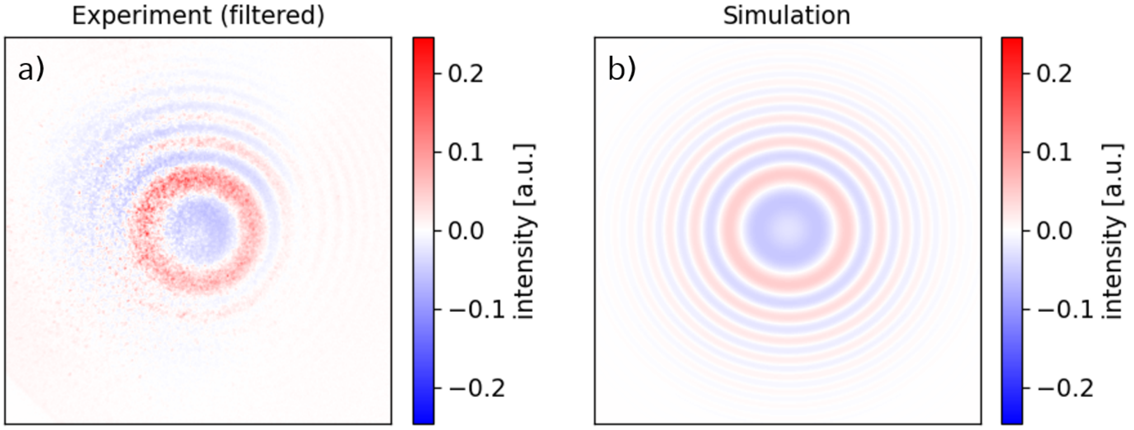

Figure 4.18: Comparison of experimentally recorded and simulated probe images using the density model with Gaussian decay: a) shows the experimentally recorded image with applied filtering while the corresponding simulation result is presented in b).

Similar to the previous model, the recorded image of the probe and the corresponding simulation match in appearance and brightness (see figure 4.18). The comparison

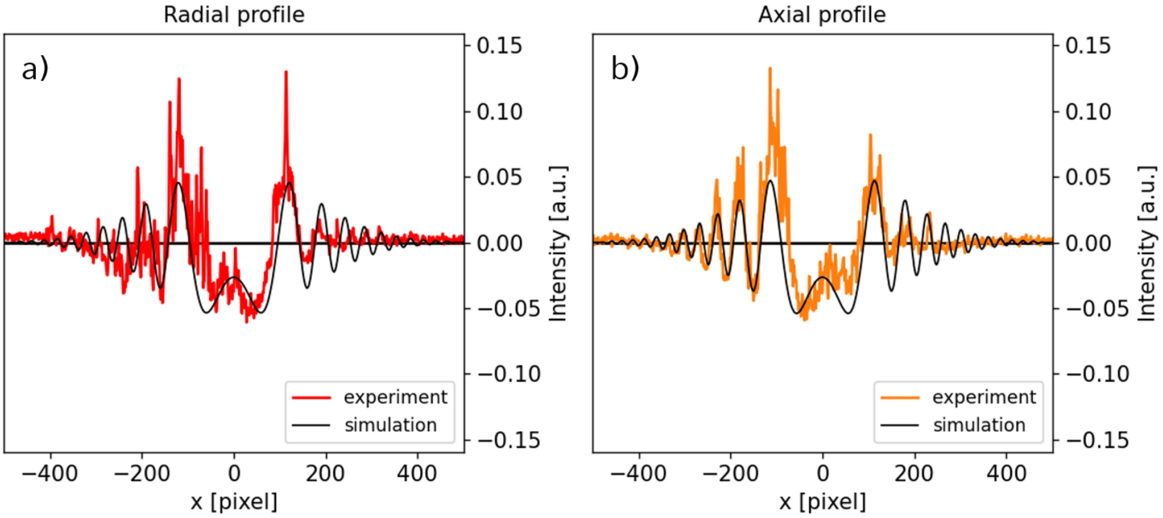

Figure 4.19: Profiles of images in 4.18 a) and b): radial (a)) and axial (b);, the colored curves represent experimental data and the black curves show simulation results.

of the profiles (figure 4.19) shows that the Gaussian gradient represents the height of the central peak better. Similarly, the height and position of the remaining peaks overlap well with the simulation. Almost all (except for one) evaluated probe data recorded at probe times t $>$ 39 ps can be approximated with good agreement using an ordinary Gaussian distribution function. It is therefore assumed that for late times this distribution gives a physically correct representation of the plasma. For earlier times and especially for the transmission inspecting the plasma state at time t $=$ 0 ps, though improved with respect to the exponential decay model, only partial agreement is achieved. In summary, the modeling of the density gradient with a Gaussian distribution seems to improve matters, but for regions around and shortly after the time of interaction of the pump pulse with the target, a more complex structure of the plasma is present which requires a further modification of the simple Gaussian decay model.

4.2.4 Dual Gaussian Distribution

Both previous models are based on the assumption that the electron distribution decays smoothly towards the outside and can be described by a single distribution function. However, several experimental findings indicate that a two-temperature model is often more appropriate (see e.g. [106, 107]). In addition, shocks are likely to occur during the laser-induced expansion of spherical clusters (see e.g. [108]). To implement this fact in the modeling of the electron density distribution, a second Gaussian distribution is added to the single Gaussian decay model. Two scenarios are distinguished: in the first case the additional Gaussian function is stationary at r = 0 for all times, while in the second case an additional parameter r_{hot} is introduced which describes the shift of the second Gaussian function relative to the center r = 0.

Centered Gaussian The distribution of electron density in the centered case can be expressed as follows:

$$n_e = \begin{cases} n_{cold} + n_{hot} \cdot e^{\frac{-r^2}{2 \cdot {l_{hot}}^2}}, & r < r_{cold}, \\ n_{cold} \cdot e^{\frac{-(r - r_{cold})^2}{2 \cdot {l_{cold}}^2}} + n_{hot} \cdot e^{\frac{-r^2}{2 \cdot {l_{hot}}^2}}, & r \geq r_{cold}. \end{cases} \tag{4.13}$$

n_{cold} defines the height of the original Gaussian distribution whose decay is given by the parameter l_{cold}. The implementation of the plateau described above for early stages of the expansion is achieved by the parameter r_{cold}. This also explains the choice of the index "cold" in the previous subsection. The additional Gaussian distribution is determined in its shape by n_{hot} and l_{hot}. For the simulation the parameters l_{cold}, n_{hot} and l_{hot} have to be chosen, which drastically increases the number of possible distributions. Via particle number conservation

$$\frac{n_0 \cdot {r_0}^3}{3} = \int\limits_0^{r_{cold}} dr\, r^2 \cdot n_{cold} + \int\limits_{r_{cold}}^{\infty} dr\, r^2 \cdot n_{cold} \cdot e^{\frac{-(r - r_{cold})^2}{2 \cdot {l_{cold}}^2}} + \int\limits_0^{\infty} dr\, r^2 \cdot n_{hot} \cdot e^{\frac{-r^2}{2 \cdot {l_{hot}}^2}}. \tag{4.14}$$

n_{cold} will then be fixed by the choice of l_{cold}, n_{hot} and l_{hot}:

$$n_{cold} = \frac{n_0 \cdot {r_0}^3 - 3 \cdot n_{hot} \cdot \sqrt{\frac{\pi}{2}} \cdot {l_{hot}}^3}{{r_{cold}}^3 + \frac{3}{2} \cdot l_{cold} \cdot \left({r_{cold}}^2 \cdot \sqrt{2 \cdot \pi} + 4 \cdot l_{cold} \cdot r_{cold} + {l_{cold}}^2 \cdot \sqrt{2 \cdot \pi} \right)}. \tag{4.15}$$

The selection criterion for r_{cold} is done as follows: starting with $r_{cold} = 0$, the distribution is calculated from the chosen parameters (l_{cold}, n_{hot} and l_{hot}). If the resulting density $n_e\,(r = 0)$ is above the initial value of $n_0 = 194 n_c$, r_{cold} is adapted (between 0 μm and 0.5 μm) such that a plateau region with $n_e\,(r = 0) = n_0 = 194 n_c$ forms. In all other cases, $r_{cold} = 0$. The choice of n_{hot} and l_{hot} is also subject to a certain restriction in the context of particle number conservation. As both parameters can be freely chosen, one can create a distribution where the number of electrons in the additional Gaussian component can exceed the number of available electrons in the sphere. This will result in a negative value of n_{cold} via equation 4.15 and a negative number of electrons in the center of the plasma. Hence, before implementing the distribution in the simulation it is checked if the distribution is valid ($n_e > 0$ everywhere) or if values of l_{hot} and n_{hot} need to be lowered. Figure 4.20 again displays the initial state (green), a state of incipient expansion (red) and a state with $n_e\,(r = 0) < 194 n_c$ (blue).

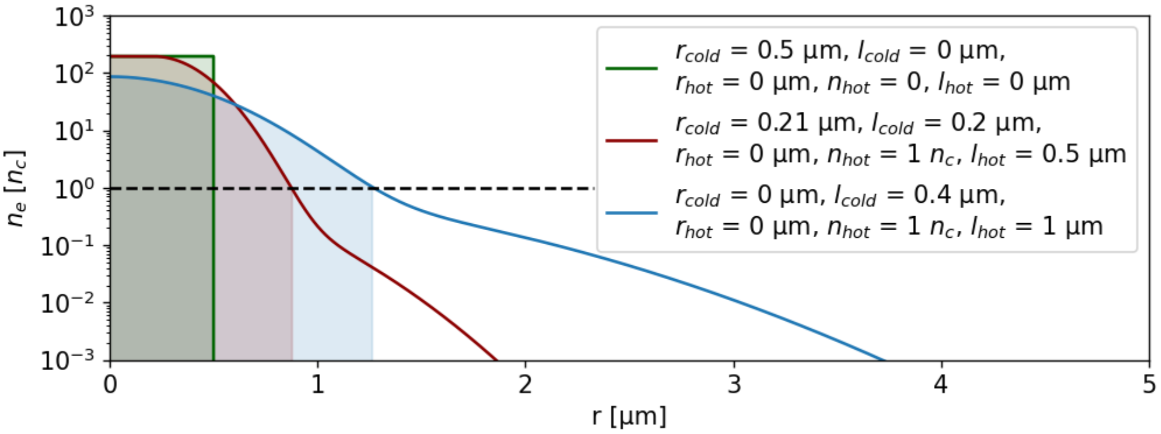

Figure 4.20: Three examples of the electron density model with two centered Gaussian distributions: the green curve shows the initial plasma with $r_{cold} = 0.5\ \mu m$, the red curve illustrates the case of early expansion with a shrinking core ($0 < r_{cold} < 0.5\,\mu m$) and the blue curve depicts the case when the central electron density ($n_e(r = 0)$) falls below the initial density.

When comparing figure 4.20 and figure 4.15, the resemblence is evident. It is not surprising that for reasonably small values of n_{hot} the curves are close to identical and result in similar agreement with experimental data. Hence, it was also not possible to reproduce the case of strong corona formation that was mentioned in the previous subsection.

Moving Gaussian By introducing an additional parameter r_{hot}, which describes a shift of the second Gaussian distribution, a spherical, decentralized accumulation of electrons can be represented in the plasma as it would be present, for example, in the formation of expanding shocks. The in this way extended density function reads:

$$n_e = \begin{cases} n_{cold} + n_{hot} \cdot e^{\frac{-(r-r_{hot})^2}{2 \cdot l_{hot}{}^2}}, & r < r_{cold}, \\ n_{cold} \cdot e^{\frac{-(r-r_{cold})^2}{2 \cdot l_{cold}{}^2}} + n_{hot} \cdot e^{\frac{-(r-r_{hot})^2}{2 \cdot l_{hot}{}^2}}, & r \geq r_{cold}. \end{cases} \tag{4.16}$$

Figure 4.21 once more represents the same three situations as in the previous models. Here, the influence of the moving second Gaussian distribution in the two cases of expansion (red and blue curve) is clearly evident by the emergence of steeper density gradients at the edges of the plasma.

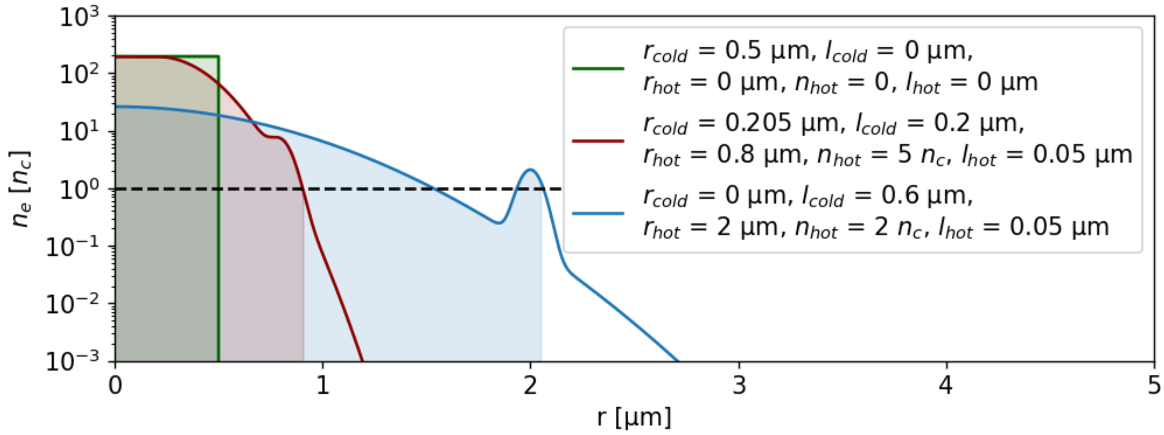

Figure 4.21: Three examplary states of the electron density model with one centered Gaussian distribution and an additional shiftable Gaussian: the initial plasma with $r_{cold} = 0.5$ µm (green curve), the case of early expansion with a shrinking core ($0 < r_{cold} < 0.5\,\mu m$) (red curve) and the case when the central electron density ($n_e(r = 0)$) falls below the initial density (blue curve).

The choice of simulation parameters is subject to the same conditions and constraints as in the case of the centralized dual Gaussian distribution. The rule of particle number conservation

$$\frac{n_0 \cdot {r_0}^3}{3} = \int\limits_0^{r_{cold}} dr\, r^2 \cdot n_{cold} + \int\limits_{r_{cold}}^{\infty} dr\, r^2 \cdot n_{cold} \cdot e^{\frac{-(r-r_{cold})^2}{2\cdot {l_{cold}}^2}} + \int\limits_0^{\infty} dr\, r^2 \cdot n_{hot} \cdot e^{\frac{-(r-r_{hot})^2}{2\cdot {l_{hot}}^2}} \tag{4.17}$$

leads to

$$\begin{aligned} n_{cold} =& \frac{-3 \cdot n_{hot} \left(e^{-\frac{r^2}{2\cdot {l_{hot}}^2}} \cdot {l_{hot}}^2 \cdot r_{hot} + l_{hot} \cdot \sqrt{\frac{\pi}{2}} \cdot \left({l_{hot}}^2 + {r_{hot}}^2\right) \left(1 + Erf\left(\frac{r_{hot}}{l_{hot}\cdot\sqrt{2}}\right)\right)\right)}{{r_{cold}}^3 + \frac{3}{2} \cdot l_{cold} \cdot \left({r_{cold}}^2 \cdot \sqrt{2\cdot\pi} + 4 \cdot l_{cold} \cdot r_{cold} + {l_{cold}}^2 \cdot \sqrt{2\cdot\pi}\right)} \\ &+ \frac{n_0 \cdot {r_0}^3}{{r_{cold}}^3 + \frac{3}{2} \cdot l_{cold} \cdot \left({r_{cold}}^2 \cdot \sqrt{2\cdot\pi} + 4 \cdot l_{cold} \cdot r_{cold} + {l_{cold}}^2 \cdot \sqrt{2\cdot\pi}\right)}. \end{aligned} \tag{4.18}$$

The comparison with the experimental data selected for validation provides the best agreement for the following parameters: $r_{cold} = 0\,\mu m$, $l_{cold} = 0.7\,\mu m$, $r_{hot} = 2.47\,\mu m$,

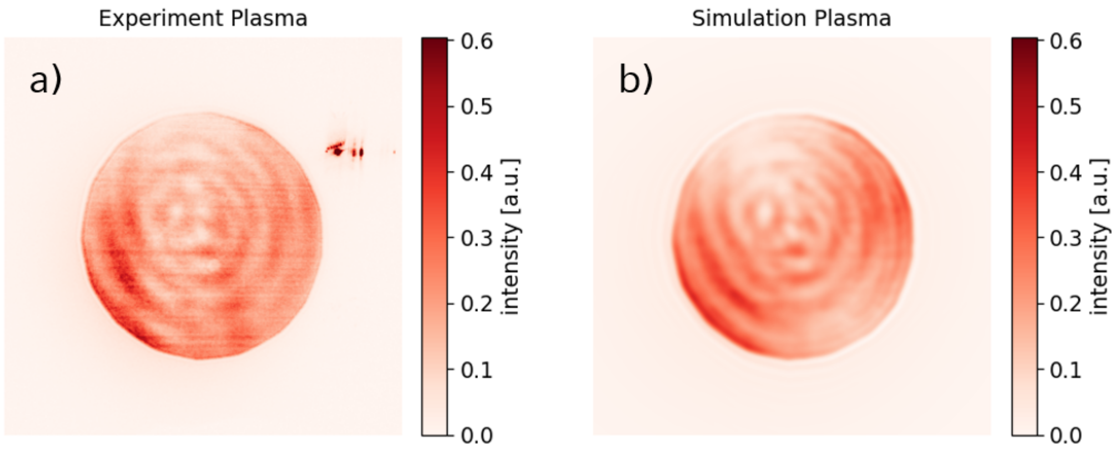

Figure 4.22: Comparison of experimentally recorded and simulated transmission images using the dual Gaussian density model with moving component: a) shows the experimentally recorded image and b) the corresponding best-fit simulation result.

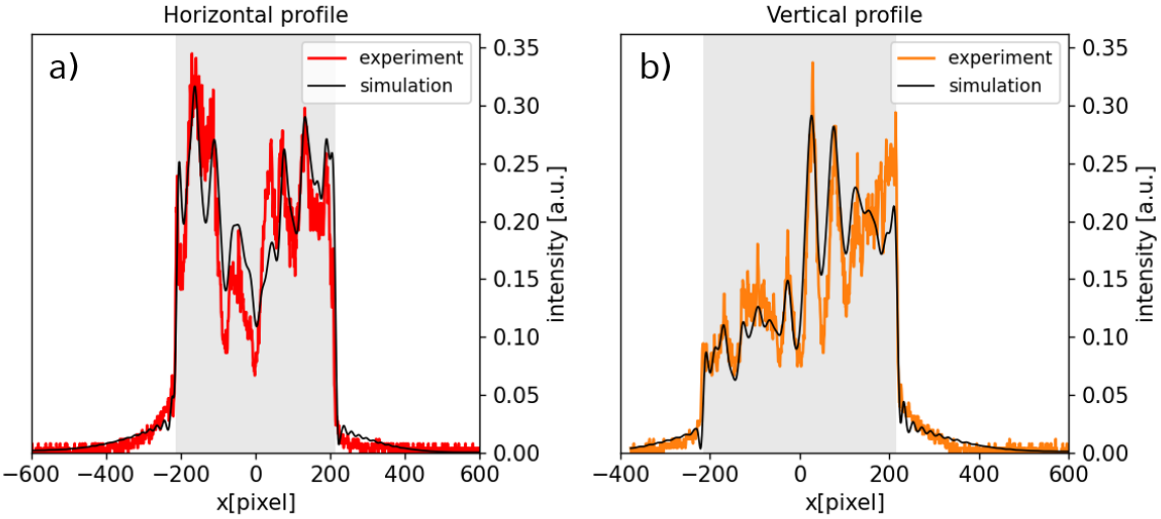

Figure 4.23: Profiles of images in 4.22 a) and b): horizontal (a)) and vertical (b)), where the colored curves represent experimental data and the black curves show simulation results. The grey area marks the area illuminated by the empty shot, indicating the onset of the observed corona.

$l_{hot} = 0.25\,\mu m$ and $n_{hot} = 1.25\,n_c$. The direct comparison of experimental raw transmission data with the simulation results (figure 4.22) shows an excellent agreement which is also reflected in a simulated darkening of 29.4 % compared to 26.7 % in the experiment. The analysis of the corresponding profiles (figure 4.23) reveals a clear improvement, both in the central beam profile and in the reproduction of the corona. This improvement can also be achieved in all other data sets where the previous models showed significant deviations.

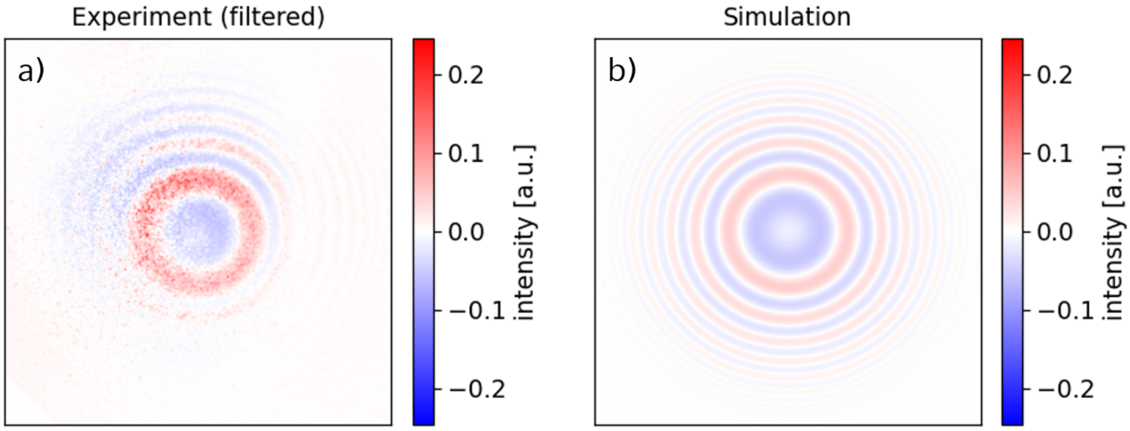

Figure 4.24: Comparison of experimentally recorded and simulated probe images using the dual Gaussian density model with moving component: a) shows the experimentally recorded image with applied filtering while the corresponding simulation result is presented in b).

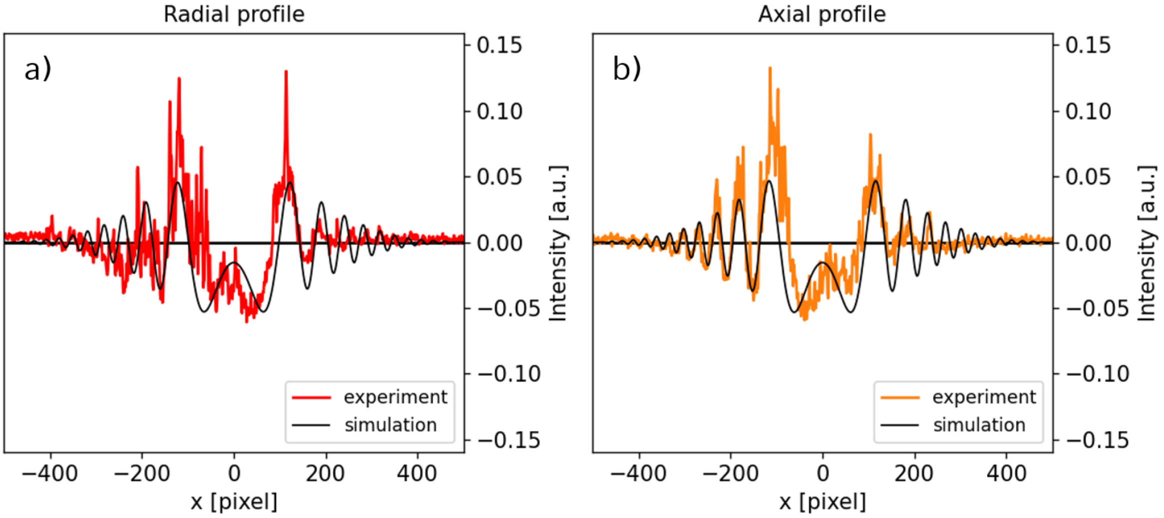

Figure 4.25: Profiles of images in 4.24 a) and b): radial (a)) and axial (b)); the colored curves represent experimental data and the black curves show simulation results.

The simulation of the probe (figure 4.24) reproduces the experimental results well. This is evident by inspecting the radial and axial profiles (figure 4.25) which correspond in terms of positions and heights of the central and first interference fringe.

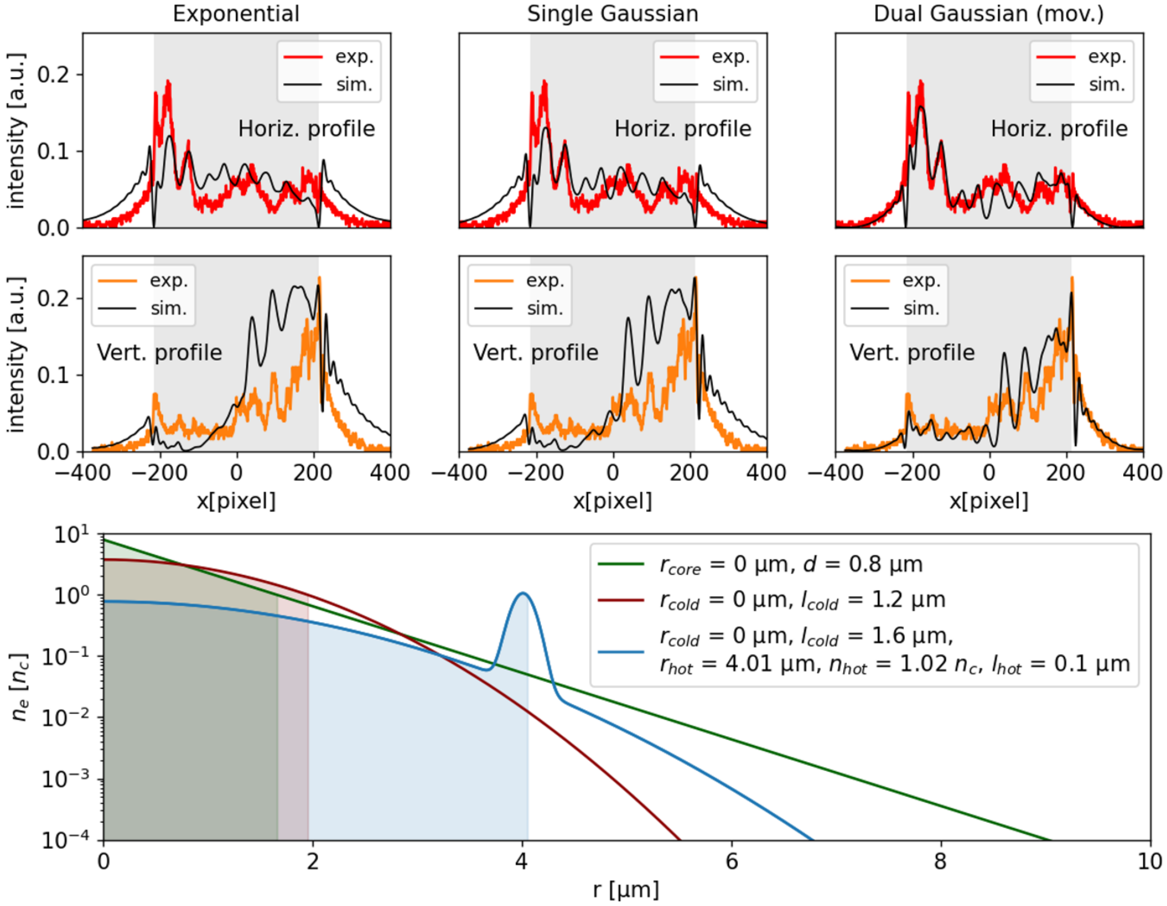

Figure 4.26: Direct comparison of horizontal and vertical profiles of reproduced pump transmission profiles (best fit) using all three models for an exemplary shot. The corresponding density profiles are shown below: exponential (green), single Gaussian (red) and dual Gaussian with moving component (blue). The shaded areas mark the region of overcritical density.

In summary, the model of dual Gaussian distribution with moving component is the only one capabale of representing the experimental result of both transmission and probe with a single set of parameters. The superiority of this model is further illustrated in figure 4.26: it shows the horizontal and vertical profiles of an exemplary pump transmission image (colored curves) and the corresponding best-fit reproduction of the simulation using the three different models described above (black curves). Only the model with additional, moving Gaussian component is able to achieve satisfactory overlap. From the density distributions of the models, shown below, it is evident that the additional component increases the area of overcrital density (shaded areas) and provides steeper gradients in the outer regions of the plasma, which both are likely the cause for the higher agreement. It is therefore assumed that this distribution function is sufficiently complex for describing the density distribution of plasma electrons over the complete period of the expansion. The already established agreement of the probe simulations at late times with the simple Gaussian distribution are contained and can be described by choosing $n_{hot} = 0$ for the second Gaussian component, which allows a smooth transition between both models.

4.3 RALEF Simulations

To support the empirically found agreement of the experimental data with the dual Gaussian distribution, simulations were performed using the 2D hydrodynamic code RALEF. The simulations, carried out by Dr. Anna Tauschwitz from the Goethe University Frankfurt am Main, allow time-resolved observation of all relevant parameters of the plasma, including the electron density distribution. RALEF is a powerful tool to model high-temperature plasmas as they are formed during the interaction with (non-relativistic) high-intensity laser pulses of arbitrary duration. It is based on a single fluid, single temperature hydrodynamic model. RALEF takes into account contributions from thermal conduction as well as thermal radiation and heating power of external energy sources (e.g. a laser) by solving the following fluid dynamics equations [86]:

$$\frac{\partial \rho}{\partial t} + \operatorname{div}\left(\rho \vec{u}\right) = 0, \tag{4.19}$$

$$\frac{\partial}{\partial t}\left(\rho \vec{u}\right) + \operatorname{div}\left(\rho \vec{u} \otimes \vec{u}\right) + \nabla p = 0, \tag{4.20}$$

$$\frac{\partial \left(\rho E\right)}{\partial t} + \operatorname{div}\left[\left(\rho E + p\right) \vec{u}\right] = Q_T + Q_r + Q_{dep}, \tag{4.21}$$

where ρ is the fuild mass density, $\vec{u}$ the fluid velocity, p the pressure and $E = e + u^2/2$ the total mass specific energy with internal energy e. Q_T and Q_r are source terms for thermal conduction and energy transport by thermal radiation, respectively[86]:

$$\begin{aligned} Q_T &= -\operatorname{div}\left(-\kappa \nabla T\right), \\ Q_r &= -\operatorname{div} \int\limits_0^\infty d\nu \int\limits_{4\pi} I_\nu \, \vec{\Omega} \, d\vec{\Omega}, \end{aligned} \tag{4.22}$$

where κ is the heat conduction coefficient, ν the photon frequency, I_ν the spectral intensity and $\vec{\Omega}$ the propagation direction of a photon. The transport of radiation energy is described by the quasi-static approximation $\vec{\Omega} \cdot \nabla I_\nu = k_\nu \left(B_\nu - I_\nu\right)$ with k_ν being the spectral absorption coefficient and B_ν the source function of radiation. Q_{dep} describes the volume-specific heating power of the external energy source. The energy dissipation rate (per unit volume) is obtained by solving the Helmholtz equations for the s- and p-polarized component of the electromagnetic field. A much more detailed describtion of the code can be found in [86]. The equation of state used for the calculation was generated by the FEOS code (see [109]).

For the simulation setup, rotational symmetry is assumed along the laser axis. The two available spatial dimensions are defined as follows: z corresponds to the propagation direction of the laser and r defines the distance to a defined point on the laser axis in a plane which is spanned by z and the axis perpendicular to it. The simulation box is limited by a semicircle with a radius of 25 mm. The corresponding grid is formed by a radial mesh whose resolution decreases towards the outside. The spherical target is a semicircle with radius 0.5 μm whose center is located in the middle of the simulation box and consists of carbon with an initial density of 1 g/cc (approximation for(C_8H_8)). The laser enters the simulation from the +z direction and is defined as a collimated beam with its spatial distribution assumed by a Gaussian distribution with 5.9 μm FWHM. The temporal evolution of the laser is implemented according to the experimentally determined contrast curve (see figure 3.14). Analogous to the experiment , the cycle-averaged peak intensity is $1.6 \cdot 10^{16}\, W/cm^2$ and the central wavelength of the laser is 793 nm.

In a first simulation, which started 1.8 ns before the arrival of the main pulse according to the measured contrast curve, it turned out that the expansion of the plasma at t = 0 ps was already very advanced to an undercritical plasma cloud. In the experiment we could prove, however, that up to 14 ps before the main pulse, the diffraction image recorded via the probe corresponds to the simulated image of an initial, non-ionized sphere. It is therefore assumed that the contrast measurement does not represent the actual intensity of preceding light on target and that in the experiment a smaller fraction of light than assumed interacts with the target prior to the main pulse. To make the hydrodynamics simulations comparable to the experimental data, it was decided to limit the interaction to a period from -14 ps to 0 ps to avoid pre-expansion under unspecific conditions. The further expansion of the plasma was simulated up to the time t = +200 ps.

Figure 4.27 shows results of the RALEF simulation at three different times (from top down t = 0 ps, t = +50 ps, and t = +200 ps). The left column shows the 2D electron density distributions at respective times extracted from the RALEF calculation. The central column contains the profiles of the density distribution (black dashed line) along the radial axis through the center of mass, the right column shows the density profile along the laser axis. For each profile, distribution functions of the moving dual Gaussian model whose parameters best reproduce the density profiles of the RALEF simulation are shown in orange. Since the density profiles at t = 0 ps only have a core density of $n_{core} = 34\,n_c$, this was adjusted accordingly in the calculation of the distribution function via fulfilling the condition of particle conservation for the adapted density.

At t = 0 ps, especially the radial profile agrees very well to the RALEF simulation results. For the axial profile along, several deviations can be observed. The radial symmetry, as assumed for the simple density models, does not correspond to the RALEF simulation, where a shock structure is visible on the laser-irradiated side only. Furthermore, the double-peaked density cannot be reconstructed with the dual Gaussian distribution. However, it is important to note that the outermost undercritical density regions remain well represented. This is of particular interest for calculating the diffraction pattern and we remind here that the overcritical region (marked by grey areas) remains inaccessible to the laser pulse. In fact, the agreement on the side facing the laser is good up to a density of 25 n_c. Thus, along the laser axis, both deviations lie in the shadow of an overcritical region and the shape within this overcritical region does not influence the diffraction pattern. For the probe the situation is different, the asymmetry along the laser axis should become visible in the diffraction patterns.

For t = +50 ps, a similar picture emerges. The radial component shows good agreement in the undercritical (accessible) region when adjusting the second gaussian to a peak at x = 0.8 µm. Due to the condition of particle number conservation, the peak density at x = 0 µm in our model ($\sim$ 140 n_c, peak not shown in figure 4.27) differs cleary from the RALEF simulations, however, this deviation is shielded from the laser. Along the laser axis, the asymmetry remains evident. The peak at the laser

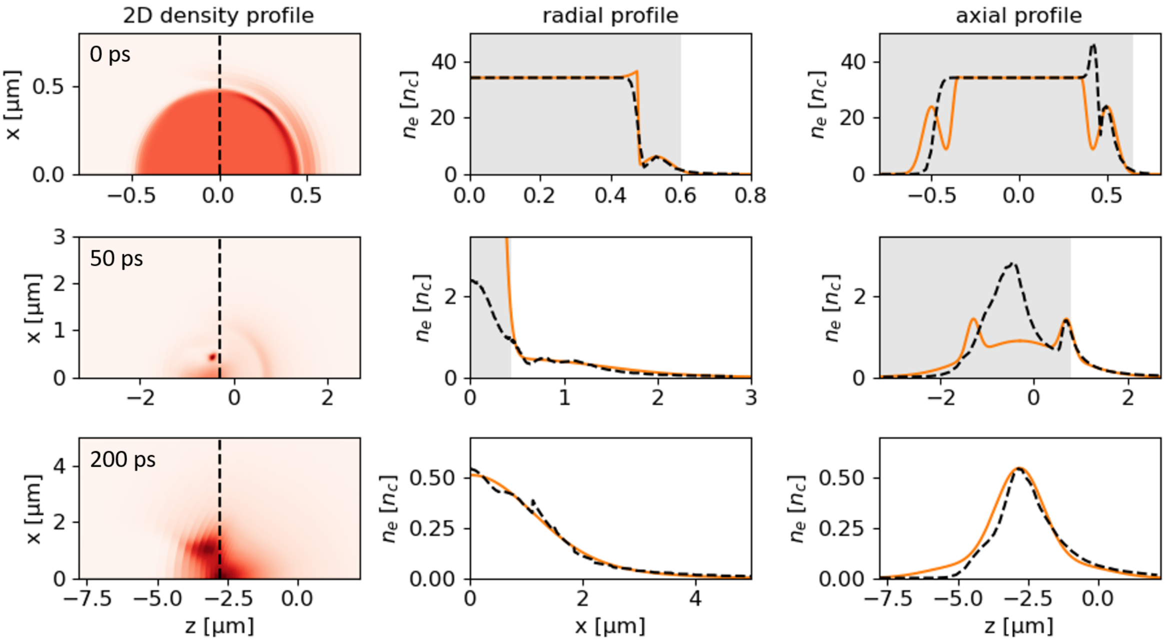

Figure 4.27: Comparison of RALEF simulation with moving dual Gaussian model: each row shows results of the RALEF simulation at distinct time steps (0 ps, +50 ps, +200 ps). Left column: 2D electron density distribution; dashed lines mark the center of mass position. Center and right column: density profiles (black dashed lines) along the radial axis through the center of mass and along z, respectively. Best-fit density distributions calculated with the moving dual Gaussian are superimposed as orange lines (parameters differ for horizontal and vertical profile). Peak of radial best-fit distribution at 50 ps ($\sim 140\ n_c$) is not shown. Grey regions mark the area of overcritical density, which are inaccessible to the laser pulse. The core density was adjusted to the RALEF simulation ($n_{core} = 34\, n_c$). The laser enters the simulation from the +z direction.

irradiated side can be described well by the distribution, but deviations at the density profile in the interior remain significant. On the side facing away from the laser, the RALEF density distribution follows a simple Gaussian curve and differs strongly from our model due to the assumption of spherical symmetry. However, those deviations are again located in the shadow of the overcritical region.

At late times (t = +200 ps), a density profile results in the RALEF simulation that, especially in the case of the radial axis, approximately follows a simple Gaussian curve. A second Gaussian distribution at x = 2 µm improves the match, but its influence on the overall profile shape is small. In the axial profile this influence is more obvious but also here the distribution approaches a simple Gaussian curve. In addition, the asymmetry becomes less pronounced. The RALEF simulations show that the density profiles evolve into a simple Gaussian distribution at late times. This is in line with the previously described agreement of probing simulations with the simple Gaussian model and the experimental data at late times.

It was shown that in comparison with the hydrodynamics simulation, only the empirically determined model of the Gaussian distribution with an additional, moving component is able to describe the decentralized increases in electron density occurring at early times. The previously determined transition to a single Gaussian distribution is in agreement with the RALEF simulation. Finally, it must be mentioned that the parameter sets of the distributions perpendicular and along the laser axis are not identical. This results from the assumption of radial symmetry in the simple density models which does not prevail in the hydrodynamics simulation. In order to keep the number of parameters in a manageable range, in the case of asymmetries the best-fit for each dimension of the plasma is determined in the later analysis of the experimental data and both sets are reported. The deviations are then considered in the error analysis.

4.4 Methodology

It is necessary to describe the selection criteria for choosing the parameters for the density distribution and for determining the best fit of simulation resuts with experimental findings for transmission and probe. In this context, it is outlined how the error ranges are estimated when reconciling experimental data and simulation results.

Selection criteria for best-fit parameter set for pump simulation

Figure 4.28 shows horizontal and vertical profiles of an exemplary pump transmission image. A distinction is made between two regions: the region defined by the beam profile of the empty shot and the region outside, in which light was only observed in shots with target. In the central region, the intensity distribution and the global reduction compared to the empty shot are the decisive factors (indicated by the bold arrow in a)). Outside, the decisive factors are the shape (right side of b)) and height of the forming corona as well as the relative height difference of the corona at the edges of the original beam profile (see black horizontal lines in a) and b)).

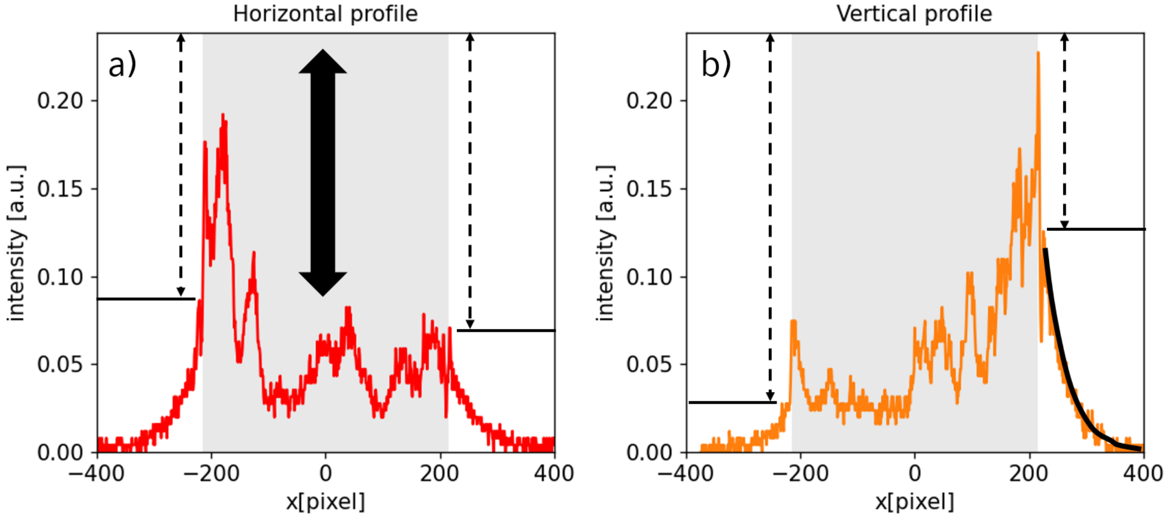

Figure 4.28: Profiles of exemplary transmission image indicating relevant parameters for choice of simulation paramteres: a) Reduction and shape of original beam profile (area marked in grey), b) shape (blacked curved line) and height (black horizontal lines) of corona forming outside of original beam.

Displacement of simulated sphere (x,y): Assuming spherical symmetry of the density distribution, it is obvious that an asymmetric occurrence of the corona is likely due to a shift of the distribution with respect to the lateral spatial distribution of the laser in focus. For the choice of the displacement perpendicular to the laser axis, the respective ratios of the corona heights at the edge of the original beam profile as well as their absolute heights are analysed. A shift away from the center in the horizontal direction provides a change in the ratio of the corona heights in the horizontal profile. Furthermore, due to the spatial shape of the intensity distribution in focus, this also leads to a reduction of both corona heights in the case of the vertical profile. More generally, any shift away from the center leads to a less intense corona as compared to the case of a centrally placed plasma. Matching the corona heights of all four edge regions of the profiles, these findings can be used to determine the position of the density distribution and thus also the overlap between target and laser when comparing experiment and simulation.

Position of moving Gaussian $\mathbf{r_{hot}}$: r_{hot} describes the position of the moving Gaussian distribution and has significant influence on the entire transmitted beam profile. On the one hand, r_{hot} defines the radial position where the extra component of the plasma has highest density and thus determines the overall size of the plasma cloud. Therefore, it has a great influence on the reduction of the brightness compared to the empty shot. On the other hand, r_{hot} allows the formation of a steeper density gradient at the edge of the plasma which results in a change of the steepness of the corona. In summary, the coarse choice for r_{hot} is mainly made from the simulated darkening in comparison with experimental data after the spatial position of the plasma has been determined. The exact choice is made from the slope of the outer corona in combination with n_{hot} and l_{hot}.

Heigth of moving Gaussian $\mathbf{n_{hot}}$: The peak height of the moving Gaussian distribution is determined by the choice of the parameter n_{hot}. In transmission, this is an essential component since it can influence the overcritical volume of the plasma. Thereby n_{hot} provides the possibility to generate a larger overcritical region than it would be possible for the single Gaussian distribution due to the particle number conservation. This enlargement mainly influences the central beam profile and the percent obscuration which therefore serves as a first crude selection criterion for this parameter. In addition, n_{hot} also influences the height and, consequently, the slope of the corona, but the effect of n_{hot} is smaller than corresponding changes of the parameters r_{hot} and l_{hot}. However, this can be used in comparison with experimental data to define n_{hot} even more precisely.

Width of moving Gaussian $\mathbf{l_{hot}}$: The width of the shiftable Gaussian distribution, determined by l_{hot}, influences the density gradient at the edge of the plasma to a large extent. This is mainly reflected in the slope of the corona. A narrow distribution causes a steeper increase and a broadening of the Gaussian leads to a flattening of the corona fraction. In both cases the height of the corona increases or decreases accordingly.

Width of central Gaussian $\mathbf{l_{cold}}$: The last parameter of the density distribution to be determined is the width of the central Gaussian which is given by l_{cold}. This parameter has an influence on the resulting beam profile only if the radial expansion of the inner distribution contributes to the density profile at the edge of the plasma or if the moving Gaussian is entirely undercritical. This can be explained by the overcritical decentralized Gaussian distribution forming an impenetrable shell for the laser and thus shielding any influence of the central distribution as long as it does not contribute outside the shell. However, if this is the case, the choice of l_{cold} affects the beam profile in the same way as l_{hot}, since it causes a change in the density gradient at the edge of the distribution.

Closing remarks: As it becomes clear from the description of the selection criteria for the individual parameters, the parameters (with the exception of the position of the distribution) cannot be considered independently of one another. However, distinct patterns that limit the parameter space in a certain way can be identified based on observations in the experimental data. Profiles that show a strong darkening of the transmitted light display a steeper, more pronounced corona. This can be reproduced in the transmission simulation by choosing a combination of larger radius r_{hot} and a steeper density gradient, i.e. smaller l_{hot}. Furthermore, it is observed that a contribution of the central Gaussian component at the edge of the plasma is often necessary for the best agreement. This results in a certain lower limit for the choice of l_{cold} via the position of the decentralized Gaussian r_{hot}. Due to the choice of l_{cold}, r_{hot} and l_{hot}, n_{hot} is often subject to an upper limit given by particle number conservation (and $n_e > 0$ everywhere) and in many cases must be above the critical density in order to obtain a sufficiently large overcritical volume to achieve the experimentally measured darkening in the simulation.

Quantification of best-fit and error margins for pump analysis

Following the qualitative description, an attempt is made to quantify the agreement and thus to create a basis for an error analysis. The metric to be investigated for the determination of the plasma density distribution parameters is the agreement between the experimental and simulated transmission images. It is therefore useful to express this correlation in numbers. For this purpose, the simulated image is first interpolated to obtain the same resolution and number of pixels as dictated by the experimental data. Then the difference between the two is calculated, squaring the deviation for each individual pixel and summing it up to a value D_{diff} for the entire image:

$$D_{diff} = \sum_{i=0}^{n} \sum_{j=0}^{m} (E_{i,j} - S_{i,j})^2 \tag{4.23}$$

where E and S represent the experimental and simulated transmission image with n times m pixel. If both images were perfectly similar, this would result in a value of $D_{diff} = 0$. The best fit with experimental data is achieved for the parameter set that yields the smallest value D_{diff}.

This calculation is performed exemplarily for the pump transmission simulations of the different density models described in the previous section to prove that the qualitatively best agreement for the dual Gaussian model is reflected in the explicit calculation of D_{diff}. Without a target (empty shot), the simulation does not perfectly match the observed pattern and results in a value of $D_{diff} = 230$. Compared with the quadratic sum over the experimental image ($D_{tot,exp} = 13454$), this represents an deviation of 1.7 %. The calculation for the simulation with plasma results in $D_{diff} = 767$ for the exponential distribution, $D_{diff} = 718$ for the single Gaussian distribution and $D_{diff} = 664$ for the dual Gaussian distribution with moving component. With $D_{tot,exp} = 6454$, this yields corresponding deviations of 12 %, 11 % and 10 %, which confirms the best agreement already qualitatively established for the latter model. This becomes even more evident when considering the data set presented in figure 4.26. The patterns reproduced with the exponential and simple Gaussian models differ from the experimental results by 50% and 44%, respectively. The deviation significantly decreases (31%) when the dual Gaussian model is used.

As the best fit has been determined for each transmission image by minimizing D_{diff}, an error tolerance of the individual parameters can then be specified. Starting from the parameter set with minimum D_{diff}, each parameter is changed step by step while the other parameters are kept constant (n_{cold} adjusts according to equation 4.18 and r_{cold} is adapted if necessary) and the respective value of D_{diff} is calculated. The corresponding error interval for the individual parameter subsequently includes all values of this parameter for which the simulation results in a D_{diff} that deviates less than 1 % from the minimum D_{diff}.

Selection criteria for best-fit parameter set of probe simulation

The decisive criteria for the choice of parameters which best resemble the experimental probe images are again illustrated on the basis of the profiles of an exemplary shot shown in figure 4.29. One criterion are the radial positions of the individual peaks, which change with the density distribution. However, it should be noted that due to the partly poor signal-to-noise ratio, not all peaks can always be clearly identified. Stronger filtering was avoided in order to prevent the generation of artifacts. A more stable selection criterion is the height of the individual peaks, whereby especially the relative height to each other is to be considered since this is less susceptible to influences of the applied filters.

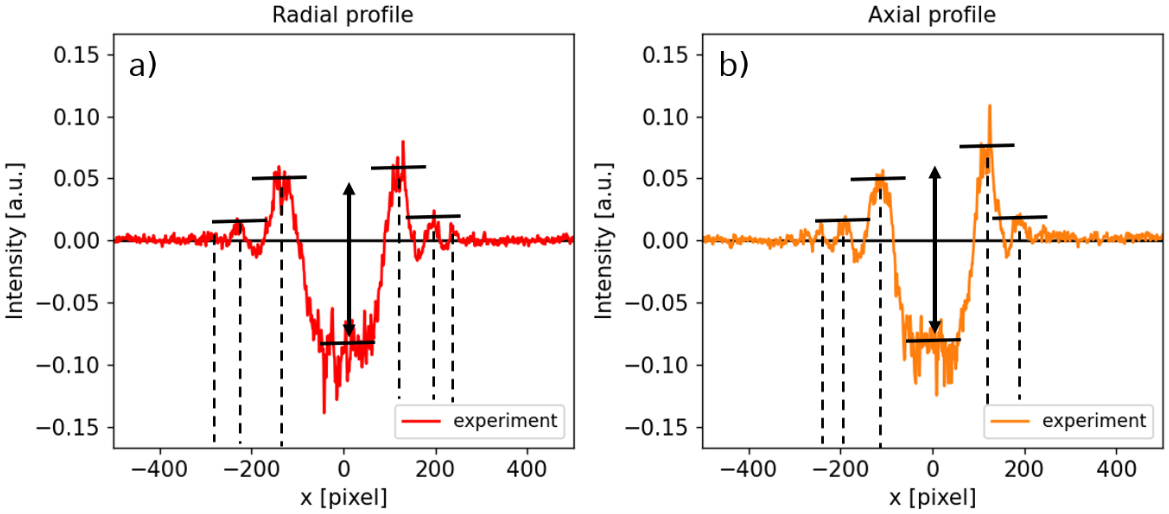

Figure 4.29: Profiles of exemplary probe image indicating relevant features for choice of density distribution parameters: absolute (black bars) and relative (arrow) height of identifiable interference maxima and position of individual maxima (dashed lines).

Displacement of simulated sphere (x,y): A shift of the density distribution with respect to the beam axis of the probe is expressed purely by a global change of the peak heights. This can be explained by the Gaussian intensity envelope of the probe. A decentralized illumination of the density distribution manifests itself by a shift of the enveloping intensity distribution, while the position of the peaks does change. The correct value of the shift in both dimensions can be obtained by comparing the peak heights right and left of the center in the respective profiles.

For all following parameters, a subdivision into three temporal ranges is made since the simulated models change depending on the time of the acquired probe image relative to the interaction (t = 0 ps):

t < 0 ps

This section contains all data recorded at times before the interaction of pump pulses and target. These include two sets of data: probe-only shots, recorded for each target and all shots with both, pump and probe, where the probe had a negative delay setting. The density model describes the initial target with a diameter of 1 μm and a refractive index of 1.577. Here, a comparison of simulation and experiment is used to check whether the measured transmission image corresponds to a sphere with a diameter of 1 μm. The radius of the initial sphere r_0 is the only variable parameter for all shots in this time window. It becomes evident that the most significant change with variation of r_0 in the simulation occurs in the ratio of the peak heights between zero and first maximum. The radial position of the individual peaks also changes slightly, but the change in peak heights provides the more pronounced and thus more stable criterion.

0 ps $\leq$ t $\leq$ 39 ps

In the time interval from 0 ps to 39 ps, all density distributions were simulated using the moving dual Gaussian distribution model. In this time domain, the peak positions of observed diffraction patterns cannot be reconstructed with a single Gaussian distribution. The same parameters as previously found in the best-fit of the associated transmission image were used for data sets at time t = 0 ps. For all data sets at later times, the determined parameter set of the pump provides a lower limit in the choice of parameters.

Width of central Gaussian $\mathbf{l_{cold}}$: The width of the central Gaussian distribution determines the basic shape of the diffraction pattern. It mainly influences the relative peak heights and the number of recognizable peaks. Therefore, a selection of l_{cold} is based on achieving a coarse agreement with the observed diffraction pattern. Deviations, e.g. of the peak positions, can be compensated afterwards by choosing the moving Gaussian parameters.

Position of moving Gaussian $\mathbf{r_{hot}}$: In the simulation, an increase of r_{hot} primarily causes a shift of the radial position of the first maxima (and thus also of all following maxima) to the outside. In addition, r_{hot} strongly influences the intensity profile in the center of the diffraction pattern.

Width of moving Gaussian $\mathbf{l_{hot}}$: The change of the modulation in the diffraction pattern is the main influence of the width of the moving Gaussian component. It can be observed that l_{hot} influences the peak heights and can cause asymmetric peak shapes in some cases.

Heigth of moving Gaussian $\mathbf{n_{hot}}$: n_{hot} determines how much the influences, previously defined for r_{hot} and l_{hot}, affect the final result of the simulation. A reduction of n_{hot} minimizes their input accordingly since the function approaches more and more the single Gaussian distribution.

t > 39 ps

Except for one shot, all diffraction images could be satisfactorily reproduced by the single Gaussian distribution, with its width l_{cold} being the only free parameter. A change of l_{cold} manifests itself in the simulation in the position of the peaks, their recognizable number and especially in a change of the central intensity distribution. An initially existing maximum changes into a minimum for increasing values of l_{cold}. More general, it can be seen that with increasing l_{cold} the number of peaks and their respective heights decreases and at the same time the depth of the central profile increases.

Quantification of best-fit and error margins for probe analysis

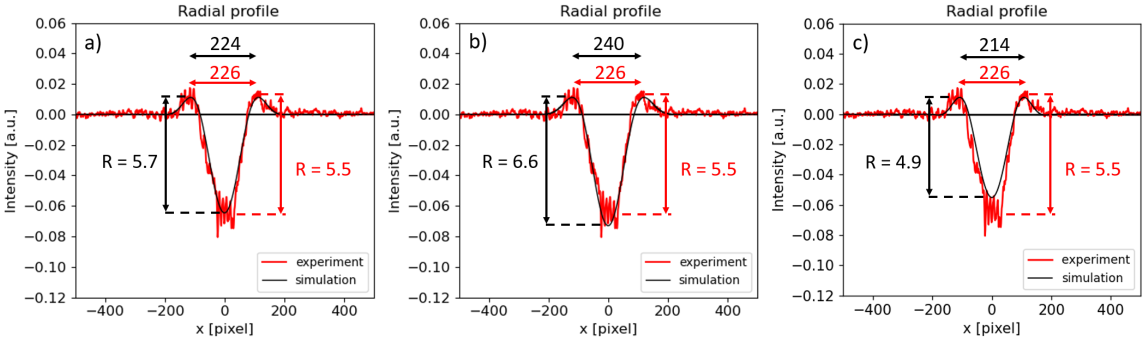

Figure 4.30: Profile of exemplary probe image (red curve) compared to profiles of simulation results (black curve): a) shows a best-fit parameter set that matches the experimental results in peak position an relative peak heights R, while b) and c) show simulation results that differ from experimental quantities by more than 10 %.

Similar to the pump, the method of calculating the sum of squared differences as a quantification of agreement between experimental and simulation results was tested for the probe. Due to the partially high noise-level and occuring asymmetries, this method could not successfully be applied here. Hence, agreement between experimentally recorded images and reproduced simulation results was verified manually. For this purpose, quantities such as peak positions and relative peak heights were extracted from the experimental results and compared to the simulations. The best-fit parameter set is defined as the one which achieves highest overlap with the experimental quantities as exemplified by figure 4.30 a). The error margins of the parameter set are determined by varying the parameters until the simulation result differs by more than 10 % in one of the experimental quantities. Such a deviation from the best fit in both directions is illustrated by figure 4.30 b) and c). If more than one parameter is required in the simulation (dual Gaussian), this method is applied for each parameter individually while all other parameters are kept at their best-fit value.

Chapter 5

Analysis and Evaluation

Contents

5.1 Selection of Evaluable Data 99

5.2 Pump 102

  5.2.1 Position in Focal Plane 103

  5.2.2 Density Distribution 104

5.3 Probe 107

  5.3.1 Negative Delay (t < 0 ps) 107

  5.3.2 Zero Delay (t = 0 ps) 109

  5.3.3 Positive Delay (t > 0 ps) 110

5.4 Discussion 112

In this chapter, the results for the density distributions in the plasma found by comparing simulation and experiment are presented. Subsequently, an expansion model is introduced which allows to describe the time course of the density distribution and from which properties of the expansion and influences of the laser can be derived.

5.1 Selection of Evaluable Data

After completion of the final experimental setup, a total number of 37 shots with levitating spheres could be recorded in three successive campaigns. The limiting factor in terms of the number of available data sets was the trapping process and the positioning of the targets via the Paul trap as well as the long-term stability of the laser. It was found that the performance of the Paul trap degraded with increasing number of shots, potentially due to parts of the trap becoming statically charged and disturbing the fields used to damp the particles. In addition, as the experiment progressed, the stability of the laser deteriorated, making an overlap of particle and focus increasingly difficult. This effect could be reduced by implementing a partial automation of the laser, however, not completely eliminated. In total, recording the data required around 18 hours.

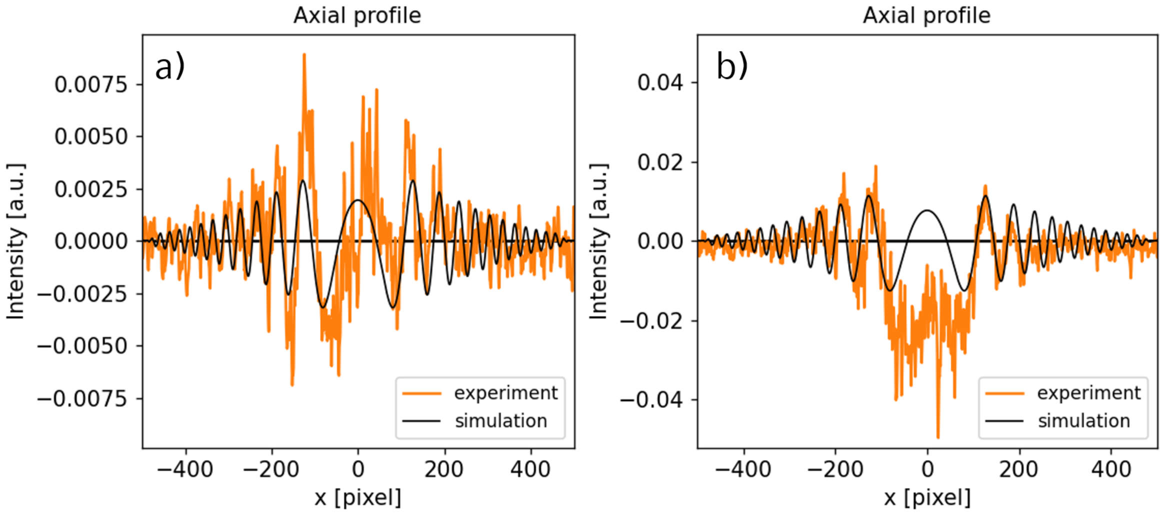

Figure 5.1: Axial profile of single sphere (a)) and cluster (b)) compared to simulation of 1 μm non-ionized plastic sphere.

To ensure that only shots with the same initial target conditions are evaluated, in a first step it was analyzed which of the irradiated targets were indeed single 1 μm spheres and which were clusters of clumping particles. For this purpose, the diffraction images acquired for each shot with the probe-only setting were compared to simulations of an non-ionized 1 μm plastic sphere. This comparison is shown in figure 5.1, where the experimentally obtained axial profile of a single sphere (a)) and a cluster (b)) are considered. The black curve corresponds in each case to the axial profile of the diffraction pattern obtained by simulation of a 1 μm sphere with a refractive index of $\eta = 1.577$. A distinct difference in the modulation of the diffraction pattern can be seen, especially in the center of the distribution. In the case of clusters, the central peak drops significantly. This behavior can be qualitatively reconstructed in the simulation by increasing the initial radius r_0 of the plastic sphere. This results in a clear criterion for the distinction of both cases. It was determined that 29 targets were single spheres while eight targets were clusters. This corresponds to a cluster rate of just over 20 %. An analysis of the cluster data was not performed, because an evaluation of the probe data can only determine that a cluster is present, but it is not possible to reconstruct how many individual spheres form the cluster. Thus, no conditions can be set for the electron particle number, which is the determining factor for the calculation of the density distribution to be simulated. An overview of all 29 evaluated data sets with the experimentally extracted quantities of transmission (in percent, compared to the transmission of the corresponding empty shot) and the temporal delay of the corresponding probe image are shown in table 5.1.

Shot number	Delay [ps]	Transm. [%]	Shot number	Delay [ps]	Transm. [%]
008_2209	- 14	82	013_2209	79	95
006_2209	- 3	101	014_2209	79	81
007_2209	- 3	91	015_2209	79	35
002_2209	0	73	004_0110	126	77
003_2209	0	105	003_0110	193	52
004_2209	0	59	016_2209	193	42
004_2509	1	64	002_0110	226	61
001_2509	3	102	017_2209	259	102
002_2509	3	100	001_0110	593	69
003_2509	3	39	007_2509	593	94
005_0110	39	103	005_2509	593	99
007_0110	39	40	006_2509	593	101
001_2209	60	62	009_2509	593	102
011_2209	79	103	010_2509	593	99
012_2209	79	99			

Table 5.1: List of all evaluated shots with shotnumber, probe delay and transmission value (compared to empty shot).

5.2 Pump

The evaluation of the pump transmission data provides the starting conditions for the following expansion of each sphere. Depending on the position in the laser focus, each target is irradiated with a different peak intensity, resulting in differences in the maximum absorbable energy and temporal evolution of ionization and expansion that may occur in the rising edge of the laser intensity during t < 0 ps. This is especially important for the later analysis of the time course of the expansion where only data sets that had identical or similar initial conditions can be compared. In addition, it is also possible to assign different expansion behaviors to particular laser intensities and thus to deduce the influence of the laser peak intensity and related parameters of the interaction.

Before presenting the relevant parameters extracted from the simulation, it should be noted that a successfull reconstruction is only possible for data sets with an obscuration of more than 5% in the transmission image. For all other data sets no parameter set for position and density distribution can be found for which D_{diff} assumes a unique minimum value. For this reason, these shots are excluded, since no conclusions about the expansion behavior can be derived due to the missing initial conditions. This reduces the number of shots that can be evaluated to 16. In all these cases, neither the simulation of a non-ionized sphere nor a fully ionized sphere with 1 μm diameter could describe the transmission profiles observed experimentally. This indicates that all targets have already undergone a certain expansion at the arrival of the maximum intensity at time t $= 0$ ps. This can be expected by inspecting the temporal intensity profile (see figure 5.2). Based on the mechanisms described in section 2.3 such as MPI and tunnel ionization, the laser can create a plasma considerably prior to reaching its peak intensity. The resulting heating immediately starts the expansion of this plasma into the surrounding vacuum. Since the image of the transmission is mostly generated by the fs-short, high-intensity part of the laser intensity which reaches the target (per definition) at t $= 0$ ps, this pre-expansion is included in the transmission data. The exact time of plasma creation and hence the start of expansion depends on a threshold intensity that is difficult to predict. Based on various measurements with polystyrene, a crude range of $\sim\ 10^{12} - 10^{13}\, W/cm^2$ can be estimated from the literature ([110, 111, 112]). Thus, for a centrally hit particle, the laser would be able to ionize the particle and initiate expansion already 1.5 to 1 ps before the interaction at peak intensity.

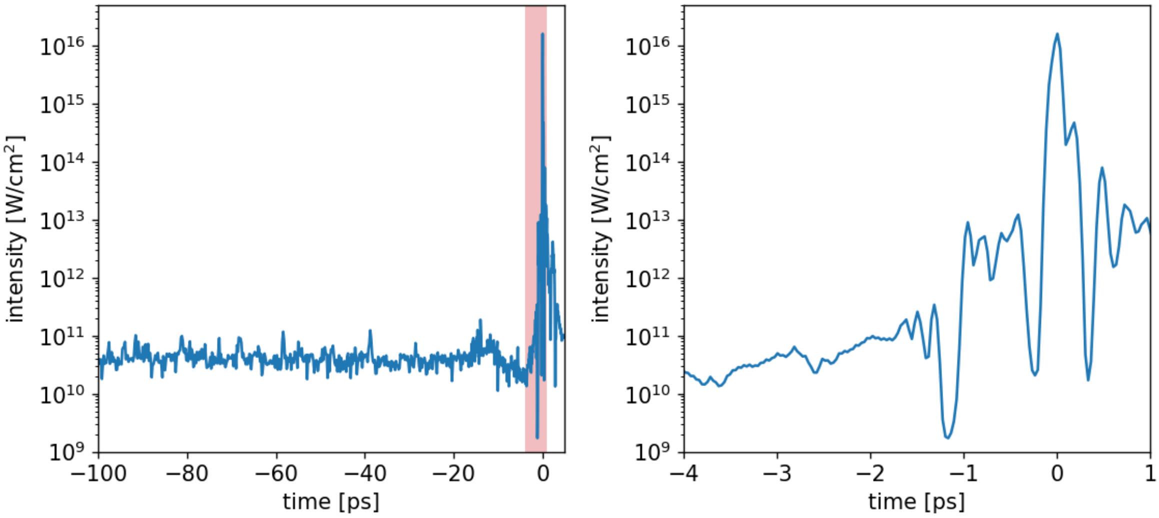

Figure 5.2: Two cutouts of the temporal intensity distribution scaled to the peak intensity of $1.6 \cdot 10^{16}\, W/cm^2$: from -100 ps to 5 ps on the left and from -5 ps to 1 ps on the right.

5.2.1 Position in Focal Plane

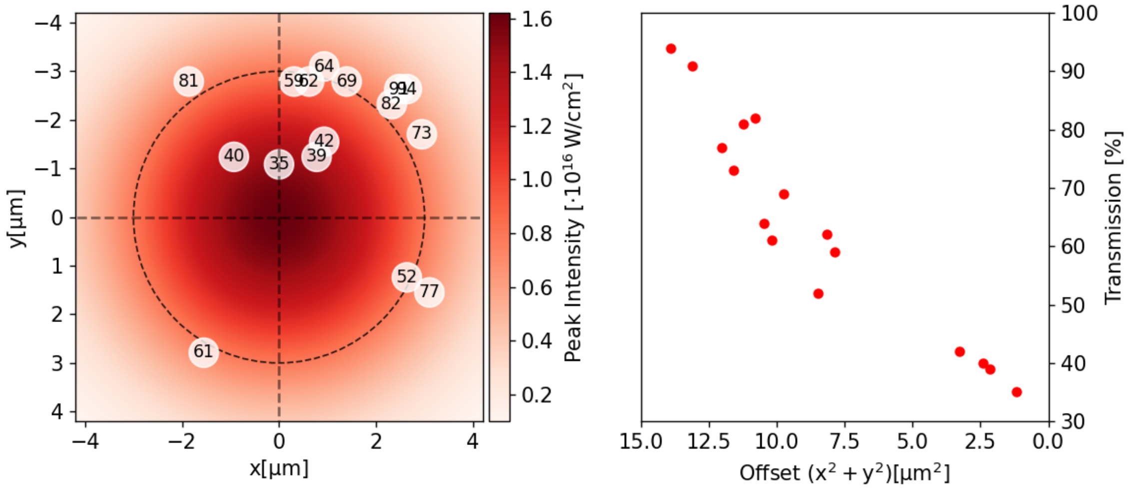

Figure 5.3: Left: Position of each evaluated sphere with correlated transmission (compared to empty shot) in an Gaussian equivalent focus with 6 μm FWHM. Right: Experimentally obtained transmission versus reconstructed quadratic offset.

The determination of the displacement of each particle perpendicular to the laser axis is based on the procedure described in section 4.4. The respective reconstructed position of each of these 16 spheres in the laser focus is shown in figure 5.3. Since the experimentally obtained high-dynamic-range image of the focus is only a temporal snapshot and no exact intensity distribution can be measured at the time of interaction, the distribution shown here corresponds to the Gaussian equivalent of the real focus, adjusted to assume the same FWHM and peak intensity as determined for the real focus. The position of each target is marked by the white circles and labeled for each shot with the corresponding percent transmission compared to the empty shot. Already here it can be seen that spheres which are closer to the focus center cause lower transmission than those which are more displaced from the center. This becomes even clearer when the transmission of each particle is plotted against the quadratic offset from the laser axis $x^2 + y^2$. Thereby, an almost linear relationship between both quantities is observed which is a hint that the size of the particle (plasma) at t = 0 ps also depends on the initial position.

5.2.2 Density Distribution

The sole displacement of the particles is not capabale of describing the change in transmission (as one would expect a logarithmic scaling of transmission with displacement and not a linear one). The additional contribution of plasma expansion **before** t = 0 ps becomes clear if one also looks at the corresponding reconstructed density profile for each initial offset position. In figure 5.4 the individual parameters of the dual Gaussian distribution are plotted versus the offset $x^2 + y^2$ for each shot. As a reminder for the reader: l_{cold} describes the width of the central Gaussian, the corresponding values for the plateau region r_{cold} and the amplitude n_{cold} result from the particle number conservation. r_{hot} describes the position of the additional, moving Gaussian distribution, the amplitude and width of which are determined by n_{hot} and l_{hot}, respectively. The error bars of the individual parameters were determined by the procedure described in section 4.4.

In general, particles which were hit more centrally show greater pre-expansion. This is consistent with the fact that these particles are exposed to a higher peak intensity and hence the threshold of plasma formation is reached earlier in time. A closer look at the individual parameters reveals the following observations: The width of the central Gaussian increases linearly with decreasing offset $x^2 + y^2$ from the center, leading to greater expansion. Concerning the moving component of the distribution, the closer the particle is to the laser axis, the further out its peak position is, the narrower the width of the Gaussian, and the lower its amplitude. But in all cases the moving Gaussian density reaches above the critical density. Looking at the error bars, the uncertainty becomes larger for smaller overlap between target and laser. This is not surprising since on the one hand these plasmas are smaller and on the other hand they interact only with a region of lower laser intensity, which strongly reduces their influence on the final transmission profile and thus makes a clear definition of the parameters within the described method more difficult.

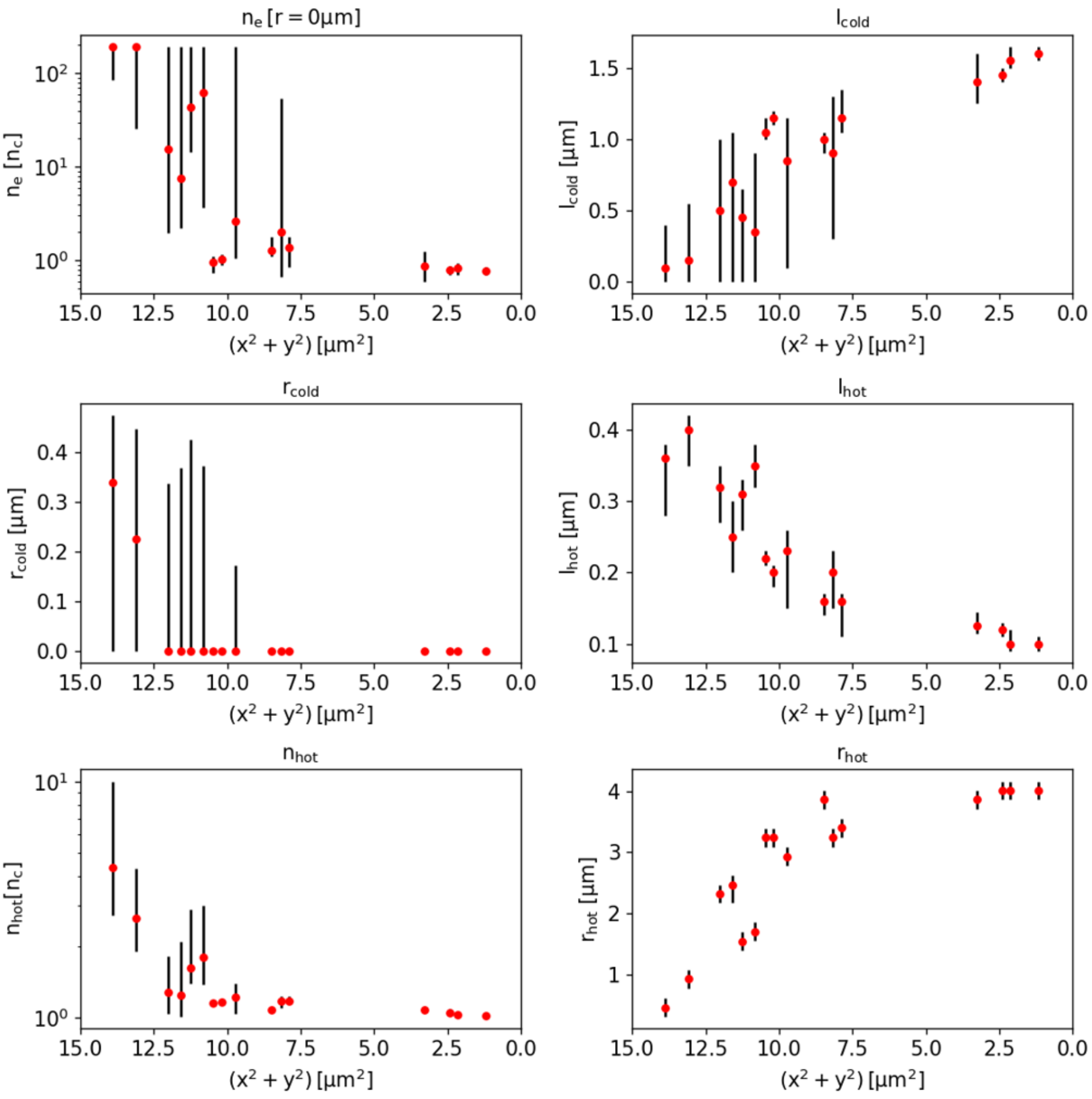

Figure 5.4: Parameters of density distribution function extracted from comparison of simulation and experimental results of transmission diagnostic.

The overall distributions, exemplarily shown in figure 5.5 for three different offsets, further illustrates the observed behaviour: if the particle and the laser are only slightly overlapping (13.1 μm^2), the density distribution is plateau-like and drops of steeply at the edge. In comparison to the central distribution, the additional density component is hardly perceptible. It is also rather broad and located close to the center. If the particle is closer to the laser axis (9.7 μm^2), the density in the center falls far below the original value of 194 n_c. The course follows a broad Gaussian distribution and the moving component is clearly visible at its edge. For data sets showing the strongest overlap with the laser focus (1.2 μm^2), the highest density seems to be located in the moving component with the central part indicating an already undercritical plasma. With respect to the central distribution in all three scenarios, it must be noted that this is not a direct measurement since this part is shielded from the laser by the shell formed by the overcritical shock (indicated by the grey areas in figure 5.5). It is possible that especially in the last case, the broad Gaussian distribution yields the best reconstruction because it provides additional density components outside the shock, as seen in the comparison with the RALEF simulations (see figure 4.27). Since the density at r = 0 μm results from the choice of the simulation parameters, this may result in a too low central density. In the interior, there may still be overcritical regions which cannot be reconstructed by the simple density model used in this work.

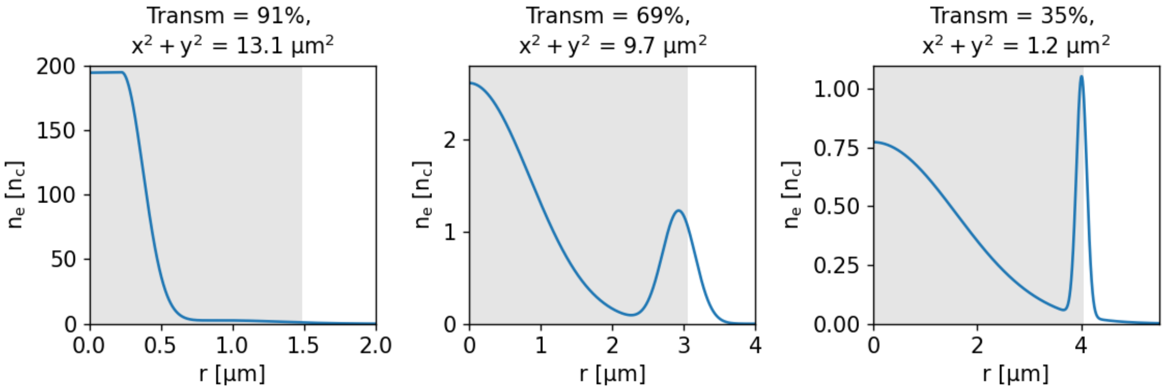

Figure 5.5: Three exemplary density distributions reconstructed for different offsets and transmission values. The grey areas mark the region of density that cannot be directly observed by the laser.

More features can be revealed by analyzing the offset-dependence of the radius of the critical density r_{nc} and the limiting radius of the distribution r_{targ}. r_{nc} is important in transmission mostly because it defines the area in the focus which is impenetrable for the laser and thus is primarily responsible for the reduction of the transmission. r_{targ}, which is defined by the truncation condition from subsection 4.1.3 (99.99% of all particles of the distribution within r_{targ}) indicates the course of lower densities.

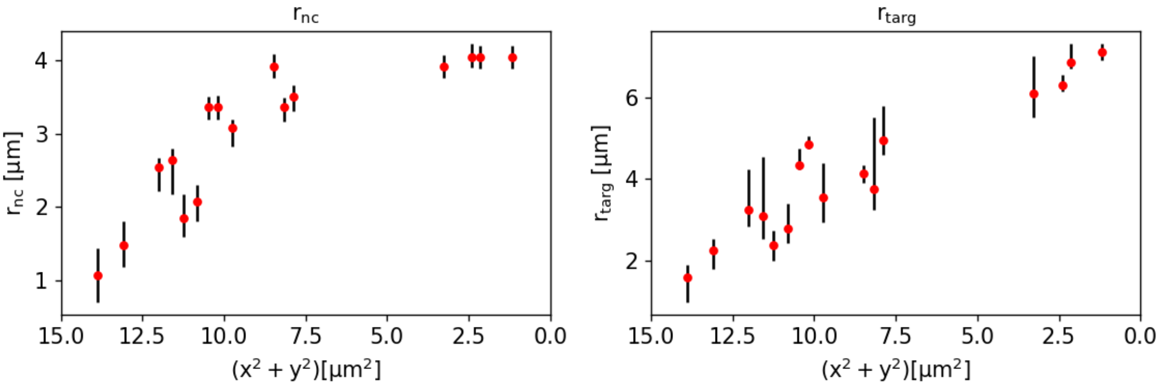

Figure 5.6: Offset-dependency of radius of critical density r_{nc} and limiting radius of transmission simulations r_{targ}.

In figure 5.6 both parameters are plotted against the offset $x^2 + y^2$. A comparison with figure 5.4 shows that the radius of the critical density follows in its behavior almost exactly the course of r_{hot}. The limiting radius r_{targ}, however, is mainly determined by the width of the central Gaussian distribution l_{cold}. This also explains why a simple Gaussian distribution, especially in the case of small offsets to the laser axis, is not able to reconstruct the observed transmission images. The additional Gaussian component provides the necessary increase of the critical density area in these cases.

5.3 Probe

After the starting conditions for each target could be determined by the analysis of the transmission, one can now investigate the temporal progress of the expansion. In the following, a distinction is made between three cases: data with negative delay, where the probe examines the particle before the arrival of the pump, data with zero delay, where pump and probe interact with the plasma at the same time and data with positive delay, where the probe investigates the plasma at a defined time after the interaction with the pump.

5.3.1 Negative Delay (t < 0 ps)

As shown in the transmission analysis, all shots feature some pre-expansion at t = 0 ps that depends on the particle offset with respect to the laser axis. Shots with negative delay can thus be used to define a temporal range for the onset of ionization. The two shots available in this regime have a delay setting of t = -14 ps and t = -3 ps. The offset of both targets to the laser axis can be determined from the transmission analysis to 10.8 μm^2 and 13.1 μm^2, respectively.

In comparison with the simulation, both shots show diffraction patterns which correspond to those of an initial plastic sphere with 1 μm diameter in the simulation. In figure 5.7, a) shows the experimental axial profile for -14 ps delay and b) the one for -3 ps. The solid black curve corresponds in each case to the results of the simulation using a initial sphere with refractive index 1.577. The black dashed curves are simulation results for a fully ionized 1 μm-sphere with a core density of 194 n_c, showing clear deviations from the experimental data.

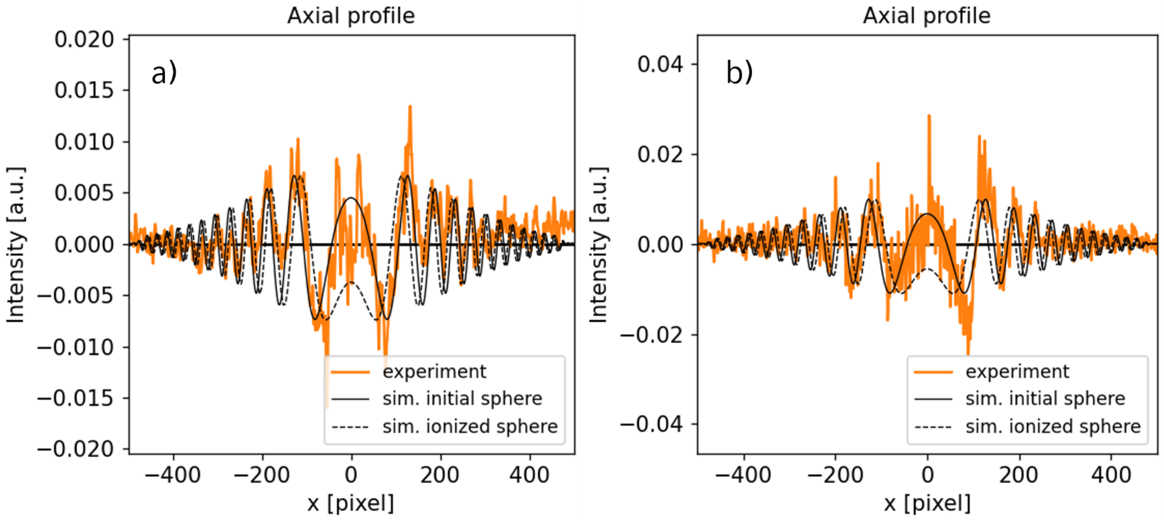

Figure 5.7: Axial profiles of two probe images with negative delay, where a) displays the data taken at -14 ps and b) the data taken at -3 ps. In both cases, the solid black curve corresponds to the simulation result when simulating an initial plastic sphere of 1 μm diameter while the dashed black curve represents a fully ionized sphere with the same diameter.

Since the simulation only distinguishes between the two cases of constant purely real (initial sphere) and constant purely imaginary refractive index (ionized sphere), the sole case to be excluded is that a overcritical plasma is already present at the times investigated. Further potential changes of the target, which are not or only to a small extent reflected in a change of the refractive index, cannot be investigated here. Nevertheless, the results restrict the starting time of the expansion. With regard to preceding light in the ns-regime, it can be stated that this does not cause any measurable changes on the target (in contrast to the initial RALEF simulations, starting at t = -1.8 ns). This statement is valid despite the comparatively large distance to the laser axis (and therefore intensity of few times $10^{15}\,W/cm^2$ instead of $10^{16}\,W/cm^2$) because this part of the intensity distribution generally does not follow the same spatial distribution in the focal plane as the fs-short, high-intensity pulse. Especially ASE, which is generated in the used multipass amplifiers and is not reduced by Pockels cells, does not pass the laser chain collimated and therefore has a much worse focusability resulting in a broader spatial distribution in the focal plane. Also, the pre-pulse at t = -584 ps (see figure 3.14) has no measurable influence on the particle, although it should be noted that its peak intensity is reduced by a factor of about 2.4 (for the measurement at -14 ps) and 2.8 (for the measurement at -3 ps) by the offset of the target to the laser axis. However, looking at the parameter set obtained from the transmission analysis, there is no sudden jump in the plasma sizes for shrinking offsets, which suggests that this pre-pulse does not trigger a premature expansion even with a better overlap between target and laser. As the offset between target and focus is known, the temporal intensity distribution of figure 3.14 can be scaled towards the position-dependend peak intensity from figure 5.3. Both shots do not indicate ionization, thus the highest intensity up to the respective point in time, where the data was taken, can be used to confine the lower limit for the plasma formation threshold. In each case, this value is given by the prepulse and yields $1.5 - 2 \cdot 10^{11}\,W/cm^2$. Considering the above statement about the constant parameter increase for smaller offsets, this value could be extended towards $5 \cdot 10^{11}\,W/cm^2$. The upper limit is given by the intensity for barrier suppression ionization: for the first ionization energy of polystyrene of $E_{ion} = 8.46\,eV$ [113] and using equations 2.22 and 2.7, this yields an intensity of $2 \cdot 10^{13}\,W/cm^2$. Hence the intensity range for plasma generation onset is expected to be $5 \cdot 10^{11} - 2 \cdot 10^{13}\,W/cm^2$, which is in line with the above mentioned literature.

5.3.2 Zero Delay (t = 0 ps)

Probe measurements with zero delay can be used to validate the selected density model and to verify the diagnostics. Since both pulses interact with the same plasma at the time t = 0 ps (though in directions perpendicular to each other), only one spherically symmetric model results in a single parameter set of the distribution with which experimental results of both diagnostics can be reconstructed. This could already be shown in section 4.2 for a target with an offset of 11.6 μm^2. Similarly, for another shot with an offset of 7.9 μm^2, the parameters found in the transmission analysis were used for the simulation of the probe image. The comparison between experiment and simulation is shown in figure 5.8. The axial and radial profile of the diffraction patterns are in good agreement, which again confirms the choice of the model.

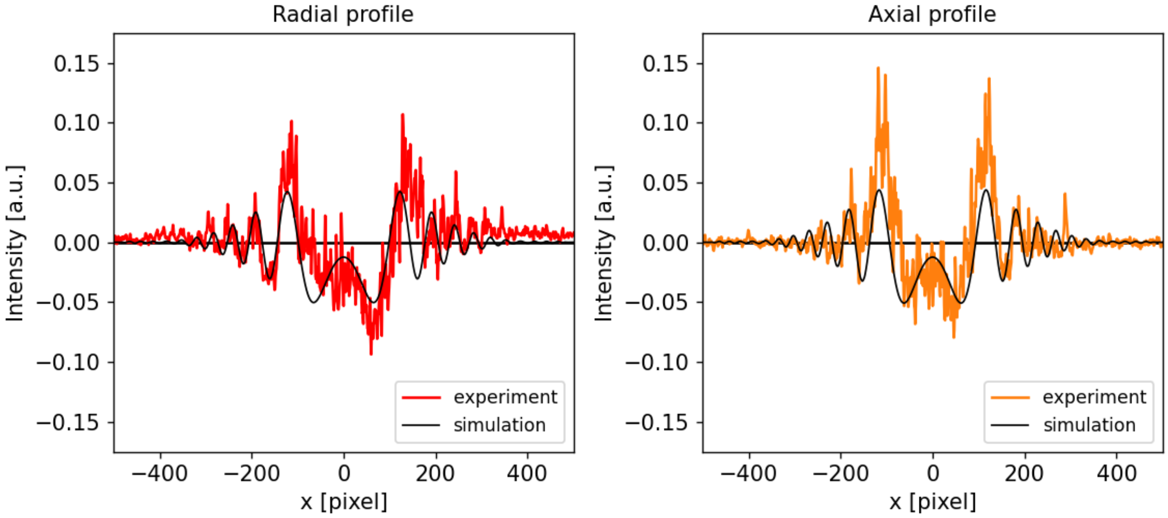

Figure 5.8: Radial and axial profile of probe image with zero delay, the black curve corresponds to the simulation results obtained by using the same density distribution as for the corresponding transmission simulation.

Moreover, the agreement between transmission and probe reinforces the suitability of the transmission as a plasma diagnostic in its own right. Knowledge about the density distribution, gained from the transmission, can not only be used to group shots of similar experimental conditions but can serve directly as a measurement of the plasma during the interaction with the pump pulse. This finding is especially valuable for other experimental setups where no probe pulse is available to measure the plasma conditions or emission/scattering of the plasma into the probe diagnostics is too strong.

5.3.3 Positive Delay ($t > 0$ ps)

The temporal evolution of the plasma expansion is studied by probe data with positive delay. In the experiment, the density distribution was investigated over a time span of almost 600 ps. Due to the experimental setup, in contrast to the transmission one of the two observed dimensions in the probe is aligned along the laser axis. As a result, asymmetries can occur between both axes in the course of the expansion, which cannot be reproduced by the simple, spherically symmetric density model. In order to keep the number of used parameters small and the model simple, the distribution in these cases is determined seperately along the axial and radial direction as described in section 4.4. It can be shown that this method provides good results for small delays up to about 40 ps and large delays above 100 ps. In the intermediate range, strong asymmetries develope even within the two directions, preventing a reasonable reconstruction via the simple density model. In these cases, the density distribution cannot be determined quantitatively.

For the reconstruction of the diffraction patterns at late times (t > 100 ps), a density distribution in the form of a simple Gaussian distribution is sufficient (except for one shot). This is in agreement with observations in the hydrodynamics simulation discussed in section 4.3. An overview of the reconstructed density distributions together with the determined offset from the central laser axis is listed in table 5.2. The error margins are obtained according to the method described in section 4.4.

Delay [ps]	Offset [μm^2]	l_{cold} [μm]	n_{hot} [n_c]	r_{hot} [μm]	l_{hot} [μm]
1	10.5	$1.35^{+0.3}_{-0.3}$	$0.25^{+0.05}_{-0.10}$	$4.8^{+0.45}_{-0.45}$	$0.4^{+0.10}_{-0.15}$
3	2.1	$2.4^{+0.6}_{-0.4}$	$0.1^{+0.05}_{-0.05}$	$7.8^{+0.75}_{-0.60}$	$0.25^{+0.15}_{-0.15}$
39	2.4	$5.0^{+0.5}_{-0.5}$	-	-	-
		$9.0^{+1.5}_{-1.5}$	$0.0015^{+0.0010}_{-0.0010}$	$17.0^{+2.0}_{-2.0}$	$3.0^{+1.0}_{-1.0}$
126	12.0	$7.0^{+0.5}_{-0.5}$	-	-	-
193	8.5	$11.5^{+1.0}_{-1.0}$	-	-	-
193	3.3	$16.0^{+2.0}_{-2.0}$	$0.0005^{+0.0002}_{-0.0002}$	$19.0^{+1.5}_{-1.5}$	$4.0^{+1.0}_{-1.5}$
226	10.2	$11.0^{+1.0}_{-1.0}$	-	-	-
		$14.0^{+1.5}_{-1.0}$			
593	9.7	$20.0^{+2.0}_{-2.0}$	-	-	-
593	13.9	$12.0^{+1.5}_{-1.0}$	-	-	-

Table 5.2: Parameters of reconstructed density profiles (t > 0 ps) with corresponding probe delay and offset from the laser axis.

When comparing the parameters of the expansion at early times (t = 1 ps and t = 3 ps) with the values determined from the transmission, already an onset of smearing of the shock-like component and the transition to the simplified distribution is observed. For the distribution at t = 1 ps, the width l_{hot} nearly doubles from 0.22 μm to 0.4 μm while the amplitude n_{hot} decreases by more than a factor of 4 from 1.15 n_c to 0.25 n_c. This behavior is even more pronounced for the distribution at t = 3 ps. Here, the width l_{hot} of 0.25 μm is more than twice as large than at the time of the transmission measurement and the amplitude drops by an order of magnitude from 1.03 n_c to only 0.1 n_c. Another interesting aspect is that data sets, obtained at the same points in time (193 ps respectively 593 ps), show significant deviations in terms of plasma size. Thereby it shows that particles with smaller offset have already expanded further at the same time, which is expected. In order to make meaningful statements about the time course of the expansion, only data with similar offsets may thus be compared. In summary, it can be seen that regardless of the offset, the width of the distribution function increases, indicating a progressive plasma expansion over the observed period of time.

5.4 Discussion

Now that the relevant parameters of laser-triggered plasma expansion have been described, an attempt can be made to model the behavior of the plasma. As already introduced in section 2.6, two simplified models can be used for this purpose: the hydrodynamic expansion and the Coulomb explosion. It is first interesting to discuss which of the two regimes represents the measured expansion best: recalling equation 2.48, the hydrodynamic pressure generated by the hot electrons p_e is

$$p_e = n_e \cdot k_B \cdot T_e. \tag{5.1}$$

As this pressure depends on n_e, p_e scales with r^{-3}. The Coulomb pressure due to charge separation is calculated as

$$p_{coulomb} = \frac{Q^2 \cdot e^2 \cdot k_e}{8 \cdot \pi \cdot r_{initial}^4}. \tag{5.2}$$

Assuming a fully ionized, 1 μm sphere with an electron density of $3.4 \cdot 10^{23}\, cm^{-3}$ and an electron temperatur of 1 keV, up to 10^9 electrons would have to leave the plasma in order for $p_{coulomb}$ to be on the order of p_e. Although this is only a percent of the total number of electrons, one needs to keep in mind the space charge fields the electrons would have to overcome to reach that level of depletion. For an electron on the sphere surface (r = 0.5 μm) this would result in

$$E_{escape} = \frac{k_e \cdot (Q + 1) \cdot e^2}{r} \approx 3 \cdot 10^6 \, eV, \tag{5.3}$$

which can likely not be achieved with our laser intensity of $10^{16} \, W/cm^2$. Moreover, the influence of the Coulomb explosion at the onset of expansion is further reduced by its scaling of r^{-4} compared to the hydrodynamic expansion which scales with r^{-3}.

Therefore, a purely hydrodynamic expansion is most likely and considered in the following. From the calculations of section 2.6, the ion velocity for hydrodynamic expansion of a spherical plasma with homogeneous density is given as

$$\left(\frac{dr}{dt}\right)^2 = \frac{3 \cdot k_B \cdot T_{e0} \cdot Z}{m_i} \cdot \left(1 - \left(\frac{r_0}{r}\right)^2\right), \tag{5.4}$$

where, compared to equation 2.55, the assumption was made that the fraction of electrons which have left the plasma is negligibly small ($Q \approx 0$). The density distributions measured in this work, however, refer to the electrons since they determine the refractive index of the plasma. For the derivation of the ion velocity it was assumed that the ions are at rest at the beginning of the expansion and that the absorbed laser energy is transfered solely to the electrons. During the expansion the electrons then transfer their energy to the ions. Under the condition of energy conservation, the following therefore holds true for any time t after the beginning of the expansion:

$$N_e \cdot m_e \cdot v_e^2 = N_e \cdot m_e \cdot v_{e0}^2 - N_i \cdot m_i \cdot v_i^2, \tag{5.5}$$

where v_{e0} is the electron velocity at the beginning of the expansion and v_e and v_i are the electron and ion velocity at time t. Inserting 5.4 for the ion velocity yields

$$v_e = v_{e0} \cdot \frac{r_0}{r}. \tag{5.6}$$

This expression for the electron velocity can also be directly obtained from 2.51. Starting from the definition of temperature in an ideal gas $m_e \cdot v_e^2 = 3 \cdot k_B \cdot T_e$ one gets

$$v_e^2 = \frac{3 \cdot k_B \cdot T_e}{m_e} = \frac{3 \cdot k_B \cdot T_{e0}}{m_e} \left(\frac{r_0}{r}\right)^2 = v_{e0}^2 \cdot \left(\frac{r_0}{r}\right)^2. \tag{5.7}$$

Therefore the sphere radius

$$r\,(t) = \sqrt{2 \cdot r_0 \cdot v_{e0} \cdot t + r_0^2}. \tag{5.8}$$

For the simple case of a constant density (up to the radius described by the equation above), the density is automatically defined by the radius. In the case of a Gaussian density distribution, some adjustments can be made to employ the formalism. First, we assume that the expansion of the plasma front behaves the same as in the case of homogeneous density. We also assume that the plasma follows a simple, broadening Gaussian distribution throughout the expansion period. For late times this is valid as the distribution could be modeled best by a single Gaussian. At early times, when shock features (the moving Gaussian) are present, this approximation is still justified because the front of the plasma (the outermost border) is determined by the width of the central Gaussian (for example compare figure 5.6 and figure 5.4). We chose the front of the distribution (rather arbitrarily) by $r\left(n_e = 1/cm^3\right)$ to ensure that the number of electrons within the front is the same as in a homogeneous distribution. From the time-dependent radius of this front, a corresponding width of the entire Gaussian distribution can be calculated, which then determines the time course of the entire distribution $n_e\left(t\right)$

$$n_e\left(t\right) = n_{cold} \cdot e^{-\frac{r^2}{2 \cdot l_{cold}(t)^2}}, \tag{5.9}$$

where the central density n_{cold} is subject to the conservation of particle number. The expansion radius of an arbitrary density (referred to as isodensity radius) can then be obtained from

$$r\left(t, n_e\right) = \sqrt{-2 \cdot l_{cold}\left(t\right)^2 \cdot ln\left(\frac{3 \cdot n_e \cdot \sqrt{\frac{\pi}{2}} \cdot l_{cold}\left(t\right)^3}{n_i \cdot r_i^3}\right)}, \tag{5.10}$$

where $r_i = 0.5\,\mu m$ and $n_i = 194\,n_c$ and we must only keep in mind that the chosen n_e cannot be too large (it should always remain in the outermost region where the density decreases monotonically). For the determination of the temporal development of the density distribution, only the two initial parameters v_{e0} and r_0 are necessary. Due to the fact that no exact starting time of the expansion can be determined, the model is limited in the following to the range after the laser interaction, namely from t = 0 ps to t = 600 ps. The start parameter r_0 is obtained from the density profiles reconstructed from the transmission measurement. v_{e0} describes the expansion velocity at the time t = 0 ps and serves as a fit parameter. Figure 5.9 shows an example of what such an expansion looks like. Isodensity radii which can be determined from equation 5.10 are plotted against time. As starting conditions a plasma front at $r_0 = 5\,\mu m$ and the corresponding velocity of the expansion of $v_{e0} = 1\,\mu m/ps$ were arbitrarily chosen.

As can be seen, the distribution at time t = 0 ps already shows some expansion for all densities considered, similar to what can be reconstructed from the transmission diagnostic. Subsequently, the radii initially expand, with the critical density radius already reaching its maximum expansion after 10 ps and then beginning to shrink. After about 28 ps, the plasma expands to a point where it is completely undercritical.

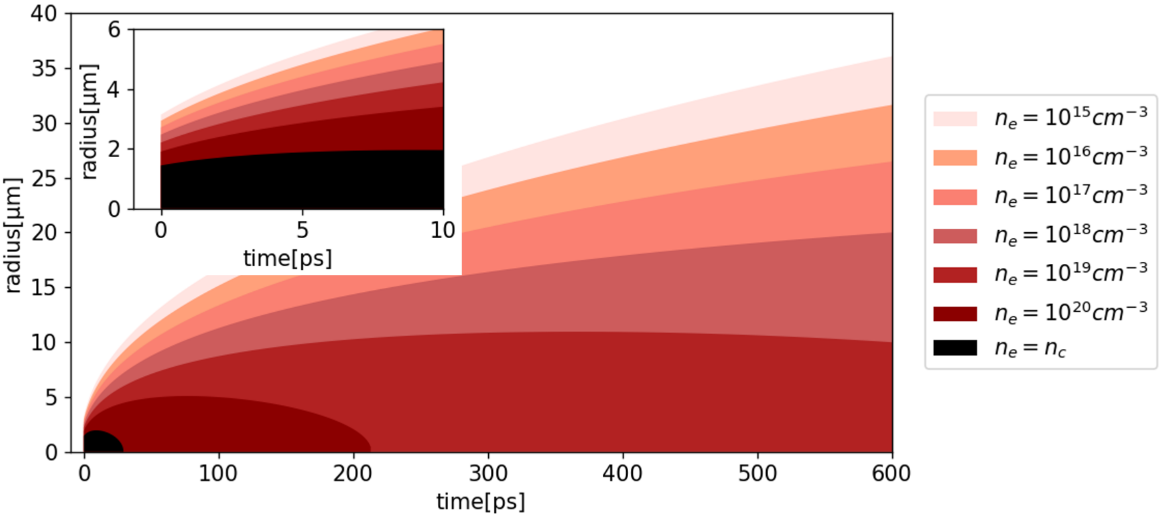

Figure 5.9: Exemplary expansion of a Gaussian density distribution calculated via equations 5.8 and 5.10 with arbitrary starting parameters $r_0 = 5\,\mu m$ for the plasma front at t = 0 ps and $v_{e0} = 1\,\mu m/ps$ as the expansion velocity, where different colors show the temporal course of distinct isodensity radii. The inset illustrates the expansion during the first 10 ps.

In order to compare the experimentally found distributions with the model, shots must first be sorted according to similar starting conditions (i.e. similar overlap between particle and laser focus). This is necessary because the starting parameter r_0, used as input for the model, is determined from the experimentally found distributions. Therefore, from table 5.2 the shots with an offset of 2.1 μm^2, 2.4 μm^2 and 3.3 μm^2 as well as the shots with offset 8.5 μm^2, 9.7 μm^2, 10.2 μm^2 and 10.5 μm^2 are grouped. The two remaining shots (12.0 μm^2 and 13.9 μm^2) are considered separately because they have large uncertainties in the transmission-determined density distribution due to their large offset. For both groups, the reconstructed distributions at time t = 0 ps are used to determine the propagation of the plasma front r_0. A mean value is formed in each case, which serves as the starting parameter for the model. The corresponding values are listed in table 5.3.

Delay [ps]	Offset [μm^2]	r_0 [μm]
3	2.1	15.3
39	2.4	14.3
193	3.3	13.8
mean	2.6	14.5

Delay [ps]	Offset [μm^2]	r_0 [μm]
1	10.5	10.4
193	8.5	9.9
226	10.2	11.4
593	9.7	8.5
mean	9.7	10.0

Table 5.3: Probe data grouped by offset with corresponding plasma front radius r_0.

First, the group with the smallest offset is considered. For this purpose, the experimentally found value of $r_0 = 14.5\,\mu m$ is taken as the model input parameter. Subsequently, v_{e0} is used to fit the model to the isodensity radii obtained from the individual distributions. For shots where different distributions where found in axial and radial dimension, the isodensity radii are determined seperately and the mean value is used for each radius. The result is shown in figure 5.10. Here, the model-based course of the different densities is again depicted by colored areas, while experimental measurement points are symbolized by different colored markers. The inset shows experimental data for t = 3 ps. To account for the temporal stretching of the probe pulse, an error of ± 2.6 ps was assumed for all data points of this diagnostic, while the error bars in y-direction account for the uncertanties of the parameter set in table 5.2. In the case of seperate distributions, the error represents the lower limit of the smaller distribution and the upper limit of the bigger distribution. In comparison with the experimental data, the best agreement is obtained for $v_{e0} = 3.8\,\mu m/ps$. The isodensity radii of the two measurement points at t = 39 ps and t = 193 ps agree well with the model-based expansion within the error bars. For the measurement at 3 ps, the radii up to $n_e = 10^{18}\,cm^{-3}$ also agree well with the model, but higher-density radii grow faster than predicted. This is due to the shock represented by the moving Gaussian, which at this time is not as dominant as in the transmission measurement, but still clearly present. The lower densities are defined by the width of the central Gaussian distribution and therefore in good agreement with the model.

For the second group, a starting parameter of $r_0 = 10.0\,\mu m$ was determined and the model was again fitted to the experimental data by adjusting v_{e0}. The result is illustrated in figure 5.11. With a starting velocity of $v_{e0} = 3.1\,\mu m/ps$, there is good

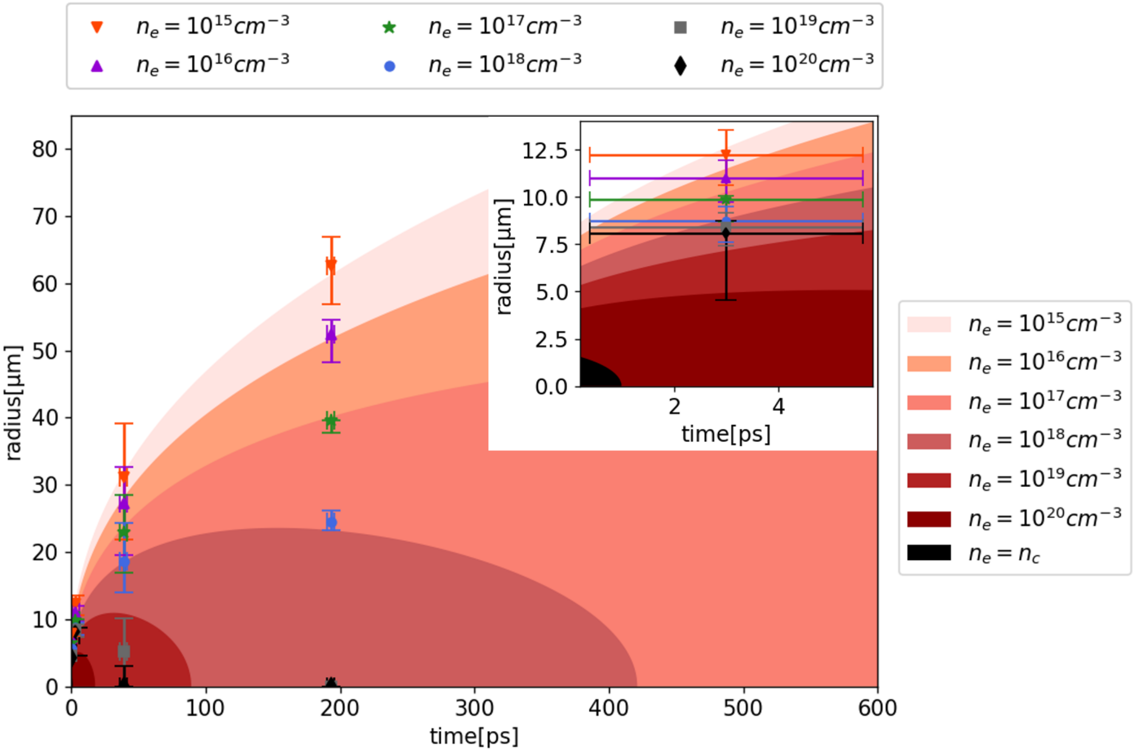

Figure 5.10: Comparison of modeled and experimentally determined temporal evolution of the density distribution for shots with high overlap with the laser focus. The model-based course of the isodensity radii is shown by colored areas, experimentally obtained radii are depicted by a set of colored markers. Input values of $r_0 = 14.5\,\mu m$ and $v_{e0} = 3.8\,\mu m/ps$ are used for calculating the model.

agreement with the experimental density distributions, as in the previous case. As before, for the data point immediately after the interaction, the low-density radii follow the model, while higher densities show faster expansion due to the shock, although this appears to be even more pronounced after 1 ps than in the previous case after 3 ps. This again suggests a rapid decay of the shock and a transition towards a regular Gaussian distribution.

Lastly, it is possible to check how well the expansion model agrees with the density distributions at time t = 0 ps determined from the transmission. The mean values of the isodensity radii of all data points belonging to the group are formed similarly as for the plasma front radius. In figure 5.12 the two cases are shown, where a) corresponds to the first group with small offset and b) to the one with larger offset. The error bars are derived from the maximum and minimum radius for each density within the group. In

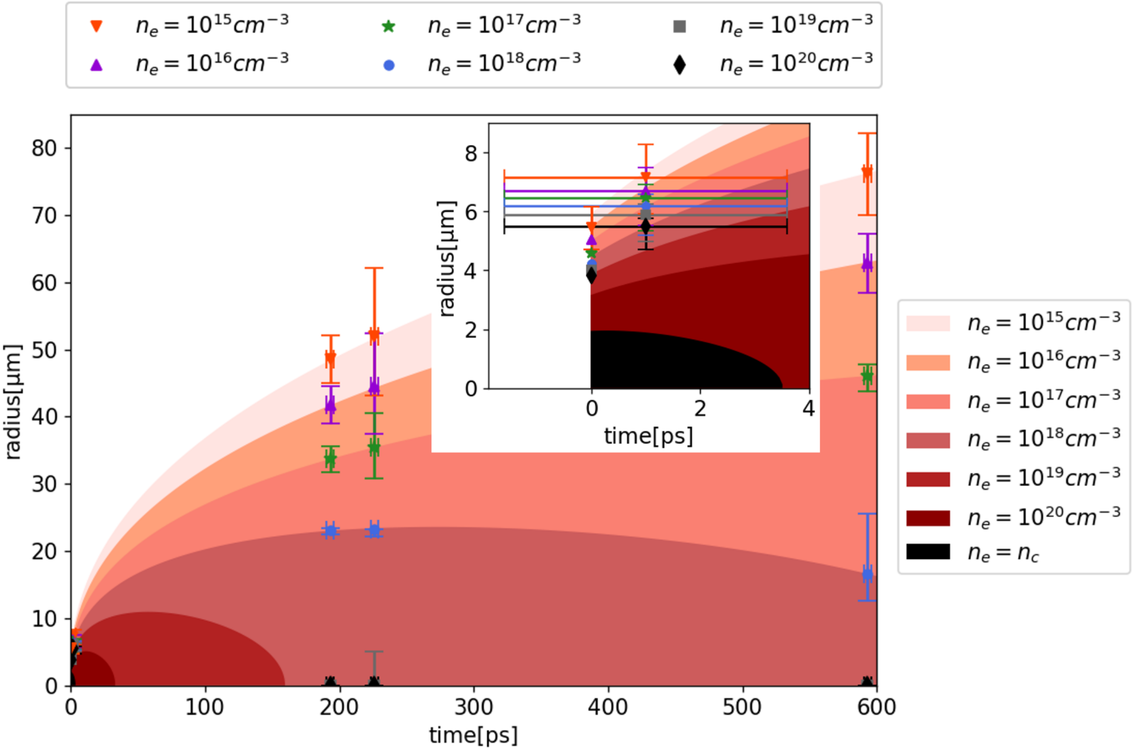

Figure 5.11: Comparison of modeled and experimentally determined temporal evolution of the density distribution for shots with medium overlap with the laser focus. The model-based course of the isodensity radii is shownby colored areas, experimentally obtained radii are depicted by a set of colored markers. Input values of $r_0 = 10.0\,\mu m$ and $v_{e0} = 3.1\,\mu m/ps$ are used for calculating the model.

both cases, the experimental radii of low densities are close to those of the model, with slightly lower propagation detected in the experiment. Nevertheless, an overlap can be observed within the error tolerance. Similar to the two data points at t = 1 ps and t = 3 ps before, the influence of the shock on the distribution can also be detected here. The expansion of high densities is again more advanced at this time than in the model.

For the last two data sets with the largest offset to the laser axis, the model is calculated individually, because the plasma front radii and the shape of the density distribution are strongly deviating for both cases. The respective models and corresponding experimental data points are shown in figure 5.13. For the shot with an offset of 12.0 μm^2, $r_0 = 5.5\,\mu m$ was determined from the transmission and fitted with $v_{e0} = 3.2\,\mu m/ps$, while for an offset of 13.9 μm^2, $r_0 = 4.1\,\mu m$ and $v_{e0} = 2.8\,\mu m/ps$. As before, there is good agreement for both probe data sets. For the expansion at

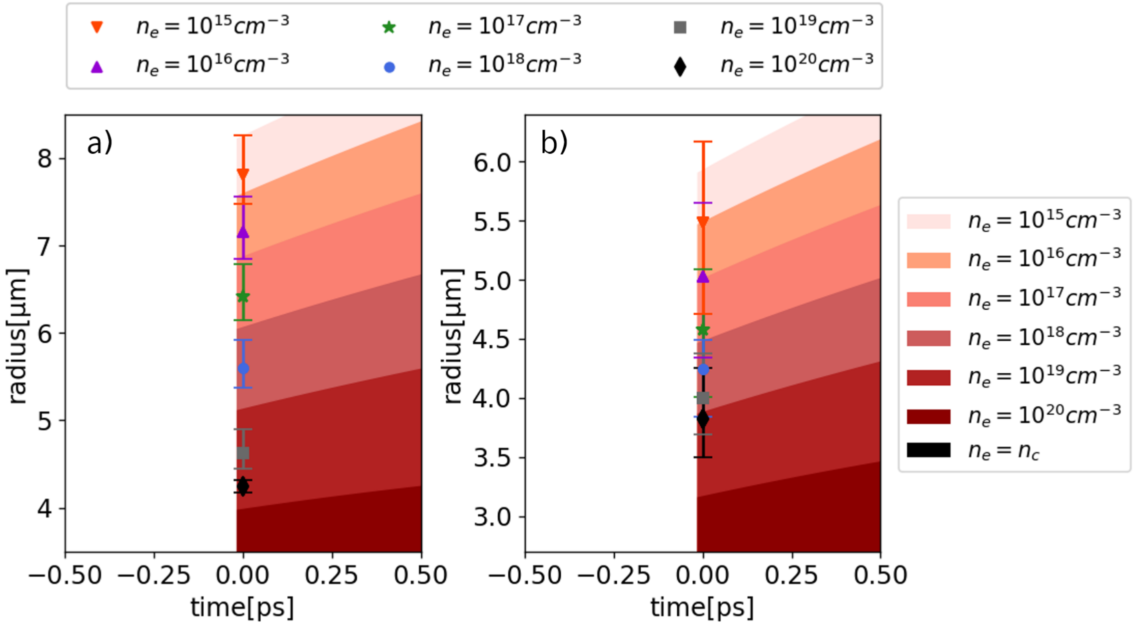

Figure 5.12: Comparison of modeled and experimentally determined temporal evolution of the density distribution for shots with both good (a)) and medium (b)) overlap with the laser focus at t = 0 ps. The model-based course of the isodensity radii is shown by colored areas, experimentally obtained radii are depicted by a set of colored markers.

time t = 0 ps, figure 5.13 a) shows a quite significant deviation, while in figure 5.13 b) the experimental radii are close to the model. This deviation can be attributed to the relatively large error in determining the width of the central Gaussian, l_{cold}, from the transmission. This uncertainty directly affects the determination of the radius of the plasma front and may provide an explanation for the discrepancy. Although a fitting of the function with only two grid points does not qualify for the confirmation of the model, in light of the two groups of data and their agreement with the model, these two extra data sets contribute more measurement points for the initial expansion velocity v_{e0}.

In summary, the temporal evolution of the experimental data can be described by the simple model assuming hydrodynamic expansion. It can be seen that plasmas with a better overlap between target and laser expand faster than plasmas with less overlap, which is to be expected. In the following, a possible connection between absorbed laser energy and expansion velocity will be investigated. As already shown, the expansion of the particle does not start when the peak intensity arrives at time

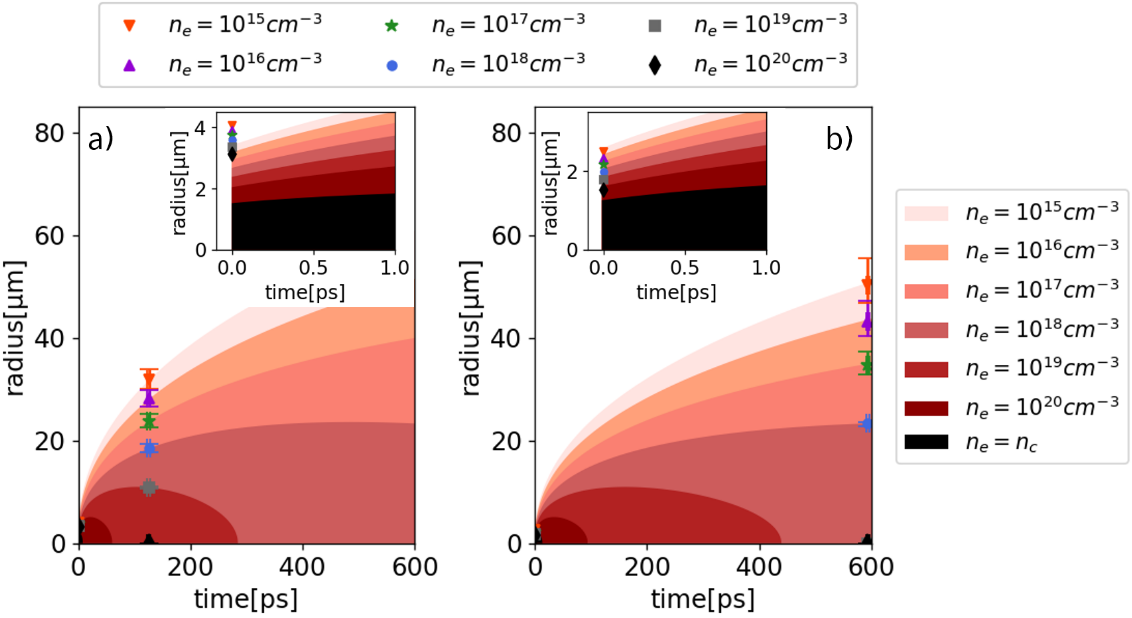

Figure 5.13: Comparison of modeled and experimentally determined temporal evolution of the density distribution for two shots with large offset to the laser axis. The model-based course of the isodensity radii is shown in color, experimentally obtained radii are depicted by a set of colored markers. Input values of $r_0 = 5.5\,\mu m$ and $v_{e0} = 3.2\,\mu m/ps$ (a)) and $r_0 = 4.1\,\mu m$ and $v_{e0} = 2.8\,\mu m/ps$ (b)) are used for calculating the model.

t = 0 ps, but already before that, however the exact time remains unknown due to the lack of data. Therefore $v_{eo}\,(t = 0ps)$ represents a plasma velocity that is already lowered due to the electron cooling during expansion. However, the determination of the expansion velocity at this point in time in concert with the knowledge about the density profile of the plasma offers the possibility to estimate the energy contained in the initial plasma which is necessary to reach the observed conditions at time t = 0 ps. This energy can be calculated via

$$E_{in} = \frac{1}{2} \cdot N_e \cdot m_e \cdot v_{e,in}^2 \tag{5.11}$$

where $v_{e,in}$ describes the initial plasma velocity at the start of expansion. It is related to v_{e0} via equation 5.6:

$$v_{e,in} = v_{e0} \cdot \frac{r_{0,in}}{r_0}. \tag{5.12}$$

To determine $r_{0,in}$ a further approximation is made: since the expansion model describes the propagation of a Gaussian distribution, the initial plasma with a step-like density distribution with a width of 0.5 μm, is approximated by a Gaussian distribution whose isodensity radius for $n_e = n_c$ assumes the same width. The plasma front radius $r_{0,in} = 1.33\,\mu m$ is obtained. Using equations 5.11 and 5.12, the following energies and velocities can be calculated (see table 5.4) for the four groups of data sets presented in figures 5.10, 5.11 and 5.13.

$r_0\,[\mu m]$	$v_{e0}\,[\mu m/ps]$	$r_{0,in}\,[\mu m]$	$v_{e,in}\,[\mu m/ps]$	$E_{in}\,[\mu J]$
14.5	3.8	1.33	41.4	139
10.0	3.1	1.33	23.4	44
5.5	3.2	1.33	13.2	14
4.1	2.8	1.33	8.6	6

Table 5.4: List of initial plasma energies E_{in} and velocities $v_{e,in}$, obtained from equation 5.11 and 5.12 using the corresponding parameters for each group of data sets with similar laser offset.

This shows a difference of more than one order of magnitude between the individual data sets. One explanation is of course the different overlap with the laser focus and the resulting different amount of laser energy to which the particle was exposed. In order to estimate how much of this is due to the overlap alone, it is calculated in the following which amount of laser energy a particle of 0.5 μm radius is exposed to at the respective positions in the focal plane (see figure 5.3). To calculate the temporal and spatial distribution of the laser energy in the focal plane, first a Gaussian distribution equivalent to the real focus is created with a FWHM of 6 µm. The sum over the entire distribution corresponds to the applied laser energy of $E_{tot} = 600\,\mu J$. It is then multiplied by a scaled temporal intensity distribution function from figure 3.14, whose integral over time corresponds to 1. Thus, for each point in time, a weighted spatial energy distribution whose integral over time and space corresponds exactly to the total laser energy is available. Due to the probe measurements with negative delay, the time period is limited to an interval from -14 ps to +120 fs, containing $> 95\%$ of the total 600 μJ. To determine the laser energy available to each particle, a circular mask with a diameter of 1 µm is then placed at the corresponding particle position and the energy input within this area is summed over the entire time period. For the group of shots with smallest offset this provides energies of 13.1, 12.9 and 12.0 μJ or a mean of 12.7 μJ. In the case of medium offset one obtains 6.8, 8.0, 7.0 and 7.2 μJ or a mean of 7.3 μJ. For the two shots with biggest offset, the values are 6.0 μJ and 5.2 μJ. Only in the last case, this energy is close to the value in table 5.4. And for this particular case, the reconstructed density profile is very close to an ionized sphere of 1 μm diameter.

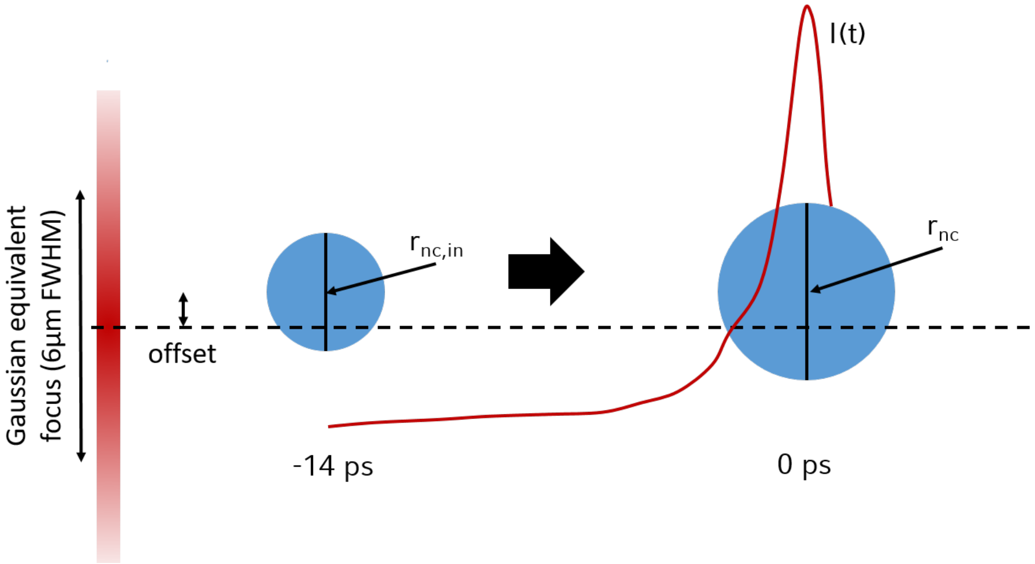

Figure 5.14: Model for energy within area of critical density: The target is positioned in a Gaussian equivalent laser focus of 6 μm FWHM. The lateral offset in the focal plane is obtained from figure 5.3. Starting with initial conditions $r_{nc,in}$ at t = -14 ps, the area of critical density increases linearly until t = 120 fs. The increase is given by the simulation-determined values r_{nc}. The energy is approximated by integrating the energy within the overcrital area from -14 ps to 120 fs.

The discrepancy for all other cases (that were exposed to a higher peak intensity, closer to the laser axis) suggests that the area within which laser energy can be absorbed increases with rising laser intensity. This is also in agreement with the already observed pre-expansion of the plasma which could be detected at time t = 0 ps. As has been shown in many other experiments, this area is closely related to the region where the plasma reaches critical density. Therefore, an increase of this area with increasing laser intensity is simulated in the following, with an assumed initial radius of 0.5 μm radius and the final size given by the values determined from the transmission (see figure 5.6). The starting time again is t = -14 ps. The subsequent growth is assumed to be linear since no further data points are available to model a different growth behavior. Figure 5.14 illustrates the model.

Using this approach, the values of potentially absorbable energy E_{nc} increase significantly as illustrated in table 5.5. Comparing those energies to the ones from table 5.4, one can cleary see that within the growing overcritical area, the plasma is exposed to sufficient laser energy to achieve the initial conditions that are required for explaining the measured expansion. Looking at the ratio E_{nc}/E_{tot} one notices that in each case the value is very close to the experimentally observed transmission loss. This agreement supports the validity of the simulation-determined values for the area of overcritical density and thus the obtained density distributions.

offset $[\mu m^2]$	$r_{nc}\,[\mu m]$	$E_{nc}\,[\mu J]$	$E_{nc}/E_{tot}[\%]$	exp. TM loss[%]
2.1	4.05	397	66	61
2.4	4.05	394	66	60
3.3	3.92	365	61	58
10.5	3.36	205	34	36
8.5	3.92	294	49	48
10.2	3.36	208	35	39
9.7	3.08	180	30	31
12.0	2.54	116	19	23
13.9	1.08	17	3	6

Table 5.5: For each shot, the offset from the laser axis and the energy contained within the growing area of critical density E_{nc} are listed. Moreover, the ratio of this energy to the total pulse energy E_{tot} is compared with the experimentally determined loss of transmitted light in each case.

The absorption f_A, given by the ratio of E_{in} and group-specific mean values of E_{nc}, is 36 % for the group with best overlap, 20 % for the data set with medium overlap and 12 % and 35 % for the two individual data points with large offset. As the position of all shots is known in the focal plane, the individual absorption values can be correlated to a peak intensity. This relation is plotted in figure 5.15, where the peak intensity is calculated for the individual offsets (mean value for groups), based on figure 5.3. For both groups with small and medium offset, the error bars are calculated from the minimum and maximum values of E_{nc} and peak intensity within the group. For the

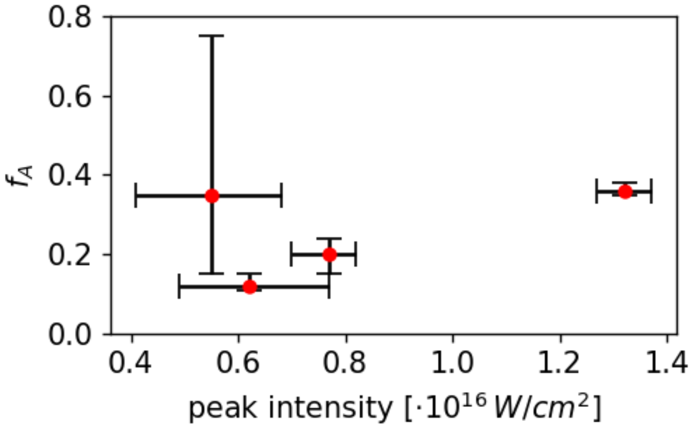

Figure 5.15: Experimentally determined fractional absorption versus position-dependend peak intensity.

two single data points, the y-error represents the upper and lower limit of E_{nc} and thus f_A, based on the error of the radius of overcritial density from figure 5.6. In the x-direction, the error accounts for an approximated positional inaccuracy within in focal plane of $\Delta x = \Delta y = \pm 0.25 \mu m$.

Figure 5.15 indicates that the absoption is correlated to the respective offset (and thus peak intensity) of each particle. In order to understand this behaviour it is first necessary to verify the dominant absorption mechanism. For peak intensities around $10^{16}\,W/cm^2$, resonance absorption and vacuum heating are generally assumed, where the plasma scale length can be used to distinguish between both cases [84]. The scale length most relevant for absorption is the one present around the fs-short main pulse, as most of the pulse energy is contained within several 10s of femtoseconds around t = 0 ps. Due to the reconstructed density distributions from the transmission measurement, we have access to this parameter. Figure 5.16 shows cutouts of the density distribution aquired from the transmission analysis, where a) and b) are respresentative examples of the two groups with smallest and medium offset and c) and d) show the two shots that were considered individually in the expansion analysis. The plasma scale length L is approximated by a linear fit that best reproduces the gradient of the electron density at the position $r\,(n_e = n_c)$ and defined as the distance between the two points where the fit equals $n_e = n_c$ and $n_e = 0$. From figure 5.16, one obtains values between $L/\lambda = 0.25$ and $L/\lambda = 0.56$, suggesting that resonance absorption is the main mechanism to consider. This is also in line with other experiments in the context of laser-droplet interaction in a similar intensity regime [114, 115].

Moreover, figure 5.16 reveals that the scale length varies with the respective off-

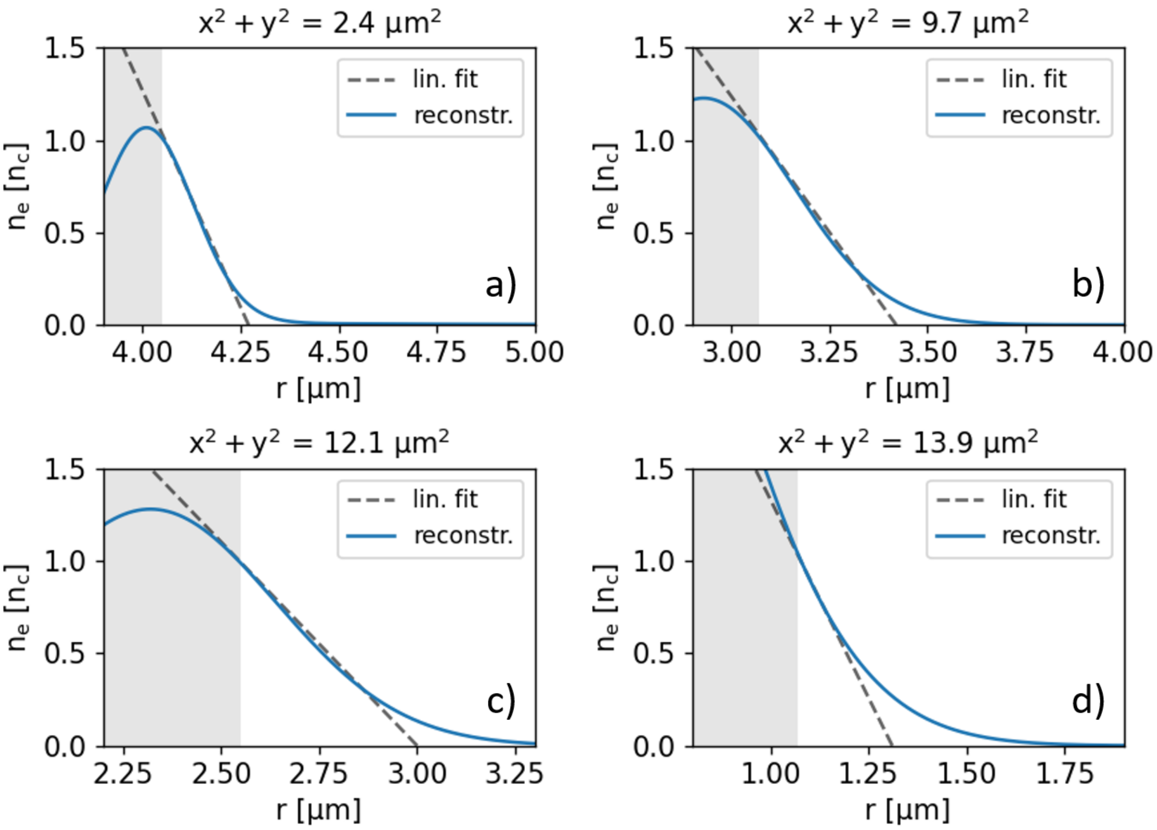

Figure 5.16: Cutouts of the density distribution obtained by the transmission analysis are shown, where a) and b) are representative examples for the two groups with small and medium offset. c) and d) show the density distributions for the two shots considered seperately in the expansion analysis. A linear fit is used to model the electron density gradient at the position of critical density. The grey bars indicate the part of the density distribution that is inaccessible for the laser.

set. Recalling equations 2.39 one immediately notices that the fractional absorption is strongly depending on L. Based on those equations, Wu et al. [116] have developed a simple analytic model to estimate the resonantly absorbed energy of a spherical target depending on the plasma scale length. By determining the scale length for each shot of table 5.5 (and using the offset for the respective peak intensity), the expected absorption values can be calculated using equation (7) of [116] and compared to our experimentally determined values of figure 5.15. The results are shown in figure 5.17.

Here, the experimentally obtained absorption values are shown in red, while values from the analytic model are depicted in blue. The green dots represent the respective plasma scale lengths, used as input for the analytic model. The error margins of the

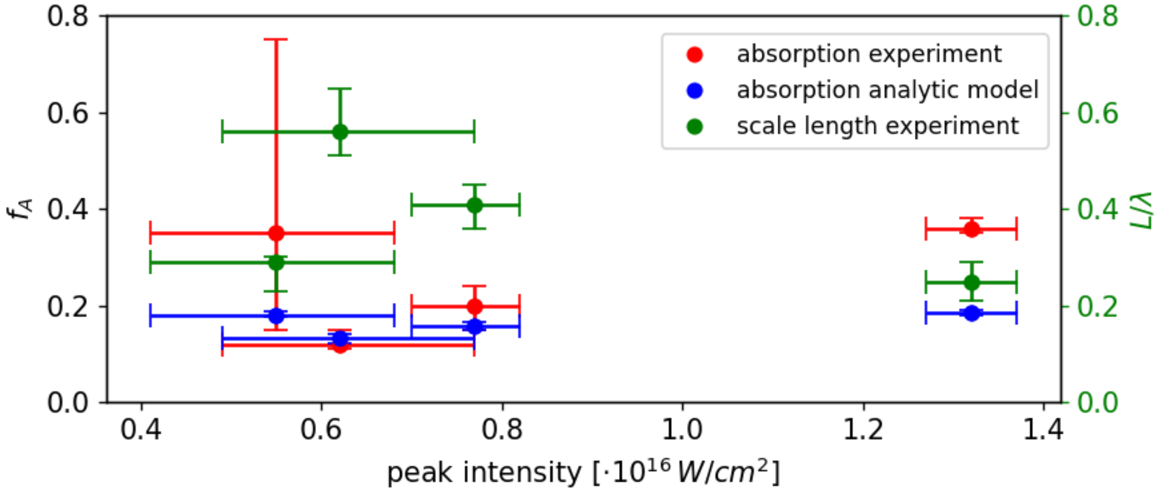

Figure 5.17: Comparison of absorption values and scale length: red dots show the experimentally determined absorption values from figure 5.15, while values obtained from the analytic model of [116] are represented by blue dots. The respective scale lengths, used as input for the analytic model, are depicted in green. The error bars for the scale length in y-direction are determined by the min/max-value within the two groups and from the minimum and maximum scale length for the individual shots based on the error margins of the reconstructed density distribution. The y-error for the analytic model is calculated from the error margins of the scale length.

scale length in y-direction are either obtained by the min/max-value within the groups with small and medium offset or by the minimum and maximum scale length based on the error margins of the reconstructed density distribution (see figure 5.4). The analytic model predicts lower absorption fractions than determined experimentally, especially in the two cases where highest absorption is measured in the experiment. However, both agree qualitatively in the intensity-dependend course of absorption. The increase in absorption for the lowest peak intensity can be reproduced in the analytic model and is caused by the decrease in scale length compared to the next two data points with higher peak intensity. The reason for this drop can be seen in figure 5.16: for the three cases with higher overlap, the scale length is defined by the width of the decentralized Gaussian component. As shown in the transmission analysis the width increases with larger offset (lower peak intensity) which leads to a larger scale length and thus lower absorption. In the case of biggest offset however, the additional Gaussian is located close to the center, hence the density distribution is mostly determined by the steeply decaying central Gaussian. This results in a smaller scale length and higher absorption, in line with the experimental observations. In summary, the intensity dependence of the experimentally determined absorption values can be reproduced by a simple analytical model of resonance absorption using the scale lengths derived from the experimental data. The deviation in absolute values suggests that other processes may have to be taken into account and encourages further studies in the field of expanding microplasmas.

Chapter 6

Summary and Outlook

Contents

6.1 Summary 129
6.2 Outlook 130

6.1 Summary

The reconstructed density distribution provides relevant plasma parameters in great detail from transmission images when experimental quantities such as beamprofiles or spatial and temporal intensity distribution are recorded in high quality and an appropriate model is chosen for the numerical simulations. These findings can help to further improve the understanding of physical processes within the laser-plasma interaction, for example for laser-ion acceleration in near-critical micro-plasmas, where the plasma density is a crucial parameter (e.g. [39]). Furthermore, the comparison of the numerical model with experimental data allows to recognize potentially occurring asymmetries. Those could be investigated qualitatively or even quantitatively, depending on the desired complexity of the model.

Studying the temporal evolution of the density distribution allows to develop or verify expansion models for the laser-irradiated plasma. From these models, the energy within the plasma can be approximated and provides the basis to investigate the influence of parameters such as peak intensity or plasma scale length on quantities like fractional absorption or expansion velocity. Such comparisons can, for example, be used to validate theoretical scalings. Additionally, time-resolved studies as performed in this work can in the future serve as a benchmark for numerical simulation codes such as RALEF. This also provides the opportunity to verify the accuracy of measured experimental quantities which are often used as input parameters in these simulations.

6.2 Outlook

The simple approach presented in this work has shown the potential of gathering detailed information about the plasma during and after the laser-interaction. Building on the current setup, a variety of improvements can be implemented. One of the main challenges was the low number of data points that could be obtained from the experiment. One solution would of course be to increase the positioning accuracy and stability of the target system; promising improvements have already been made in another experiment [117]. In addition, the number of data points available from a single shot can be improved by implementing multi-color probing techniques (e.g. [45, 118]). Not only would this significantly increase the number of data points (by an order of magnitude), but this would also allow to study the plasma expansion of a single target, thus decreasing the influence of shot-to-shot fluctuations. Additionally, positional changes of the center of the density distribution over time could be observed via the recorded probe images if one can exclude asymmetries in the plasma to produce a similar change in the diffraction pattern as a global shift in position (e.g. via simulations).

Another improvement can be made concerning the current upper limit of laser intensity in the pump pulse due to stray light and self-emitted light from the plasma affecting the probe diagnostic. Although the intrinsic probing via the pump provides a tool that is not limited in this regard, it is fixed to t = 0 ps, thus no time-resolved measurements are currently possible at intensities above $10^{16}\,W/cm^2$. A potential solution would be the use of an off-harmonic probe pulse, such that disturbing light sources can be effectively damped via spectral filters, significantly increasing the signal-to-noise ratio in this diagnostic. A change of the probe towards higher frequencies would furthermore allow to access regions of higher density, revealing the distribution beyond the current limit of the critical density associated to the wavelength of the pump [119]. The developed simulation tools can easily be adjusted to model diffraction at different wavelengths and could still be used to compare experimental results with numerically implemented density distributions.

With regard to the distribution model, so far asymmetries have been neglected for the sake of simplicity and a moderate number of free parameters. However, various experimental images show (expected) non-spherical diffraction patterns, indicating asymmetries in particular during early phases of the interaction, primarily along the laser propagation axis. This behavior is also observed in the RALEF simulations. In order to quantify these effects, the hydrodynamic simulations can directly be used as an input for calculating the diffraction patterns.

This work can be seen as a first step towards studying the expansion dynamics of micron-sized spherical plasmas. The simple experimental approach has shown that the plasma can be studied quantitatively if the laser- and target-conditions are well defined. This provides a unique opportunity to visualize and study plasma processes and compare results with simulation tools.

List of Abbreviations

AC	**A**lternating **C**urrent
ASE	**A**mplified **S**pontaneous **E**mission
ATI	**A**bove **T**hreshold **I**onization
BSI	**B**arrier **S**uppression **I**onization
CALA	**C**entre for **A**dvanced **L**aser **A**pplications
CMOS	**C**omplementary **m**etal-**o**xid-**s**emiconductor
CO	**C**ut**o**ut
CPA	**C**hirped **P**ulse **A**mplification
CW	**C**ontinuous **W**ave
DC	**D**irect **C**urrent
FEOS	**F**rankfurt **e**quation-**o**f-**s**tate
FFT	**F**ast **F**ourier **T**ransform
FROG	**F**requency-**r**esolved **o**ptical **g**ating
FWHM	**F**ull **w**idth at **h**alf **m**aximum
GS	**G**rid**s**ize
HE	**H**igh **E**nergy
LE	**L**ow **E**nergy
LWFA	**L**aser-**W**ake**f**ield **A**cceleration

MPI	**M**ulti**p**hoton **I**onization
Nd:YAG	**n**eodymium-**d**oped **y**ttrium **a**luminium **g**arnet
PHELIX	**P**etawatt **H**igh **E**nergy **L**aser for Heavy **I**on E**x**periments
PIC	**P**article-**i**n-**C**ell
PSD	**P**osition **s**ensitive **d**evice
RALEF	**R**adiation **A**rbitrary **L**agrange-**E**ulerian **F**luid
Regen	**Regen**erative amplifier
RES	**Res**olution
TCC	**T**arget **C**hamber **C**enter
TI	**T**unnel **I**onization
Ti:Sa	**ti**tanium-**sa**pphire
TNSA	**T**arget **N**ormal **S**heath **A**cceleration
ZEUS	**Z**inths **E**xtremly **U**seful **S**uperlaser

Publications and Conference Contributions

Peer-Reviewed Publications

2022

- F.H. Lindner, E.G. Fitzpatrick, D. Haffa, L. Ponnath, A.-K. Schmidt, **M. Speicher**, B. Zielbauer, J. Schreiber and P.G. Thirolf, "Charge-state resolved laser acceleration of gold ions to beyond 7MeV/u," *Scientific Reports*, vol. 12, no. 1, pp. 1-11, 2022.

2021

- A. Prasselsperger, M. Coughlan, N. Breslin, M. Yeung, C. Arthur, H. Donnelly, S. White, M. Afshari, **M. Speicher**, R. Yang, B. Villagomez-Bernabe, F.J. Currell, J. Schreiber and B. Dromey, "Real-Time Electron Solvation Induced by Bursts of Laser-Accelerated Protons in Liquid Water," *Physical Review Letters*, vol. 127, no. 18, p. 186001, 2021.

2020

- T.F. Rösch, Z. Szabó, D. Haffa, J. Bin, S. Brunner, F.S. Englbrecht, A.A. Friedl, Y. Gao, J. Hartmann, P. Hilz, C. Kreuzer, F.H. Lindner, T.M. Ostermayr, R. Polanek, **M. Speicher**, E.R. Szabó, D. Taray, T. Tökés, M. Würl, K. Parodi, K. Hideghéty and J. Schreiber, "A feasibility study of zebrafish embryo irradiation with laser-accelerated protons," *Review of Scientific Instruments*, vol. 91, no. 6, p. 063303, 2020.

2019

- D. Haffa, J. Bin, **M. Speicher**, K. Allinger, J. Hartmann, C. Kreuzer, E. Ridente, T.M. Ostermayr and J. Schreiber, " Temporally Resolved Intensity Contouring (TRIC) for characterization of the absolute spatio-temporal intensity distribution of a relativistic, femtosecond laser pulse," *Scientific Reports*, vol 9, no. 1, pp. 1-9, 2019.

- J. Szerypo, W. Ma, G. Bothmann, D. Hahner, M. Haug, P. Hilz, C. Kreuzer, R. Lange, S. Seuferling, **M. Speicher**, F. Stehr, S. Stork, P.G. Thirolf, J. Schreiber and H.-F. Wirth, " Target fabrication for laser-ion acceleration research at the Technological Laboratory of the LMU Munich," *Matter and Radiation at Extremes*, vol. 4, no. 3, p. 035201, 2019.

- D. Haffa, R. Yang, J. Bin, S. Lehrack, F.-E. Brack, H. Ding, F.S. Englbrecht, Y. Gao, J. Gebhard, M. Gilljohann, J. Götzfried, J. Hartmann, S. Herr, P. Hilz, S.D. Kraft, C. Kreuzer, F. Kroll, F.H. Lindner, J. Metzkes-Ng, T.M. Ostermayr, E. Ridente, T.F. Rösch, G. Schilling, H.-P. Schlenvoigt, **M. Speicher**, D. Taray, M. Würl, K. Zeil, U. Schramm, S. Karsch, K. Parodi, P.R. Bolton, W. Assman and J. Schreiber, "I-BEAT: Ultrasonic method for online measurement of the energy distribution of a single ion bunch", *Scientific Reports*, vol. 9, no. 1, pp. 1-7, 2019.

2018

- **M. Speicher**, D. Haffa, M.A.O. Haug, J. Bin, Y. Gao, J. Hartmann, P. Hilz, C. Kreuzer, F.H. Lindner, T.M. Ostermayr, T.F. Rösch, R. Yang and J. Schreiber, "Integrated double-plasma-mirror targets for contrast enhancement in laser ion acceleration," *Journal of Physics: Conference Series*, vol. 1079, no. 1, p. 012002, 2018.

- J. Hartmann, D. Haffa, **M. Speicher**, J. Bin, P. Hilz, C. Kreuzer, T. Ostermayr, S. Lehrack and J. Schreiber, "The spatial contrast challenge for intense laser-plasma experiments", vol. 1079, no. 1, p. 012003, 2018.

- F.H. Lindner, J.H. Bin, F. Englbrecht, P.R. Bolton, Y. Gao, J. Hartmann, P. Hilz, T.M. Ostermayr, T.F. Rösch, **M. Speicher**, K. Parodi, P.G. Thirolf and J. Schreiber, " A novel approach to electron data background treatment in an online wide-angle spectrometer for laser-accelerated ion and electron bunches," *Review of Scientific Instruments*, vol. 89, no. 1, p. 013301, 2018.

2017

- Y. Gao, J. Bin, D. Haffa, C. Kreuzer, J. Hartmann, **M. Speicher**, F.H. Lindner, T.M. Ostermayr, P. Hilz, T.F. Rösch, S. Lehrack, F. Englbrecht, S. Seuferling, M. Gilljohann, H. Ding, W. Ma, K. Parodi and J. Schreiber, "An automated, 0.5 Hz nano-foil target positioning system for intense laser plasma experiments," *High Power Laser Science and Engeneering*, vol. 5, 2017.

- F.H. Lindner, D. Haffa, J.H. Bin, F. Englbrecht, Y. Gao, J. Gebhard, J. Hartmann, P. Hilz, C. Kreuzer, S. Lehrack, T.M. Ostermayr, T.F. Rösch, **M. Speicher**, M. Würl, K. Parodi, J. Schreiber and P.G. Thirolf, "Towards swift ion bunch acceleration by high-power laser pulses at the Centre for Advanced Laser Applications (CALA)," *Nuclear Instruments and Methods in Physics Research Section B: Beam Interactions with Materials and Atoms*, vol. 402, pp. 354-357, 2017.

Conference Contributions

- **3rd European Advanced Accelerator Concepts Workshop (EAAC 2017)**, "HDR spatio-temporal intensity mapping by single-shot optical probing", Oral, La Biodola, Isola d'Elba, 2017

- **4th Targetry for High Repetition Rate Laser-Driven Sources Workshop (TARG4)**, "Small-scale target design with integrated double plasma mirror", Poster, Milan, 2019

Bibliography

[1] E. Rutherford, "Address of the President, Sir Ernest Rutherford, at the anniversary meeting, November 30, 1926," *Proceedings of the Royal Society of London. Series A, Containing Papers of a Mathematical and Physical Character*, vol. 113, no. 765, pp. 481–495, 1927.

[2] G. Aad, T. Abajyan, B. Abbott, J. Abdallah, S. A. Khalek, A. A. Abdelalim, R. Aben, B. Abi, M. Abolins, O. AbouZeid, *et al.*, "Observation of a new particle in the search for the Standard Model Higgs boson with the ATLAS detector at the LHC," *Physics Letters B*, vol. 716, no. 1, pp. 1–29, 2012.

[3] S. Chatrchyan, V. Khachatryan, A. M. Sirunyan, A. Tumasyan, W. Adam, E. Aguilo, T. Bergauer, M. Dragicevic, J. Erö, C. Fabjan, *et al.*, "Observation of a new boson at a mass of 125 GeV with the CMS experiment at the LHC," *Physics Letters B*, vol. 716, no. 1, pp. 30–61, 2012.

[4] W. Röntgen, "Über eine neue Art von Strahlen: vorläufige Mitteilung," *Sitzungsber. Phys. Med. Gesell.*, 1895.

[5] G. N. Hounsfield, "Computerized transverse axial scanning (tomography): Part 1. Description of system," *The British Journal of Radiology*, vol. 46, no. 552, pp. 1016–1022, 1973.

[6] J. Thariat, J.-M. Hannoun-Levi, A. S. Myint, T. Vuong, and J.-P. Gérard, "Past, present, and future of radiotherapy for the benefit of patients," *Nature Reviews Clinical Oncology*, vol. 10, no. 1, pp. 52–60, 2013.

[7] W. D. Newhauser and R. Zhang, "The physics of proton therapy," *Physics in Medicine & Biology*, vol. 60, no. 8, p. R155, 2015.

[8] A. P. Chernyaev and S. M. Varzar, "Particle accelerators in modern world," *Physics of Atomic Nuclei*, vol. 77, no. 10, pp. 1203–1215, 2014.

[9] S. Matsumoto, T. Abe, Y. Higashi, T. Higo, and Y. Du, "High gradient test at Nextef and high-power long-term operation of devices," *Nuclear Instruments and Methods in Physics Research Section A: Accelerators, Spectrometers, Detectors and Associated Equipment*, vol. 657, no. 1, pp. 160–167, 2011.

[10] A. Degiovanni, W. Wuensch, and J. G. Navarro, "Comparison of the conditioning of high gradient accelerating structures," *Physical Review Accelerators and Beams*, vol. 19, no. 3, p. 032001, 2016.

[11] E. I. Simakov, V. A. Dolgashev, and S. G. Tantawi, "Advances in high gradient normal conducting accelerator structures," *Nuclear Instruments and Methods in Physics Research Section A: Accelerators, Spectrometers, Detectors and Associated Equipment*, vol. 907, pp. 221–230, 2018.

[12] V. I. Veksler, "The principle of coherent acceleration of charged particles," *The Soviet Journal of Atomic Energy*, vol. 2, no. 5, pp. 525–528, 1957.

[13] F. Mako and T. Tajima, "Collective ion acceleration by a reflexing electron beam: Model and scaling," *The Physics of Fluids*, vol. 27, no. 7, pp. 1815–1820, 1984.

[14] T. Maiman, "Stimulated Optical Radiation in Ruby," *Nature*, vol. 187, no. 4736, pp. 493–494, 1960.

[15] T. Tajima and J. M. Dawson, "Laser Electron Accelerator," *Physical Review Letters*, vol. 43, no. 4, p. 267, 1979.

[16] F. J. McClung and R. W. Hellwarth, "Giant Optical Pulsations from Ruby," *Applied Optics*, vol. 1, no. 101, pp. 103–105, 1962.

[17] D. Strickland and G. Mourou, "Compression of amplified chirped optical pulses," *Optics Communications*, vol. 55, no. 6, pp. 447–449, 1985.

[18] E. Esarey, C. B. Schroeder, and W. P. Leemans, "Physics of laser-driven plasma-based electron accelerators," *Reviews of Modern Physics*, vol. 81, no. 3, p. 1229, 2009.

[19] A. J. Gonsalves, K. Nakamura, J. Daniels, C. Benedetti, C. Pieronek, T. C. H. De Raadt, S. Steinke, J. H. Bin, S. S. Bulanov, J. Van Tilborg, *et al.*, "Petawatt Laser Guiding and Electron Beam Acceleration to 8 GeV in a Laser-Heated Capillary Discharge Waveguide," *Physical Review Letters*, vol. 122, no. 8, p. 084801, 2019.

[20] R. Snavely, M. H. Key, S. P. Hatchett, T. E. Cowan, M. Roth, T. W. Phillips, M. A. Stoyer, E. A. Henry, T. C. Sangster, M. S. Singh, *et al.*, "Intense High-Energy Proton Beams from Petawatt-Laser Irradiation of Solids," *Physical Review Letters*, vol. 85, no. 14, p. 2945, 2000.

[21] A. Maksimchuk, S. Gu, K. Flippo, D. Umstadter, and V. Y. Bychenkov, "Forward Ion Acceleration in Thin Films Driven by a High-Intensity Laser," *Physical Review Letters*, vol. 84, no. 18, p. 4108, 2000.

[22] E. L. Clark, K. Krushelnick, J. R. Davies, M. Zepf, M. Tatarakis, F. N. Beg, A. Machacek, P. A. Norreys, M. I. K. Santala, I. Watts, *et al.*, "Measurements of Energetic Proton Transport through Magnetized Plasma from Intense Laser Interactions with Solids," *Physical Review Letters*, vol. 84, no. 4, p. 670, 2000.

[23] S. C. Wilks, A. B. Langdon, T. E. Cowan, M. Roth, M. Singh, S. Hatchett, M. H. Key, D. Pennington, A. MacKinnon, and R. A. Snavely, "Energetic proton generation in ultra-intense laser–solid interactions," *Physics of Plasmas*, vol. 8, no. 2, pp. 542–549, 2001.

[24] F. Wagner, O. Deppert, C. Brabetz, P. Fiala, A. Kleinschmidt, P. Poth, V. A. Schanz, A. Tebartz, B. Zielbauer, M. Roth, *et al.*, "Maximum Proton Energy above 85 MeV from the Relativistic Interaction of Laser Pulses with Micrometer Thick CH_2 Targets," *Physical Review Letters*, vol. 116, no. 20, p. 205002, 2016.

[25] I. J. Kim, K. H. Pae, I. W. Choi, C.-L. Lee, H. T. Kim, H. Singhal, J. H. Sung, S. K. Lee, H. W. Lee, P. V. Nickles, *et al.*, "Radiation pressure acceleration of protons to 93 MeV with circularly polarized petawatt laser pulses," *Physics of Plasmas*, vol. 23, no. 7, p. 070701, 2016.

[26] A. Higginson, R. J. Gray, M. King, R. J. Dance, S. D. R. Williamson, N. M. H. Butler, R. Wilson, R. Capdessus, C. Armstrong, J. S. Green, *et al.*, "Near-100 MeV protons via a laser-driven transparency-enhanced hybrid acceleration scheme," *Nature Communications*, vol. 9, no. 1, pp. 1–9, 2018.

[27] H. Daido, M. Nishiuchi, and A. S. Pirozhkov, "Review of laser-driven ion sources and their applications," *Reports on Progress in Physics*, vol. 75, no. 5, p. 056401, 2012.

[28] A. Macchi, M. Borghesi, and M. Passoni, "Ion acceleration by superintense laser-plasma interaction," *Reviews of Modern Physics*, vol. 85, no. 2, p. 751, 2013.

[29] J. Schreiber, P. R. Bolton, and K. Parodi, "Invited Review Article:"Hands-on" laser-driven ion acceleration: A primer for laser-driven source development and potential applications," *Review of Scientific Instruments*, vol. 87, no. 7, p. 071101, 2016.

[30] B. M. Hegelich, B. J. Albright, J. Cobble, K. Flippo, S. Letzring, M. Paffett, H. Ruhl, J. Schreiber, R. K. Schulze, and J. C. Fernández, "Laser acceleration of quasi-monoenergetic MeV ion beams," *Nature*, vol. 439, no. 7075, pp. 441–444, 2006.

[31] D. Jung, L. Yin, B. J. Albright, D. C. Gautier, R. Hörlein, D. Kiefer, A. Henig, R. Johnson, S. Letzring, S. Palaniyappan, *et al.*, "Monoenergetic Ion Beam Generation by Driving Ion Solitary Waves with Circularly Polarized Laser Light," *Physical Review Letters*, vol. 107, no. 11, p. 115002, 2011.

[32] S. Kar, K. F. Kakolee, B. Qiao, A. Macchi, M. Cerchez, D. Doria, M. Geissler, P. McKenna, D. Neely, J. Osterholz, *et al.*, "Ion Acceleration in Multispecies Targets Driven by Intense Laser Radiation Pressure," *Physical Review Letters*, vol. 109, no. 18, p. 185006, 2012.

[33] S. Steinke, P. Hilz, M. Schnürer, G. Priebe, J. Bränzel, F. Abicht, D. Kiefer, C. Kreuzer, T. Ostermayr, J. Schreiber, *et al.*, "Stable laser-ion acceleration in the light sail regime," *Physical Review Special Topics-Accelerators and Beams*, vol. 16, no. 1, p. 011303, 2013.

[34] C. A. J. Palmer, N. P. Dover, I. Pogorelsky, M. Babzien, G. I. Dudnikova, M. Ispiriyan, M. N. Polyanskiy, J. Schreiber, P. Shkolnikov, V. Yakimenko, *et al.*, "Monoenergetic Proton Beams Accelerated by a Radiation Pressure Driven Shock," *Physical Review Letters*, vol. 106, no. 1, p. 014801, 2011.

[35] D. Haberberger, S. Tochitsky, F. Fiuza, C. Gong, R. A. Fonseca, L. O. Silva, W. B. Mori, and C. Joshi, "Collisionless shocks in laser-produced plasma generate monoenergetic high-energy proton beams," *Nature Physics*, vol. 8, no. 1, pp. 95–99, 2012.

[36] H. Schwoerer, S. Pfotenhauer, O. Jäckel, K.-U. Amthor, B. Liesfeld, W. Ziegler, R. Sauerbrey, K. W. D. Ledingham, and T. Esirkepov, "Laser-plasma acceleration of quasi-monoenergetic protons from microstructured targets," *Nature*, vol. 439, no. 7075, pp. 445–448, 2006.

[37] S. Ter-Avetisyan, B. Ramakrishna, R. Prasad, M. Borghesi, P. V. Nickles, S. Steinke, M. Schnürer, K. I. Popov, L. Ramunno, N. V. Zmitrenko, *et al.*, "Generation of a quasi-monoergetic proton beam from laser-irradiated sub-micron droplets," *Physics of Plasmas*, vol. 19, no. 7, p. 073112, 2012.

[38] T. M. Ostermayr, D. Haffa, P. Hilz, V. Pauw, K. Allinger, K.-U. Bamberg, P. Böhl, C. Bömer, P. R. Bolton, F. Deutschmann, *et al.*, "Proton acceleration by irradiation of isolated spheres with an intense laser pulse," *Physical Review E*, vol. 94, no. 3, p. 033208, 2016.

[39] P. Hilz, T. M. Ostermayr, A. Huebl, V. Bagnoud, B. Borm, M. Bussmann, M. Gallei, J. Gebhard, D. Haffa, J. Hartmann, *et al.*, "Isolated proton bunch acceleration by a petawatt laser pulse," *Nature Communications*, vol. 9, no. 1, pp. 1–9, 2018.

[40] J. J. Macklin, J. D. Kmetec, and C. L. Gordon III, "High-Order Harmonic Generation Using Intense Femtosecond Pulses," *Physical Review Letters*, vol. 70, no. 6, p. 766, 1993.

[41] M. M. Murnane, H. C. Kapteyn, and R. W. Falcone, "High-Density Plasmas Produced by Ultrafast Laser Pulses," *Physical Review Letters*, vol. 62, no. 2, p. 155, 1989.

[42] J. D. Kmetec, C. L. Gordon III, J. J. Macklin, B. E. Lemoff, G. S. Brown, and S. E. Harris, "MeV X-Ray Generation with a Femtosecond Laser," *Physical Review Letters*, vol. 68, no. 10, p. 1527, 1992.

[43] H. Hamster, A. Sullivan, S. Gordon, W. White, and R. W. Falcone, "Subpicosecond, Electromagnetic Pulses from Intense Laser-Plasma Interaction," *Physical Review Letters*, vol. 71, no. 17, p. 2725, 1993.

[44] A. Sävert, S. P. D. Mangles, M. Schnell, E. Siminos, J. M. Cole, M. Leier, M. Reuter, M. B. Schwab, M. Möller, K. Poder, *et al.*, "Direct Observation of the Injection Dynamics of a Laser Wakefield Accelerator Using Few-Femtosecond Shadowgraphy," *Physical Review Letters*, vol. 115, no. 5, p. 055002, 2015.

[45] D. Haffa, J. Bin, M. Speicher, K. Allinger, J. Hartmann, C. Kreuzer, E. Ridente, T. M. Ostermayr, and J. Schreiber, "Temporally Resolved Intensity Contouring

(TRIC) for characterization of the absolute spatio-temporal intensity distribution of a relativistic, femtosecond laser pulse," *Scientific Reports*, vol. 9, no. 1, pp. 1–9, 2019.

[46] C. W. Siders, S. P. Le Blanc, D. Fisher, T. Tajima, M. C. Downer, A. Babine, A. Stepanov, and A. Sergeev, "Laser Wakefield Excitation and Measurement by Femtosecond Longitudinal Interferometry," *Physical Review Letters*, vol. 76, no. 19, p. 3570, 1996.

[47] J. P. Geindre, P. Audebert, A. Rousse, F. Fallies, J. C. Gauthier, A. Mysyrowicz, A. Dos Santos, G. Hamoniaux, and A. Antonetti, "Frequency-domain interferometer for measuring the phase and amplitude of a femtosecond pulse probing a laser-produced plasma," *Optics Letters*, vol. 19, no. 23, pp. 1997–1999, 1994.

[48] D. Gabor, "A New Microscopic Principle," *Nature*, vol. 161, pp. 777–778, 1948.

[49] M. Centurion, Y. Pu, Z. Liu, D. Psaltis, and T. W. Hänsch, "Holographic recording of laser-induced plasma," *Optics Letters*, vol. 29, no. 7, pp. 772–774, 2004.

[50] S. P. Le Blanc, E. W. Gaul, N. H. Matlis, A. Rundquist, and M. C. Downer, "Single-shot measurement of temporal phase shifts by frequency-domain holography," *Optics Letters*, vol. 25, no. 10, pp. 764–766, 2000.

[51] N. H. Matlis, S. Reed, S. S. Bulanov, V. Chvykov, G. Kalintchenko, T. Matsuoka, P. Rousseau, V. Yanovsky, A. Maksimchuk, S. Kalmykov, *et al.*, "Snapshots of laser wakefields," *Nature Physics*, vol. 2, no. 11, pp. 749–753, 2006.

[52] L. B. Da Silva, T. W. Barbee Jr, R. Cauble, P. Celliers, D. Ciarlo, S. Libby, R. A. London, D. Matthews, S. Mrowka, J. C. Moreno, *et al.*, "Electron Density Measurements of High Density Plasmas Using Soft X-Ray Laser Interferometry," *Physical Review Letters*, vol. 74, no. 20, p. 3991, 1995.

[53] R. F. Smith, J. Dunn, J. Nilsen, V. N. Shlyaptsev, S. Moon, J. Filevich, J. J. Rocca, M. C. Marconi, J. R. Hunter, and T. W. Barbee Jr, "Picosecond X-Ray Laser Interferometry of Dense Plasmas," *Physical Review Letters*, vol. 89, no. 6, p. 065004, 2002.

[54] T. Kluge, M. Rödel, J. Metzkes-Ng, A. Pelka, A. L. Garcia, I. Prencipe, M. Rehwald, M. Nakatsutsumi, E. E. McBride, T. Schönherr, *et al.*, "Observation of

Ultrafast Solid-Density Plasma Dynamics Using Femtosecond X-Ray Pulses from a Free-Electron Laser," *Physical Review X*, vol. 8, no. 3, p. 031068, 2018.

[55] T. M. Ostermayr, J. Gebhard, D. Haffa, D. Kiefer, C. Kreuzer, K. Allinger, C. Bömer, J. Braenzel, M. Schnürer, I. Cermak, *et al.*, "A transportable Paul-trap for levitation and accurate positioning of micron-scale particles in vacuum for laser-plasma experiments," *Review of Scientific Instruments*, vol. 89, no. 1, p. 013302, 2018.

[56] J. D. Jackson, *Classical Electrodynamics.* New York, NY: Wiley, 1962.

[57] D. J. Griffiths, *Introduction to Electrodynamics; 3rd ed.* Upper Saddle River, NJ: Prentice-Hall, 1999.

[58] A. Macchi, *A Superintense Laser-Plasma Interaction Theory Primer.* Springer Science & Business Media, 2013.

[59] J. Meyer-ter Vehn, A. Pukhov, Z. Sheng, *et al.*, "Relativistic Laser Plasma Interaction," in *Atoms, Solids, and Plasmas in Super-Intense Laser Fields*, pp. 167–192, Springer, 2001.

[60] S. Karsch, "Applications of High-Intensity Laser-Pulses." Lecture notes, LMU Munich, 2015.

[61] J. D. Lawson, "Lasers and Accelerators," *IEEE Transactions on Nuclear Science*, vol. 26, no. 3, pp. 4217–4219, 1979.

[62] P. M. Woodward, "A method of calculating the field over a plane aperture required to produce a given polar diagram," *Journal of the Institution of Electrical Engineers-Part IIIA: Radiolocation*, vol. 93, no. 10, pp. 1554–1558, 1946.

[63] M. Protopapas, C. H. Keitel, and P. L. Knight, "Atomic physics with super-high intensity lasers," *Reports on Progress in Physics*, vol. 60, no. 4, p. 389, 1997.

[64] K. Burnett, V. C. Reed, and P. L. Knight, "Atoms in ultra-intense laser fields," *Journal of Physics B: Atomic, Molecular and Optical Physics*, vol. 26, no. 4, p. 561, 1993.

[65] G. Mainfray and G. Manus, "Multiphoton ionization of atoms," *Reports on Progress in Physics*, vol. 54, no. 10, p. 1333, 1991.

[66] P. Agostini, F. Fabre, G. Mainfray, G. Petite, and N. K. Rahman, “Free-Free Transitions Following Six-Photon Ionization of Xenon Atoms,” *Physical Review Letters*, vol. 42, no. 17, p. 1127, 1979.

[67] E. Mevel, P. Breger, R. Trainham, G. Petite, P. Agostini, A. Migus, J.-P. Chambaret, and A. Antonetti, “Atoms in Strong Optical Fields: Evolution from Multiphoton to Tunnel Ionization,” *Physical Review Letters*, vol. 70, no. 4, p. 406, 1993.

[68] L. V. Keldysh *et al.*, “Ionization in the field of a strong electromagnetic wave,” *Sov. Phys. JETP*, vol. 20, no. 5, pp. 1307–1314, 1965.

[69] M. V. Ammosov, N. B. Delone, and V. P. Krainov, “Tunnel ionization of complex atoms and of atomic ions in an alternating electromagnetic field,” *Soviet Journal of Experimental and Theoretical Physics*, vol. 64, no. 6, p. 1191, 1986.

[70] S. Augst, D. Strickland, D. D. Meyerhofer, S.-L. Chin, and J. H. Eberly, “Tunneling Ionization of Noble Gases in a High-Intensity Laser Field,” *Physical Review Letters*, vol. 63, no. 20, p. 2212, 1989.

[71] W. Lotz, “An Empirical Formula for the Electron-Impact Ionization Cross-Section,” *Zeitschrift für Physik*, vol. 206, no. 2, pp. 205–211, 1967.

[72] W. Lotz, “Electron-Impact Ionization Cross-Sections and Ionization Rate Coefficients for Atoms and Ions from Hydrogen to Calcium,” *Zeitschrift für Physik*, vol. 216, no. 3, pp. 241–247, 1968.

[73] T. Ditmire, T. Donnelly, A. M. Rubenchik, R. W. Falcone, and M. D. Perry, “Interaction of intense laser pulses with atomic clusters,” *Physical Review A*, vol. 53, no. 5, p. 3379, 1996.

[74] T. Ditmire, T. Donnelly, R. W. Falcone, and M. D. Perry, “Strong X-Ray Emission from High-Temperature Plasmas Produced by Intense Irradiation of Clusters,” *Physical Review Letters*, vol. 75, no. 17, p. 3122, 1995.

[75] F. F. Chen, *Introduction to Plasma Physics and Controlled Fusion; Third ed.* Springer, 2016.

[76] P. Gibbon, *Short Pulse Laser Interactions With Matter: An Introduction.* World Scientific, 2005.

[77] P. Mulser and D. Bauer, *High Power Laser-Matter Interaction*, vol. 238. Springer, 2010.

[78] W. L. Kruer, *The Physics of Laser Plasma Interactions.* Addison-Wesley Pub. Co. Inc., Reading, MA, 1988.

[79] L. Schlessinger and J. Wright, "Inverse-bremsstrahlung absorption rate in an intense laser field," *Physical Review A*, vol. 20, no. 5, p. 1934, 1979.

[80] F. Brunel, "Not-So-Resonant, Resonant Absorption," *Physical Review Letters*, vol. 59, no. 1, p. 52, 1987.

[81] W. L. l. Kruer and K. Estabrook, "J × B heating by very intense laser light," *The Physics of Fluids*, vol. 28, no. 1, pp. 430–432, 1985.

[82] W. Rozmus and V. T. Tikhonchuk, "Skin effect and interaction of short laser pulses with dense plasmas," *Physical Review A*, vol. 42, no. 12, p. 7401, 1990.

[83] P. J. Catto and R. M. More, "Sheath inverse bremsstrahlung in laser produced plasmas," *The Physics of Fluids*, vol. 20, no. 4, pp. 704–705, 1977.

[84] P. Gibbon and A. R. Bell, "Collisionless Absorption in Sharp-Edged Plasmas," *Physical Review Letters*, vol. 68, no. 10, p. 1535, 1992.

[85] G. Malka and J. L. Miquel, "Experimental confirmation of ponderomotive-force electrons produced by an ultrarelativistic laser pulse on a solid target," *Physical review letters*, vol. 77, no. 1, p. 75, 1996.

[86] M. Basko, "RALEF-2D, Main Report." `http://www.basko.net/mm/RALEF/ralef-main-report.pdf`. Accessed: 2022-03-12.

[87] B. Fryxell, K. Olson, P. Ricker, F. Timmes, M. Zingale, D. Q. Lamb, P. MacNeice, R. Rosner, J. W. Truran, and H. Tufo, "FLASH: An Adaptive Mesh Hydrodynamics Code for Modeling Astrophysical Thermonuclear Flashes," *The Astrophysical Journal Supplement Series*, vol. 131, no. 1, p. 273, 2000.

[88] V. P. Krainov and M. B. Smirnov, "Cluster beams in the super-intense femtosecond laser pulse," *Physics Reports*, vol. 370, no. 3, pp. 237–331, 2002.

[89] J. W. Goodman, *Introduction to Fourier Optics.* MaGraw-Hill, 2nd ed., 1996.

[90] E. Hecht, *Optik.* De Gruyter, 2018.

[91] T. Pertsch, “Fundamentals of modern optics.” Lecture notes, Friedrich-Schiller University Jena, 2014/2015.

[92] T.-C. Poon and T. Kim, *Engineering Optics with MATLAB®*. World Scientific, 2006.

[93] A. Einstein, “Zur Quantentheorie der Strahlung,” *Physikalische Zeitschrift*, vol. 18, pp. 121–128, 1917.

[94] R. Ladenburg, “Untersuchungen über die anomale Dispersion angeregter Gase,” *Zeitschrift für Physik*, vol. 48, no. 1, pp. 15–25, 1928.

[95] C. V. Shank and E. P. Ippen, “Subpicosecond kilowatt pulses from a mode-locked cw dye laser,” *Applied Physics Letters*, vol. 24, no. 8, pp. 373–375, 1974.

[96] S. Karsch, “Generation of ultraintense Laserpulses.” Lecture notes, LMU Munich, 2013.

[97] J. E. Murray and W. H. Lowdermilk, “ND:YAG regenerative amplifier,” *Journal of Applied Physics*, vol. 51, no. 7, pp. 3548–3556, 1980.

[98] W. H. Lowdermilk and J. E. Murray, “The multipass amplifier: Theory and numerical analysis,” *Journal of Applied Physics*, vol. 51, no. 5, pp. 2436–2444, 1980.

[99] G. Cheriaux, P. Rousseau, F. Salin, J. P. Chambaret, B. Walker, and L. F. Dimauro, “Aberration-free stretcher design for ultrashort-pulse amplification,” *Optics Letters*, vol. 21, no. 6, pp. 414–416, 1996.

[100] N. Weisse, “Automation of a 5 TW laser system,” Master’s thesis, LMU Munich, 2021.

[101] N. V. Didenko, A. V. Konyashchenko, A. P. Lutsenko, and S. Y. Tenyakov, “Contrast degradation in a chirped-pulse amplifier due to generation of prepulses by postpulses,” *Optics Express*, vol. 16, no. 5, pp. 3178–3190, 2008.

[102] “LightPipes for Python, Manual.” `https://opticspy.github.io/lightpipes/manual.html`. Accessed: 2022-03-12.

[103] C. Peltz, C. Varin, T. Brabec, and T. Fennel, “Time-Resolved X-Ray Imaging of Anisotropic Nanoplasma Expansion,” *Physical Review Letters*, vol. 113, no. 13, p. 133401, 2014.

[104] V. F. Kovalev and V. Y. Bychenkov, "Analytic Solutions to the Vlasov Equations for Expanding Plasmas," *Physical Review Letters*, vol. 90, no. 18, p. 185004, 2003.

[105] M. Murakami and M. M. Basko, "Self-similar expansion of finite-size non-quasi-neutral plasmas into vacuum: Relation to the problem of ion acceleration," *Physics of Plasmas*, vol. 13, no. 1, p. 012105, 2006.

[106] L. M. Wickens, J. E. Allen, and P. T. Rumsby, "Ion Emission from Laser-Produced Plasmas with Two Electron Temperatures," *Physical Review Letters*, vol. 41, no. 4, p. 243, 1978.

[107] M. Passoni, V. T. Tikhonchuk, M. Lontano, and V. Y. Bychenkov, "Charge separation effects in solid targets and ion acceleration with a two-temperature electron distribution," *Physical Review E*, vol. 69, no. 2, p. 026411, 2004.

[108] D. D. Hickstein, F. Dollar, J. A. Gaffney, M. E. Foord, G. M. Petrov, B. B. Palm, K. E. Keister, J. L. Ellis, C. Ding, S. B. Libby, *et al.*, "Observation and Control of Shock Waves in Individual Nanoplasmas," *Physical Review Letters*, vol. 112, no. 11, p. 115004, 2014.

[109] S. Faik, "FEOS Code Package." `https://physik.faik.de/feos.php?lang=eng`. Accessed: 2022-04-18.

[110] A. Naghilou, O. Armbruster, M. Kitzler, and W. Kautek, "Merging spot size and pulse number dependence of femtosecond laser ablation thresholds: modeling and demonstration with high impact polystyrene," *The Journal of Physical Chemistry C*, vol. 119, no. 40, pp. 22992–22998, 2015.

[111] D. J. O. Orzi, F. C. Alvira, and G. M. Bilmes, "Determination of femtosecond ablation thresholds by using laser ablation induced photoacoustics (LAIP)," *Applied Physics A*, vol. 110, no. 3, pp. 735–739, 2013.

[112] R. Suriano, A. Kuznetsov, S. M. Eaton, R. Kiyan, G. Cerullo, R. Osellame, B. N. Chichkov, M. Levi, and S. Turri, "Femtosecond laser ablation of polymeric substrates for the fabrication of microfluidic channels," *Applied Surface Science*, vol. 257, no. 14, pp. 6243–6250, 2011.

[113] N. I. of Standards and Technology, "NIST Chemistry WebBook, SRD 69." `https://webbook.nist.gov/cgi/cbook.cgi?ID=C100425&Mask=2FF`. Accessed: 2022-04-11.

[114] X. Y. Peng, J. Zhang, Z. Jin, T. J. Liang, Z. M. Sheng, Y. T. Li, Q. Z. Yu, Z. Y. Zheng, Z. H. Wang, Z. L. Chen, *et al.*, “Energetic electrons emitted from ethanol droplets irradiated by femtosecond laser pulses,” *Physical Review E*, vol. 69, no. 2, p. 026414, 2004.

[115] M. Anand, P. Gibbon, and M. Krishnamurthy, “Laser absorption in microdroplet plasmas,” *EPL (Europhysics Letters)*, vol. 80, no. 2, p. 25002, 2007.

[116] H. C. Wu, W. Yu, T. J. Liang, X. Y. Peng, Z. Jin, Y. J. Li, Z. M. Sheng, X. W. Tang, and J. Zhang, “A simple estimate of resonance absorption of femtosecond laser pulses by liquid droplets,” *Applied Physics B*, vol. 77, no. 6, pp. 687–689, 2003.

[117] J. Gebhard, *Laser-Ion-Acceleration from Tailored Micro-Plasmas (in preparation).* PhD thesis, LMU Munich, 2022.

[118] M. C. Kaluza, M. I. K. Santala, J. Schreiber, G. D. Tsakiris, and K. J. Witte, “Time-sequence imaging of relativistic laser–plasma interactions using a novel two-color probe pulse,” *Applied Physics B*, vol. 92, no. 4, pp. 475–479, 2008.

[119] C. Peltz, J. Powell, P. Rupp, A. Summers, T. Gorkhover, M. Gallei, I. Halfpap, E. Antonsson, B. Langer, C. Trallero, *et al.*, “Few-femtosecond resolved imaging of laser-driven nanoplasma expansion,” *New Journal of Physics*, 2022.

Acknowledgements

Am Ende dieser Arbeit möchte ich mich gerne bei all den Menschen bedanken, die mich während dieser Zeit begleitet haben und mich stets tatkräftig unterstützt haben.

An erster Stelle möchte ich meinem Doktorvater *Prof. Dr. Jörg Schreiber* danken, der es mir ermöglicht hat meine Doktorarbeit in seiner Arbeitsgruppe zu schreiben. Vielen Dank für die großartige Betreuung und Unterstützung, das Vertrauen, sowie für die vielen Gespräche und kritischen Diskussionen. Ich danke dir auch für die Möglichkeit den ZEUS Laser eigenverantwortlich zu betreuen und die vielen Freiheiten in der Verwirklichung meiner Arbeit.

Ein großer Dank geht an *PD Dr. Anna Tauschwitz* für die Zweitkorrektur dieser Arbeit und die Durchführung der RALEF Simulationen. Deine Unterstützung war eine enorme Hilfe bei der Interpretation der Daten.

Vielen Dank an die beste Arbeitsgruppe die man sich vorstellen kann. Danke an meine mittlerweile ehemaligen Kollegen *Prof. Dr Jianhui Bin*, *Dr. Ying Gao*, *Dr. Daniel Haffa*, *Dr. Peter Hilz*, *Dr. Christian Kreuzer*, *Dr. Florian Lindner* und *Dr. Tobias Ostermayr*, die mich als Masterstudent in der Gruppe aufgenommen haben und von denen ich so viel über Laser und Experimente lernen konnte. Ein großes Dankeschön möchte ich allen aktuellen Mitgliedern der LION- und HF Gruppe sagen: *Dr. Masoud Afshari*, *Felix Balling*, *Leonard Doyle*, *Erin Grace Fitzpatrick*, *Johannes Gebhard*, *Sonja Gerlach*, *Laura Geulig*, *Jens Hartmann*, *Lianren He*, *Julia Liese*, *Alexander Praßelsperger*, *Thomas Rösch* und *Anna-Katharina Schmidt.* Vielen Dank für die tolle Zusammenarbeit, die bedingungslose Unterstützung und die überagende Arbeitsatmosphäre innerhalb der Gruppe! Ihr alle habt diese Zeit zu etwas ganz Besonderem gemacht. Mein spezieller Dank gilt meinem Bürokollegen Lenny für die Unterstützung mit den LightPipes Simulationen sowie die vielen physikalischen Diskussionen. Ein großer Dank auch an Johannes, Jens und Thomas für die vielen Ratschläge und Unterstützung während dem Schreiben dieser Arbeit.

Meinen Bachelor- und Masterstudenten *Michael Heynck*, *Tanja Rohrmoser* und *Nils Weisse* möchte ich für die tollen Arbeiten und die Weiterentwicklung wichtiger Projekte danken. Auch allen anderen Kollegen, mit denen ich während meiner Zeit hier zusammenarbeiten durfte gilt mein großer Dank: *Prof. Dr. Paul Bolton*, *Dr.*

Enrico Ridente, *Dr. Matthias Würl*, *Franz Englbrecht*, *Daniel Hahner* und auch allen anderen die ich hier vergessen haben sollte zu nennen.

Ein herzlicher Dank geht an das gesamte ZEUS-Team *Felix Balling*, *Johannes Gebhard* und *Nils Weisse* für die Unterstützung bei den Experimenten, die tolle Stimmung und den Durchhaltewillen wenn die ZEUS-Paulfallen-Unschärferelation uns mal wieder einen Strich durch die Rechnung gemacht hat. Ein großes Dankeschön auch an *Prof. Dr. Wolfgang Zinth* der unserer Gruppe den ZEUS Laser überlassen hat. Mein spezieller Dank gilt an dieser Stelle Johannes, der mit mir zusammen das gesamte ZEUS Experiment aufgebaut und durchgeführt hat. Ohne deine Unterstützung wäre diese Arbeit nicht möglich gewesen! Vielen Dank auch für die vielen gemeinsamen Rennrad-Fahrten, die wir hoffentlich auch in Zukunft fortführen werden.

Bedanken möchte ich mich auch bei den Menschen, die es mir ermöglicht haben auch an anderen Lasersystemen zu experimentieren. Thanks to *Prof Brendan Dromey* and his team for allowing me to participate at their experiments at the Rutherford Appleton Lab. Auch *Johannes Gebhard*, *Dr. Florian Lindner* und *Prof. Dr. Peter G. Thirolf* möchte ich danken, dass ich an den Experimenten am JETI-Laser und am PHELIX-Laser teilnehmen durfte.

Mein Dank gilt *Nik Gjotev*, *Oliver Gosau*, *Florian Saran* und *Dr. Hans-Friedrich Wirth* für ihre Hilfsbereitschaft und Unterstützung bei allen technischen Fragen. Auch bei der mechanischen Werkstatt unter Leitung von *Rolf Öhm* möchte ich für die Anfertigung unzähliger Prototypen herzlich danken. Vielen Dank an *Katharina Adler* und das Team der Buchhaltung.

Beim ganzen Lehrstuhl für Medizinphysik um *Prof. Dr. Katia Parodi* möchte ich mich für die tolle Zusammenarbeit bedanken, im Besonderen auch bei *Prof. Dr. Peter G. Thirolf*, *Dr. Jona Bortfeld*, *Dr. Felix Rauscher* und *Andrea Leinthaler.*

Für die Unterstützung bei allen Laserfragen danke ich der gesamten Gruppe um *Prof. Dr. Stefan Karsch*, vor allem *Moritz Foerster*, *Max Gilljohann*, *Johannes Götzfried* und *Gregor Schilling.*

Ein riesengroßes Dankeschön möchte ich auch all meinen Freunden außerhalb der Arbeitsgruppe sagen, vor allem *Andi*, *Dominik*, *Domi*, *Harald*, *Jana*, *Tom* und *Tommi.* Danke für eure Freundschaft und dass man immer auf euch zählen kann.

Zum Schluss möchte ich mich noch bei den wichtigsten Menschen in meinem Leben bedanken. Bei *meiner Schwester* und bei *meinen Eltern*, die mich immer bedingungslos unterstützt haben, in allen Lebenslagen hinter mir stehen und mir diesen Weg ermöglicht haben. Vor allem aber bei meiner *Franzi*, die mich durch alle Höhen und Tiefen begleitet hat, mich stets ermutigt hat und mir immer zur Seite stand. Danke dass du diesen Weg gemeinsam mit mir gehst.